Millimeter-wave Integrated Horn Antennas

by

Erik Kurt Duerr

Submitted to the Department of Electrical Engineering and Computer Science
in partial fulfillment of the requirements for the degree of

Master of Science in Electrical Engineering and Computer Science

at the

MASSACHUSETTS INSTITUTE OF TECHNOLOGY

February 1998

Author .....
Department of Electrical Engineering and Computer Science
December 15, 1997

Certified by .....
Qing Hu
Associate Professor of Electrical Engineering and Computer Science
Thesis Supervisor

Accepted by .....
Arthur C. Smith
Chairman, Departmental Committee on Graduate Students

Millimeter-wave Integrated Horn Antennas

by

Erik Kurt Duerr

Submitted to the Department of Electrical Engineering and Computer Science
on December 12, 1997, in partial fulfillment of the
requirements for the degree of
Master of Science in Electrical Engineering and Computer Science

Abstract

This thesis explores the modeling, design, and fabrication of millimeter-wave quasi-integrated horn antennas consisting of a micromachined horn with an embedded detector and a small flare angle machined horn. The micromachined portion of the quasi-integrated millimeter-wave horns can be fabricated using low-cost, well-established techniques. To facilitate lower-cost fabrication of the machined section, this thesis explores the use of circular machined sections. Circular sections are much cheaper to fabricate than the previously used rectangular machined sections.

In order to predict the performance of circular sections, the mode matching method along with the generalized scattering matrix technique is used to model the quasi-integrated horn. The far-field pattern is predicted and designs of circular sections are created. The designed narrow flare angle circular sections were fabricated through the use of conventional and laser machining. Far-field patterns of six configurations of quasi-integrated horns were successfully obtained. These measurements indicate good agreement with the predictions of the modeling code. Explanations are offered for discrepancies between measurement and theory.

Thesis Supervisor: Qing Hu
Title: Associate Professor of Electrical Engineering and Computer Science

Acknowledgments

I have been fortunate to spend the past two years in an intellectually stimulating and challenging environment here at MIT. I would first like to thank Professor Qing Hu for providing me with this project and for supervising this thesis work. Professor Hu also deserves special thanks for bringing together the research group of intelligent, motivated and talented engineers and physicists. The synergy created by this environment certainly aided everyone in the lab in their intellectual and academic development. I would also like to thank Rick Magliocco, Lisa Hill, and Stan Robertson from the Hybrid Circuit Lab in Group 63 at MIT Lincoln Laboratory for their technical assistance and advice during the fabrication of my circular horn designs.

Members of my research group provided practical assistance, imparted information on a wide variety of subjects, and made the lab a fun learning environment. Dr. Ir. Gerhard de Lange deserves special thanks for his assistance, advice, and mentoring throughout the project. As well as being an AutoCAD, LaTeX, and MathCAD guru, he provided numerous suggestions and consultations on experimental technique and engineering design in addition to providing insight into fundamental physics concepts. My officemate and member of my subgroup, Konstantinos Konistis, was extremely helpful in discussions on electromagnetic phenomena. Arifur Rahman fabricated the micromachined horns with microbolometers that were used in measuring the far-field pattern of the quasi-integrated horns. From the quantum well subgroup, Ilya Lyubomirsky, Brian Riely, Ben Williams, and Bin Xu all gave seminars detailing the development of far- and mid-infrared quantum cascade lasers. In addition to discussing quantum well topics, my officemate, Ben, and I also had a lot of fun discussing life at MIT and exploring the lighter side of the internet. Discussions with Brian provided insight into topics related to basic physics concepts. Bin and I had many late-night discussions dealing with a wide variety of topics. Noah Zamdmer explained the intricacies of performing pump-probe measurements of quantum effect devices and of aligning tiny fibers to tiny Auston switches. Farhan Rana and I had numerous late-night discussions covering topics as wide ranging as Pakistani geography, quantum field theory, my thesis, and the philosophical implications of quantum mechanics.

I would like to express my deepest gratitude to my parents for all of their love, care, and support both during this thesis and during my younger years. I would never have made it without my mother's encouragement and humor or without my father's encouragement and engineering insight. I give a heartfelt thanks for my family and friends for all of their prayers and support during this thesis. I also acknowledge that without the peace, wisdom and answered prayer that come from my relationship with God, I could not have successfully completed this thesis.

This research was supported in part through a National Defense Science and Engineering Grant (NDSEG) Graduate Fellowship. This research was also supported in part by the U. S. Army Research Laboratory Cooperative Agreement DAAL01-96-2-0001.

Contents

List of Figures

This page intentionally left blank.

List of Tables

This page intentionally left blank.

Chapter 1

Introduction

1.1 Motivation

Atmospheric attenuation varies considerably in the millimeter wave frequency range (30–300 GHz) with windows of low attenuation (30–38 GHz, 70–115 GHz, 130–180 GHz, 195–300 GHz) interspersed with bands of high absorption as shown in Figure 1-1[1]. Millimeter wave systems can be designed to take advantage of both the low attenuation windows and the high absorption bands. In addition to being able to penetrate the atmosphere, millimeter waves, unlike optical and infrared radiation, pass through smoke, fog, and light rain with little power loss or distortion[2]. Thus, millimeter wave devices can be used in foul weather or in smoky conditions. Though microwaves also exhibit similar propagation characteristics, millimeter wave systems can achieve better performance with more compact and lighter weight systems. The millimeter wave part of the spectrum is also much less crowded than the microwave portion and offers inherently higher bandwidth. As a result of these advantages, companies are interested in developing systems which operate at millimeter wave frequencies for both commercial and military applications. The recent development of technologies which allow low cost, high volume production of millimeter wave components means that commercial implementation of millimeter wave systems is finally a viable possibility[3, 4, 5, 6, 7, 8]. The two major areas of commercial application are communication systems and transportation aids[9].

In military applications, communication and imaging systems are two areas in which

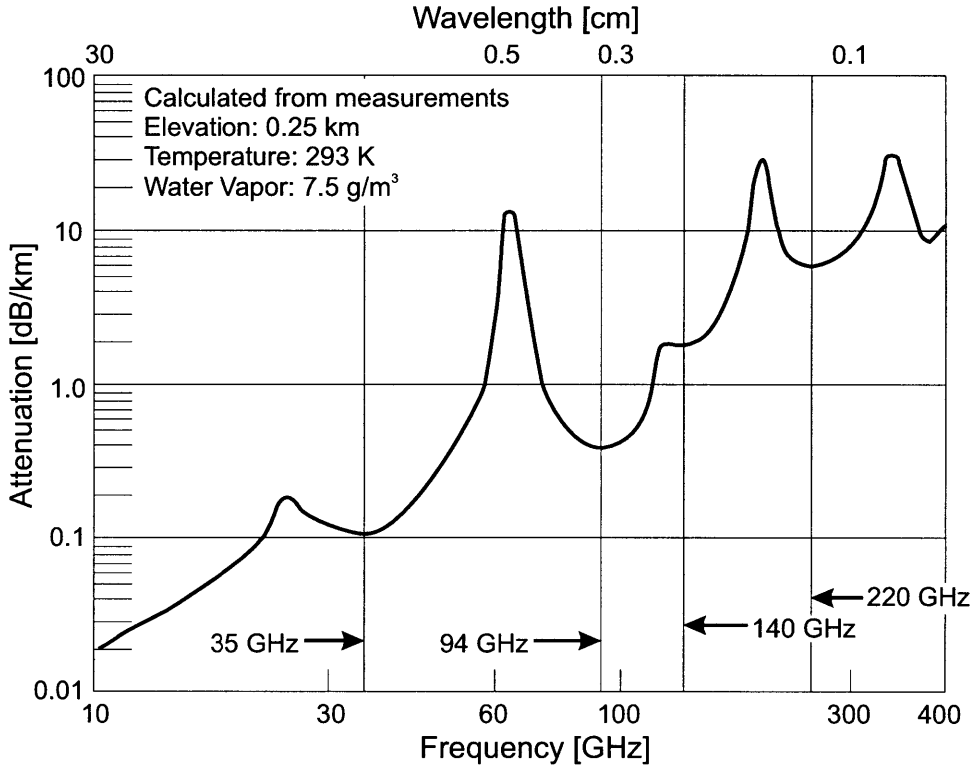

Figure 1-1: *Atmospheric absorption in the millimeter-wave frequency range. From [1]*

millimeter wave systems are currently being developed. Much military work has been performed at 94 GHz, the center of a transmission window, but other parts of the spectrum have also been explored. By operating in a band of high absorption, such as the oxygen band at 60 GHz, a low probability of intercept (LPI) link can be used to transmit sensitive information with little danger of eavesdropping. "Detection as well as interception and jamming of a 60GHz LPI-link is nearly impossible."[10] In addition to being used for communication links, millimeter-wave imaging technology has obvious applications in battlefield imaging. As a complement to infrared based night vision technology, millimeter wave imagers could be used when inclement weather or smoke prevent the use of infrared sensors.

Commercial communication system designers can use different parts of the millimeter wave spectrum for different purposes. Systems operating in an absorption band have very limited range thus permitting frequency reuse, while systems in low attenuation windows allow for longer links[11]. Other applications for communication in high attenuation bands include urban links, personal communication networks (PCN), and inter-satellite

links[10]. A good example of an urban short range link is the wireless local-area network (WLAN). Millimeter wave technology offers large bandwidth potential to WLANs for flexible, high data rate communication within offices[2]. Systems which demonstrate the feasibility of the WLAN[12] as well as its integration with a fiber backbone[13] have been demonstrated. Millimeter wave components[14] and complete systems[5, 15] have been designed and tested for PCN applications. Applications for longer range millimeter wave communication links include connecting a group of cellular telephone cells with a controller station and distributing high bandwidth video services such as "interactive television transmission and teleconferencing"[16]. A system for distributing digital radio using millimeter wave components has also been developed[17]. In addition to technical work, vital frequency allocation and other policy questions are being discussed in Europe and in the United States[18, 19].

Transportation aids, including automobile collision avoidance radar, intelligent cruise control (ICC), railway information and control systems, and runway imaging systems, can take advantage of high and low attenuation frequency bands[20, 21, 22]. Automotive applications have received the majority of the work as the potential market is very large, and many people see Road Traffic Informatics (RTI) as the best way to alleviate growing traffic congestion problems[23]. Three major highway applications for electromagnetic wave systems are automatic toll systems, transmission systems (car-to-car and car-to-roadside), and collision avoidance radar[20, 24, 25]. While automatic debiting systems (ADS) have been universally implemented at microwave frequencies around 6 GHz, the other two applications are best suited to millimeter wave frequencies. Anticollision radar could be used both for ICC systems and for obstacle warning systems[26]. As communication systems could be designed in absorption bands to avoid long range signal propagation, radar systems operating in absorption bands reduce the possibility of interference between two different systems. Extensive work has been done at the component[27, 28] and system[29, 30] level. Radar systems with a longer range have also been designed and tested[6, 31, 32]. As railways become more congested and trains travel at higher speeds, communication links between trains and a control center become increasingly important for safety and efficiency. As millimeter wave systems could provide this service for highways, millimeter

wave systems have been shown effective for rail applications[22]. Finally, long distance imaging technology can aid aircraft for improved inclement weather guidance and landing systems[33]. Systems demonstrating the concept have been constructed at 90 and 94 GHz[21, 34, 35].

Widespread use of millimeter wave systems has been hindered by the cost and difficulty of fabricating millimeter wave devices. Previously mentioned work[3, 4, 7, 14] has been directed primarily toward the development of active devices for millimeter wave transmitters. In the fabrication of transmitters and detectors, an antenna structure must be used to couple the radiation out of the transmitter or into the detector. For systems requiring high performance, one of two radiation coupling methods has been traditionally used, a metal horn antenna or a planar antenna with lens. Lens coupled planar antennas are difficult to fabricate in arrays as the lens must be much larger than the planar antenna, thus prohibiting close element spacing. Similarly, the smaller dimensions of the horn antenna must be on the order of the wavelength of the radiation and machining accuracy must be much less than a wavelength. Machining these horns becomes very difficult and costly at millimeter wave frequencies. In addition, the effort required to machine these horns increases linearly with the number of elements, making large array manufacture extremely costly. In order for millimeter wave devices to be widely accepted in commercial or military markets, simpler fabrication techniques are needed.

New fabrication techniques provide a means of creating millimeter-wave systems at much lower cost than traditional techniques. One of the most promising new techniques, silicon (Si) micromachining has been used for the fabrication of sensitive millimeter wave detector systems[36, 37, 38, 39, 40, 41, 42, 43, 44], waveguides and transmission lines[33, 45, 46, 47], filters[48], and antennas[49, 50, 51] among other structures. In one application of this technology, researchers at the University of Michigan developed the technique of anisotropic silicon etching to form a pyramidal cavity in a stack of silicon wafers[39, 40, 52, 53] as shown in Figure 1-2. A silicon nitride membrane on one wafer is not removed. On this membrane, the detecting element is fabricated along with a dipole antenna[54]. The dipole antenna couples the radiation gathered by the horn structure to the detecting element. As an entire wafer with many devices can be processed in a single fabrication

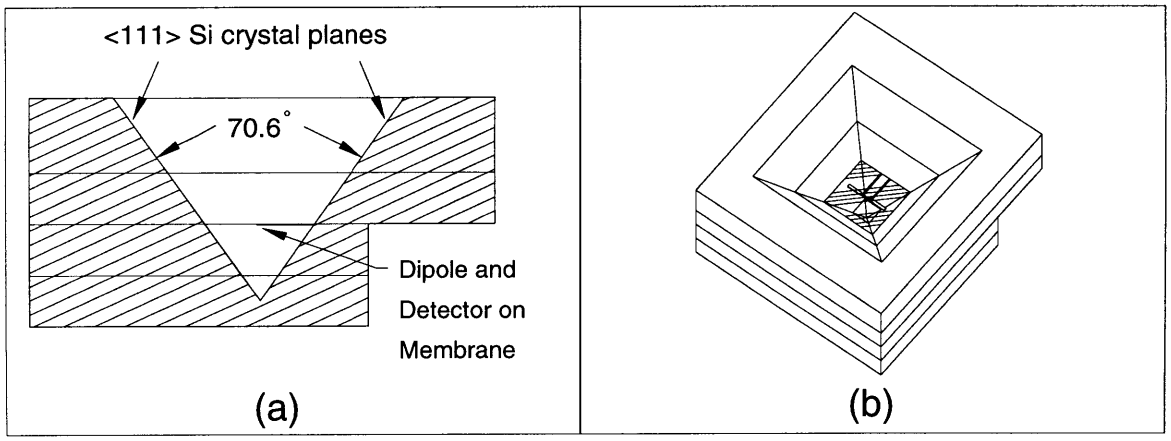

Figure 1-2: *(a) Cross-section view of micromachined horn; (b) Micromachined horn antenna with dipole antenna fabricated on Si_3N_4 membrane*

run, the micromachining technique lends itself to array fabrication. Array fabrication has been accomplished[44]. An advantage of using silicon processing is that the entire microelectronics industry is built around silicon. Commercially tested techniques already exist for device fabrication. Being able to fabricate devices such as local oscillators[55], amplifiers, and signal processing circuits on the same wafer as the detector further increases the usefulness of the devices and the appeal of micromachining. Relatively easy mass production of detectors is another benefit of using a technology that has a pre-existing infrastructure. As the designs of systems using micromachined horns are improved, the probability of using this technology to tap the aforementioned commercial and military markets increases.

1.2 Approach

The pyramidal horn formed by anisotropic etching of Si is defined by the $\langle 111 \rangle$ crystal planes of Si. These crystal planes form a horn with 70.6° flare angle. This large flare angle places the practical limit on the maximum directivity achievable by micromachined horn antennas at 13 dB[56]. For some applications such as focal plane imaging arrays, this directivity is not high enough. One approach for improving the directivity and beam pattern of the horn consists of attaching a machined horn section with small flare angle to the aperture of the micromachined section. With this type of design called a quasi-integrated horn,

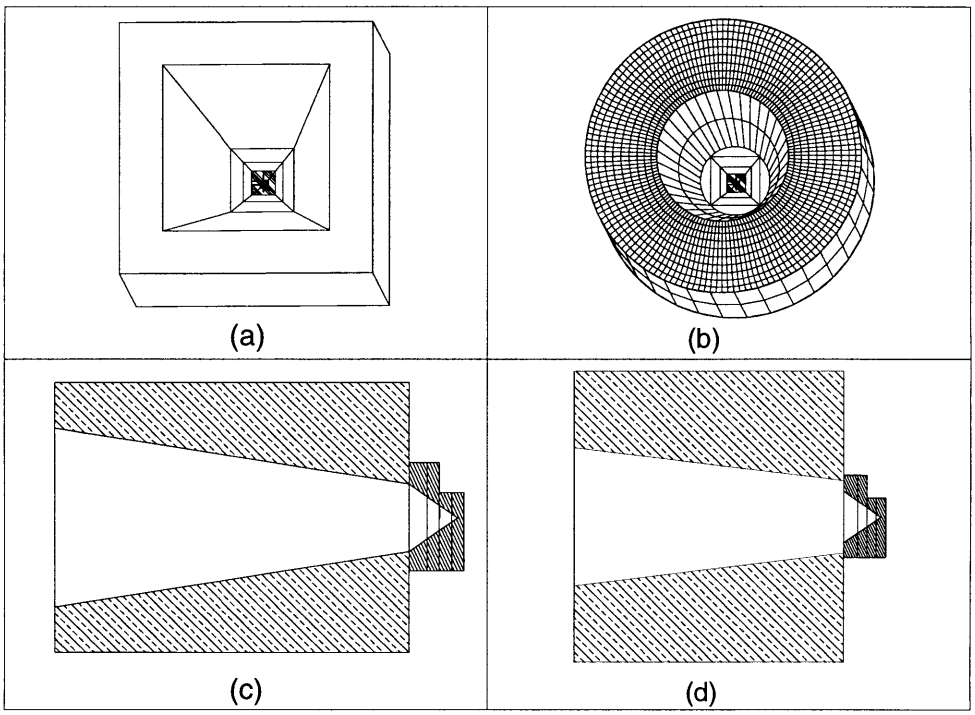

Figure 1-3: *(a) Perspective view of micromachined horn with rectangular machined section; (b) Perspective view of micromachined horn with circular machined section; (c) Cross-section of (a); (d) Cross-section of (b)*

directivities as high as 20 dB and 25 dB have been achieved[53, 56]. Because the pyramidal micromachined horn has a rectangular cross section, the machined horn section was also designed with a rectangular cross section. Though this machined section is not as difficult and expensive to make as the waveguides for traditional waveguide receivers, considerable cost is still involved. Fabrication of the machined section could be accomplished more easily if the cross section were circular instead of rectangular. A mandril machined on a lathe could be used as a die to fabricate machined horn sections. Alternatively, the horn could be machined directly using a tapered end mill or lathe. Perspective and cross-section views of the micromachined section with both rectangular and circular machined sections are shown in Figure 1-3.

An accurate simulation of the micromachined antenna with machined section is needed in order to design the machined section properly. The simulation needs to provide information about the directivity of the antenna, the beam pattern, and the embedding impedance seen by the detector element. Numerous electromagnetic modeling techniques can be

used to provide this type of information[56]. An accurate model of the micromachined antenna with rectangular machined section was developed by George Eleftheriades using the mode matching method with generalized scattering matrices[39, 56, 57]. The mode matching method and generalized scattering matrix methods are well known[58, 59, 60] and have been used to solve a number of electromagnetic problems[61, 62, 63, 64, 65, 66]. The methods are particularly suited to analyzing waveguide discontinuities and tapered waveguides (i.e. horns)[67, 68, 69, 70, 71]. The junction of the micromachined section and machined section will be modeled as the junction between a rectangular waveguide and a circular waveguide. Several groups have reported using these modeling techniques to predict scattering from rectangular to circular waveguide[72, 73, 74, 75]. Using these results as a starting point, modification of the FORTRAN code written by Eleftheriades was made in order to model a micromachined antenna section with circular machined horn section.

In order to test the simulation, circular machined sections were fabricated for use with existing micromachined sections. While most circular horns are machined on a lathe, other technologies for fabrication of the machined section are effective, especially in low volume applications. Millimeter wave horns have been successfully fabricated out of stacks of wafers[76, 77]. Called platelet horns, these structures are fabricated by stacking a large number of very thin wafers each of which has a different size aperture cut out of it. Laser cutting tools can accurately cut the apertures in the metal or non-metal wafers. We fabricated and tested both platelet horns and standard machined horns. Because silicon is inexpensive and can be laser machined easily, silicon wafers were used for the fabrication of the machined horn section. This work is the first time platelet horns have been fabricated from non-metal wafers. This work also represents one of the first times that quasi-integrated horns have been made from micromachined horns and circular machined sections.

1.3 Thesis Overview

In Chapter 2, the electromagnetic modeling theory of mode matching is presented. Results of applying this technique to the specific problem of a transition between a rectangular

waveguide to a circular waveguide. The technique for applying the mode matching method to the design of quasi-integrated horn antennas is presented in Chapter 3. The fabrication steps of the platelet horns and design of the experimental setup are presented in Chapter 4. Experimental results and discussion of the results are also presented in Chapter 4. Conclusions drawn and suggestions for future work are made in Chapter 5.

Chapter 2

Electromagnetic Modeling

Numerous electromagnetic modeling techniques are available for describing the interaction of electromagnetic waves and media[78]. Since very few electromagnetics problems have exact analytic solutions, semi-analytical and numerical methods must be used to solve the remaining problems. Completely numerical methods, such as finite difference time domain, transmission line method, and method of moments, suffer the drawbacks that these methods do not efficiently model electrically large or open structures[56]. These shortcomings mean that these techniques are not optimal for modeling a horn that has an aperture with dimensions of a few wavelengths. The semi-analytical techniques of mode matching and generalized scattering matrices have been used to successfully characterize and design electromagnetic horns[67, 68, 79, 80], and specifically micromachined horns[39, 56, 57]. An introduction to waveguide theory is provided before describing the mode matching method.

2.1 Waveguide Theory

A brief discussion of waveguide theory especially as is relevant to the mode matching method is given here. A more complete discussion can be found in references [81, 82, 83, 84].

Electromagnetic waves obey Maxwell's equations[1]

$$\nabla \times \vec{E} = -\frac{\partial \vec{B}}{\partial t} \tag{2.1}$$

$$\nabla \times \vec{H} = \frac{\partial \vec{D}}{\partial t} + \vec{J} \tag{2.2}$$

$$\nabla \cdot \vec{D} = \rho \tag{2.3}$$

$$\nabla \cdot \vec{B} = 0\,, \tag{2.4}$$

where $\vec{E}$ is the electric field, $\vec{H}$ is the magnetic field, $\vec{D}$ is the electric displacement, and $\vec{B}$ is the magnetic flux[85]. Solutions to Maxwell's equations are chosen so that they satisfy the boundary conditions[2]

$$\hat{n} \times (\vec{E}_1 - \vec{E}_2) = 0 \tag{2.5}$$

$$\hat{n} \times (\vec{H}_1 - \vec{H}_2) = \vec{J}_s \tag{2.6}$$

$$\hat{n} \cdot (\vec{B}_1 - \vec{B}_2) = 0 \tag{2.7}$$

$$\hat{n} \cdot (\vec{D}_1 - \vec{D}_2) = \rho_s\,, \tag{2.8}$$

where $\vec{J}_s$ is the surface current, ρ_s is the surface charge, and $\hat{n}$ and regions 1 and 2 are shown in Figure [85]. In an isotropic environment as is found in most dielectric filled waveguides, the constitutive relations are

$$\vec{D} = \epsilon \vec{E} \tag{2.9}$$

$$\vec{B} = \mu \vec{H}. \tag{2.10}$$

In a source-free environment and assuming a $e^{j\omega t}$ time dependence and constitutive relations (2.9) and (2.10), Maxwell's equations become

$$\nabla \times \vec{E} = -j\omega\mu\vec{H} \tag{2.11}$$

[1]Maxwell's equations are presented here in vector form, assuming that no magnetic charge or current exists.

[2]The boundary conditions presented here assume a stationary boundary.

$$\nabla \times \vec{H} = j\omega\epsilon\vec{E} \tag{2.12}$$

$$\nabla \cdot \vec{E} = 0 \tag{2.13}$$

$$\nabla \cdot \vec{H} = 0. \tag{2.14}$$

From equations (2.11-2.14) and (2.9-2.10), it can easily be shown that the electric ($\vec{E}$) and magnetic ($\vec{H}$) fields are solutions to the homogeneous vector Helmholtz equations

$$\nabla^2\vec{E} + k^2\vec{E} = 0 \tag{2.15}$$

$$\nabla^2\vec{H} + k^2\vec{H} = 0, \tag{2.16}$$

where k is the wave number, $k = \omega\sqrt{\mu\epsilon} = \frac{2\pi}{\lambda}$ [83]. In closed, perfectly-conducting waveguides with uniform axial geometry and filled with an isotropic, lossless dielectric, the solutions take two forms, transverse electric (TE) solutions which do not have an axial component of the electric field and transverse magnetic (TM) solutions which do not have an axial component of the magnetic field. Each solution is a mode, or eigenmode, of the waveguide. The functional form of the eigenmode is determined by the transverse geometry of the waveguide, as the geometry determines the surface over which the boundary conditions are applied. Assuming the fields vary time harmonically and the longitudinal axis of the waveguide is the z axis, the general solutions for TE waves can be expressed as the sum of waves propagating the positive and negative z directions

$$\vec{E} = \vec{E}^+ + \vec{E}^- = \left(\vec{E}_t\right) e^{-j\beta z} + \left(\vec{E}_t\right) e^{j\beta z} \tag{2.17}$$

$$\vec{H} = \vec{H}^+ + \vec{H}^- = \left(\vec{H}_t + \vec{H}_z\right) e^{-j\beta z} + \left(-\vec{H}_t + \vec{H}_z\right) e^{j\beta z}, \tag{2.18}$$

where the subscripts t and z indicate the transverse and axial components, respectively. Similarly, for a TM mode, the solution has the form

$$\vec{E} = \vec{E}^+ + \vec{E}^- = \left(\vec{E}_t + \vec{E}_z\right) e^{-j\beta z} + \left(\vec{E}_t - \vec{E}_z\right) e^{j\beta z} \tag{2.19}$$

$$\vec{H} = \vec{H}^+ + \vec{H}^- = \left(\vec{H}_t\right) e^{-j\beta z} - \left(\vec{H}_t\right) e^{j\beta z}. \tag{2.20}$$

The solutions to the homogeneous Helmholtz equations (2.15) and (2.16) are usually chosen such that the eigenmodes are orthonormal (orthogonal and normalized), that is

$$\langle \vec{e}_m, \vec{e}_n \rangle_A = \int_A \vec{e}_m \cdot \vec{e}_n \, dA = \begin{cases} 1 & \text{if } m = n \\ 0 & \text{if } m \neq n \end{cases}, \tag{2.21}$$

where A is the transverse cross-section of the waveguide. Other authors express the orthonormalization as

$$\langle \vec{e}_m, \vec{h}_n \rangle_A = \int_A \vec{e}_m \times \vec{h}_n \cdot \hat{z} \, dA = \begin{cases} 1 & \text{if } m = n \\ 0 & \text{if } m \neq n \end{cases}, \tag{2.22}$$

but for mode expressions defined as in appendix section A.1.3, the definitions are equivalent. Because the eigenmodes are generally chosen to be real functions, taking the complex conjugate of the $\vec{h}$ term would not produce a different result. Any electromagnetic field in the guide can be represented by an appropriately weighted infinite sum of eigenmodes[81].

Appendix A contains the derivation for the expressions of the eigenmodes in circular and rectangular guides.

2.2 Mode Matching Method

Mode matching is a method used to describe electromagnetic fields interacting at an interface. In waveguide analysis, the method is generally used to describe the effect of a discontinuity, where a discontinuity is defined as a change in the transverse geometry of the guide. This technique is often applied to horn design by approximating a smooth horn structure as a stepped series of progressively larger waveguides each with uniform cross-section[67, 80]. Eleftheriades, et al. have shown that this approximation yields results which agree well with experiment as long as enough waveguide sections are used[39, 40].

A brief, general introduction to the technique of mode matching is provided before specific examples are discussed.

2.2.1 General Technique

The standard electromagnetic boundary conditions (2.5) and (2.6) determine the relationship between tangential electric and magnetic fields on either side of a boundary. These simple, fundamental relations are the basis for the mode matching method. The method is used to find a convenient way of expressing the relationship between the fields on either side of a boundary. Mode matching is used when the fields on either side of the boundary are easily expressed as a sum of orthogonal eigenmodes.[3] Thus, the method is used almost exclusively in waveguide analysis. A discontinuity in the waveguide defines the boundary across which the boundary conditions are enforced. A set of matrix equations are obtained from the boundary condition equations applied to the discontinuity. These matrix equations can be arranged to yield the generalized scattering parameters which give an expression for the coupling of each eigenmode on one side of the boundary to each eigenmode on the other side of the boundary[59]. Written in matrix form, these coupling coefficients are called a generalized scattering matrix. A generalized scattering matrix is similar to the standard scattering matrix of circuit theory, but can be used to relate evanescent, or cutoff, modes as well as propagating modes.

2.2.2 Analysis of a Bifurcated Waveguide

The prototypical example for illustrating the mode matching method is the bifurcated waveguide, a waveguide that is divided by a semi-infinite septum, as in Figure 2-1. The boundary across which the field matching is performed is the junction between the larger guide and the two smaller guides. In region 1, the field is the sum of eigenmodes of the larger guide, while on the other side the field is composed piecewise of the field in each smaller guide, 2 and 3. For the sake of simplicity, a guide with no variation in one of the two transverse dimensions will be considered. As shown in Figure 2-1, the x direction is the single transverse dimension, and the guide extends longitudinally in the z direction. In this example, the lower-case mode function variables, $\vec{e}$ and $\vec{h}$, correspond to mode expressions defined as $\vec{e}_t$ and $\vec{h}_t$ in appendix section A.1.3. A general expression for the

[3] If some modes are degenerate, then they are orthogonalized before mode matching is done.

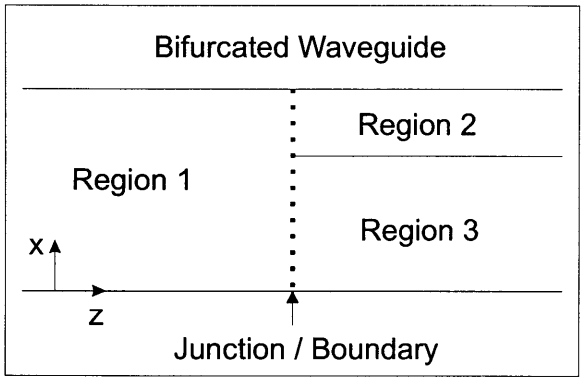

Figure 2-1: *Detail of junction in bifurcated waveguide.*

mode summation is used with no distinction made between TE and TM modes. Two mode indices are used for the sake of generality and applicability to the remainder of this thesis even though modes in infinite parallel plate waveguides need only one index.

For the case of a bifurcated guide, sheet current cannot exist on the boundary as there is no conductor to support a current. Thus, the tangential electric $\vec{E}_t$ and magnetic $\vec{H}_t$ fields must be continuous across the boundary. The electric field matching expression can be written as

$$\vec{E}_t^1 = \vec{E}_t^2 u_2 + \vec{E}_t^3 u_3, \tag{2.23}$$

where the superscript or subscript numbers refer to the region, or guide, of that particular number and where

$$u_p = \begin{cases} 1 & \text{in guide } p \\ 0 & \text{elsewhere} \end{cases} . \tag{2.24}$$

Expanding the tangential field expressions in terms of normalized eigenfunctions, equation (2.23) becomes

$$\begin{aligned} \sum_{mn} \left(a_{mn}^+ + a_{mn}^-\right) \sqrt{Z_{1,mn}} \vec{e}_{mn}^1 = & \sum_{qr} \left(b_{qr}^+ + b_{qr}^-\right) \sqrt{Z_{2,qr}} \vec{e}_{qr}^2 u_2 \\ & + \sum_{uv} \left(c_{uv}^+ + c_{uv}^-\right) \sqrt{Z_{3,uv}} \vec{e}_{uv}^3 u_3 \end{aligned} , \tag{2.25}$$

where $Z_{p,bc}$ is the impedance of the bc^{th} mode in guide p. The variables a, b, and c are the complex modal amplitudes of the eigenmodes in guides 1, 2, and 3, respectively. A similar

equation for the magnetic field is

$$\vec{H}_t^1 = \vec{H}_t^2 u_2 + \vec{H}_t^3 u_3 \tag{2.26}$$

$$\sum_{mn} \left(a_{mn}^+ - a_{mn}^-\right) \frac{\vec{h}_{mn}^{\,1}}{\sqrt{Z_{1,mn}}} = \sum_{qr} \left(b_{qr}^+ - b_{qr}^-\right) \frac{\vec{h}_{qr}^{\,2} u_2}{\sqrt{Z_{2,qr}}} + \sum_{uv} \left(c_{uv}^+ - c_{uv}^-\right) \frac{\vec{h}_{uv}^{\,3} u_3}{\sqrt{Z_{3,uv}}}, \tag{2.27}$$

where $\vec{h}^p = \hat{z} \times \vec{e}^p$ for guide p. The two equations (2.25) and (2.27) are the fundamental equations needed to derive expressions for the scattering parameters relating the eigenmodes on either side of the boundary.

The scalar product of an eigenmode, e.g. $\vec{e}_{MN}^{\,1}$, is formed on both sides of equation (2.25). The equation is integrated over the aperture of the waveguide from which the eigenmode was chosen. Because of the orthogonality of the eigenmodes of a particular guide, (i.e. $\int_{A_1} \vec{e}_{mn}^{\,1} \cdot \vec{e}_{MN}^{\,1} dA = 0$, for $m \neq M$ or $n \neq N$), only the term corresponding to the MN^{th} mode in the sum of modes for guide 1 survives. This procedure can be used to obtain an expression for each mode in guide 1. For example, if the scalar product of $\vec{e}_{MN}^{\,1}$ with both sides of equation (2.25) is integrated over the entire boundary, the result is

$$\begin{aligned} \left(a_{MN}^+ + a_{MN}^-\right) \sqrt{Z_{1,MN}} = & \sum_{qr} \left(b_{qr}^+ + b_{qr}^-\right) \sqrt{Z_{2,qr}} \left\langle \vec{e}_{qr}^{\,2} u_2, \vec{e}_{MN}^{\,1} \right\rangle_{A_1} \\ & + \sum_{uv} \left(c_{uv}^+ + c_{uv}^-\right) \sqrt{Z_{3,uv}} \left\langle \vec{e}_{uv}^{\,3} u_3, \vec{e}_{MN}^{\,1} \right\rangle_{A_1} \end{aligned}, \tag{2.28}$$

where $\left\langle \vec{e}_{bc}^{\,p} u_p, \vec{e}_{MN}^{\,1} \right\rangle_{A_1}$ is the overlap integral $\int_{A_1} \vec{e}_{bc}^{\,p} u_p \cdot \vec{e}_{MN}^{\,1} \, dA$. Leading to a matrix formulation, this equation can be written as

$$\begin{aligned} \left(a_{MN}^+ + a_{MN}^-\right) \sqrt{Z_{1,MN}} = & \sum_{qr} \left(b_{qr}^+ + b_{qr}^-\right) \sqrt{Z_{2,qr}} H_{MN,qr} \\ & + \sum_{uv} \left(c_{uv}^+ + c_{uv}^-\right) \sqrt{Z_{3,uv}} G_{MN,uv}, \end{aligned} \tag{2.29}$$

where $\overline{\overline{H}}$ and $\overline{\overline{G}}$ are matrices whose elements $H_{mn,qr}$ and $G_{mn,uv}$ are the values of the overlap

integrals $\left\langle \vec{e}^{\,2}_{qr} u_2, \vec{e}^{\,1}_{MN} \right\rangle_{A_1}$ and $\left\langle \vec{e}^{\,3}_{uv} u_3, \vec{e}^{\,1}_{MN} \right\rangle_{A_1}$, respectively. By defining the expressions

$$\overline{a} = \begin{bmatrix} a_{M_1 N_1} \\ \vdots \\ a_{M_t N_t} \end{bmatrix}, \overline{b} = \begin{bmatrix} b_{Q_1 R_1} \\ \vdots \\ b_{Q_s R_s} \end{bmatrix}, \text{and } \overline{c} = \begin{bmatrix} c_{U_1 V_1} \\ \vdots \\ c_{U_w V_w} \end{bmatrix}, \tag{2.30}$$

where t, s, and w are the total number of modes in guides 1, 2, and 3 respectively, equation (2.29) can be written even more concisely as

$$\overline{\overline{Z}}_1^{\frac{1}{2}} \left(\overline{a}^+ + \overline{a}^- \right) = \overline{\overline{H}}\, \overline{\overline{Z}}_2^{\frac{1}{2}} \left(\overline{b}^+ + \overline{b}^- \right) + \overline{\overline{G}}\, \overline{\overline{Z}}_3^{\frac{1}{2}} \left(\overline{c}^+ + \overline{c}^- \right). \tag{2.31}$$

The $\overline{\overline{Z}}$ matrices are diagonal impedance matrices with elements $\left(Z^{\frac{1}{2}}_{p,B_1C_1} \cdots Z^{\frac{1}{2}}_{p,B_tC_t} \right)$. The $\overline{a}$, $\overline{b}$, and $\overline{c}$ column matrices contain the modal coefficients for all the modes in their respective guides. While equation (2.31) will hold for any number of modes, an exact solution can only be obtained with an infinite mode set in each guide. Naturally, for most applications, the modes sets must be truncated. In this example, the sets for guides 1, 2, and 3 contain t, s, and w modes, respectively.

The other electric field matrix equations are obtained by taking the scalar product of the eigenmodes for guides 2 or 3 and equation (2.25) and integrating over the appropriate aperture. For guide 2, the equation corresponding to (2.28) is

$$\sum_{mn} \left(a^+_{mn} + a^-_{mn} \right) \sqrt{Z_{1,mn}} \left\langle \vec{e}^{\,2}_{QR} u_2, \vec{e}^{\,1}_{mn} \right\rangle_{A_2} = \left(b^+_{QR} + b^-_{QR} \right) \sqrt{Z_{2,QR}}, \tag{2.32}$$

where there is no term involving guide 3, because the guide 2 and 3 eigenmodes are orthogonal. Note that $\left\langle \vec{e}^{\,2}_{QR} u_2, \vec{e}^{\,1}_{MN} \right\rangle_{A_2}$ is equal to $\left\langle \vec{e}^{\,2}_{QR} u_2, \vec{e}^{\,1}_{MN} \right\rangle_{A_1}$, because $\vec{e}^{\,2}$ only exists over A_2. The equations for guides 2 and 3 corresponding to (2.31) are

$$\overline{\overline{H}}^T \overline{\overline{Z}}_1^{\frac{1}{2}} \left(\overline{a}^+ + \overline{a}^- \right) = \overline{\overline{Z}}_2^{\frac{1}{2}} \left(\overline{b}^+ + \overline{b}^- \right) \tag{2.33}$$

and

$$\overline{\overline{G}}^T \overline{\overline{Z}}_1^{\frac{1}{2}} \left(\overline{a}^+ + \overline{a}^- \right) = \overline{\overline{Z}}_3^{\frac{1}{2}} \left(\overline{c}^+ + \overline{c}^- \right), \tag{2.34}$$

where T denotes the transpose of the matrix.

A similar sequence of steps can be applied to the magnetic field matching equation (2.27). The resulting three equations are

$$\overline{\overline{Z}}_1^{-\frac{1}{2}}\left(\overline{a}^+ - \overline{a}^-\right) = \overline{\overline{H}}\,\overline{\overline{Z}}_2^{-\frac{1}{2}}\left(\overline{b}^+ - \overline{b}^-\right) + \overline{\overline{G}}\,\overline{\overline{Z}}_3^{-\frac{1}{2}}\left(\overline{c}^+ - \overline{c}^-\right) \tag{2.35}$$

$$\overline{\overline{H}}^T\overline{\overline{Z}}_1^{-\frac{1}{2}}\left(\overline{a}^+ - \overline{a}^-\right) = \overline{\overline{Z}}_2^{-\frac{1}{2}}\left(\overline{b}^+ - \overline{b}^-\right) \tag{2.36}$$

and

$$\overline{\overline{G}}^T\overline{\overline{Z}}_1^{-\frac{1}{2}}\left(\overline{a}^+ - \overline{a}^-\right) = \overline{\overline{Z}}_3^{-\frac{1}{2}}\left(\overline{c}^+ - \overline{c}^-\right), \tag{2.37}$$

where the $\overline{\overline{Z}}$ matrices now have elements $\left(Z^{-\frac{1}{2}}_{p,BC}\ldots Z^{-\frac{1}{2}}_{p,B_tC_t}\right)$. The same overlap integrals result because the eigenmode expressions are chosen so that they satisfy

$$\left\langle \vec{h}^2_{QR}u_2, \vec{h}^1_{MN}\right\rangle_A = \left\langle \hat{z}\times\vec{e}^2_{QR}u_2, \hat{z}\times\vec{e}^1_{MN}\right\rangle_A = \left\langle \vec{e}^2_{QR}u_2, \vec{e}^1_{MN}\right\rangle_A. \tag{2.38}$$

The matrix equations can be written in their final and standard form using the definitions

$$\overline{\alpha} = \overline{a} \tag{2.39}$$

$$\overline{\beta} = \begin{bmatrix} \overline{b} \\ \overline{c} \end{bmatrix} \tag{2.40}$$

$$\overline{\overline{M}} = \left[\overline{\overline{H}}\,\overline{\overline{G}}\right] \tag{2.41}$$

$$\overline{\overline{Z}}_\alpha^{\pm\frac{1}{2}} = \mathrm{diag}\left(Z^{\pm\frac{1}{2}}_{1,M_1N_1}\ldots Z^{\pm\frac{1}{2}}_{1,M_tN_t}\right) \tag{2.42}$$

$$\overline{\overline{Z}}_\beta^{\pm\frac{1}{2}} = \mathrm{diag}\left(Z^{\pm\frac{1}{2}}_{2,Q_1R_1}\ldots Z^{\pm\frac{1}{2}}_{2,Q_sR_s}Z^{\pm\frac{1}{2}}_{3,U_1V_1}\ldots Z^{\pm\frac{1}{2}}_{3,U_wV_w}\right). \tag{2.43}$$

The resulting four equations are

$$\left(\overline{\alpha}^+ + \overline{\alpha}^-\right) = \overline{\overline{Z}}_\alpha^{-\frac{1}{2}}\overline{\overline{M}}\,\overline{\overline{Z}}_\beta^{\frac{1}{2}}\left(\overline{\beta}^+ + \overline{\beta}^-\right) \tag{2.44}$$

$$\overline{\overline{Z}}_\beta^{-\frac{1}{2}}\overline{\overline{M}}^T\overline{\overline{Z}}_\alpha^{\frac{1}{2}}\left(\overline{\alpha}^+ + \overline{\alpha}^-\right) = \left(\overline{\beta}^+ + \overline{\beta}^-\right) \tag{2.45}$$

$$\left(\overline{\alpha}^{+} - \overline{\alpha}^{-}\right) = \overline{\overline{Z}}_{\alpha}^{\frac{1}{2}} \overline{\overline{M}}\, \overline{\overline{Z}}_{\beta}^{-\frac{1}{2}} \left(\overline{\beta}^{+} - \overline{\beta}^{-}\right) \tag{2.46}$$

$$\overline{\overline{Z}}_{\beta}^{\frac{1}{2}} \overline{\overline{M}}^{T} \overline{\overline{Z}}_{\alpha}^{-\frac{1}{2}} \left(\overline{\alpha}^{+} - \overline{\alpha}^{-}\right) = \left(\overline{\beta}^{+} - \overline{\beta}^{-}\right). \tag{2.47}$$

The desired scattering matrix parameters are obtained by solving equations (2.44)-(2.45). The scattering parameters are defined by

$$\overline{\alpha}^{-} = \overline{\overline{S}}_{11} \overline{\alpha}^{+} + \overline{\overline{S}}_{12} \overline{\beta}^{-} \tag{2.48}$$

and

$$\overline{\beta}^{+} = \overline{\overline{S}}_{21} \overline{\alpha}^{+} + \overline{\overline{S}}_{22} \overline{\beta}^{-}. \tag{2.49}$$

In only a few simple cases can an exact solution be obtained[60]. In the limit as the number of modes used in each guide approaches infinity, the relation $\overline{\overline{M}}^{T} = \overline{\overline{M}}^{-1}$ becomes true and equations (2.44) and (2.45) become equivalent as do (2.46) and (2.47). However, as the number of modes used must be finite, the expressions exhibit different numerical behavior for truncated mode sets[59]. Since the matrices must be truncated to some finite size in most cases, the relative convergence problem is encountered[60, 59]. A consequence of the relative convergence problem is that different final answers are obtained depending on the number of modes retained in each guide. This problem can be overcome with a proper choice of the ratio of the number of modes in each guide.

By choosing one equation derived from electric field continuity and one from magnetic field continuity, there are eight possible substitutions that lead to expressions for the scattering parameters. Shih[59] provides an in depth analysis of the numerical behavior of each of the eight possible substitutions. For example, a technique that has good numerical behavior and can be used for the step transition problem as well as the bifurcated waveguide example involves first substituting equation (2.44) into (2.47). Solving for $\overline{\alpha}^{-}$ in equation (2.44) and substituting yields

$$\overline{\beta}^{+} - \overline{\beta}^{-} = \overline{\overline{Z}}_{\beta}^{\frac{1}{2}} \overline{\overline{M}}^{T} \overline{\overline{Z}}_{\alpha}^{-\frac{1}{2}} \left(-\overline{\overline{Z}}_{\alpha}^{-\frac{1}{2}} \overline{\overline{M}}^{T} \overline{\overline{Z}}_{\beta}^{\frac{1}{2}} \left(\overline{\beta}^{+} - \overline{\beta}^{-}\right) + \overline{\alpha}^{+} + \overline{\alpha}^{+} \right). \tag{2.50}$$

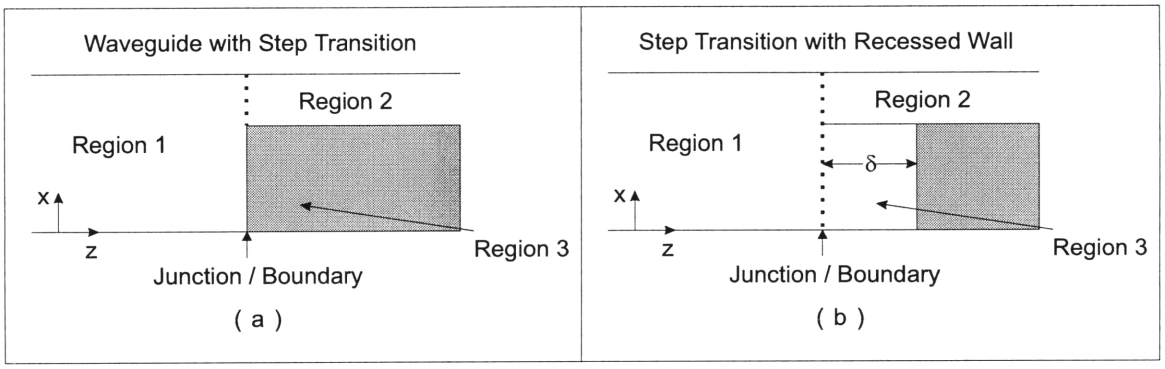

Figure 2-2: *(a) Detail of a waveguide with step transition. Shaded section indicates metal.; (b) Waveguide with step transition where the metal wall has been recessed*

Solving for $\overline{\beta}^+$ yields

$$\begin{aligned}\overline{\beta}^+ = & \underbrace{\left(\overline{\overline{I}} + \overline{\overline{Z}}_\beta^{\frac{1}{2}}\overline{\overline{M}}^T\overline{\overline{Z}}_\alpha^{-1}\overline{\overline{M}}\,\overline{\overline{Z}}_\beta^{\frac{1}{2}}\right)^{-1}\left(\overline{\overline{I}} - \overline{\overline{Z}}_\beta^{\frac{1}{2}}\overline{\overline{M}}^T\overline{\overline{Z}}_\alpha^{-1}\overline{\overline{M}}\,\overline{\overline{Z}}_\beta^{\frac{1}{2}}\right)}_{\overline{\overline{S}}_{22}}\overline{\beta}^- \\ & + \underbrace{2\left(\overline{\overline{I}} + \overline{\overline{Z}}_\beta^{\frac{1}{2}}\overline{\overline{M}}^T\overline{\overline{Z}}_\alpha^{-1}\overline{\overline{M}}\,\overline{\overline{Z}}_\beta^{\frac{1}{2}}\right)^{-1}\left(\overline{\overline{Z}}_\beta^{\frac{1}{2}}\overline{\overline{M}}^T\overline{\overline{Z}}_\alpha^{-\frac{1}{2}}\right)}_{\overline{\overline{S}}_{21}}\overline{\alpha}^+,\end{aligned} \tag{2.51}$$

where $\overline{\overline{I}}$ is the unit identity matrix. Substituting the expression for $\overline{\beta}^+$, (2.51), into equation (2.47) provides the expressions for the the other two scattering parameters

$$\overline{\alpha}^- = \underbrace{\overline{\overline{Z}}_\alpha^{-\frac{1}{2}}\overline{\overline{M}}\,\overline{\overline{Z}}_\beta^{\frac{1}{2}}\left(\overline{\overline{I}} + \overline{\overline{S}}_{22}\right)}_{\overline{\overline{S}}_{12}}\overline{\beta}^- + \underbrace{\left(\overline{\overline{Z}}_\alpha^{-\frac{1}{2}}\overline{\overline{M}}\,\overline{\overline{Z}}_\beta^{\frac{1}{2}}\overline{\overline{S}}_{21} - \overline{\overline{I}}\right)}_{\overline{\overline{S}}_{11}}\overline{\alpha}^+. \tag{2.52}$$

2.2.3 Analysis of a Waveguide with a Step Transition

In order to describe the micromachined horn with an attached circular machined section, the junction between a smaller rectangular and larger circular guide must be analyzed. The transition from a rectangular to a circular waveguide is a specific type of transition called a step transition. A brief analysis of a two dimensional step transition similar to the bifurcated waveguide presented in section 2.2.2 will be given before the three dimensional case is considered. In step transitions, the total waveguide area on either side of the boundary is different. The general mode matching technique used to analyze the bifurcated

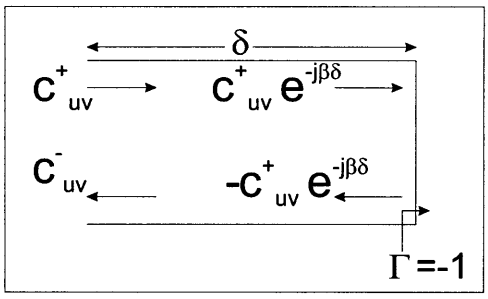

Figure 2-3: *Mode coefficient changes along a waveguide terminated in a short*

waveguide is still valid, but there are a few subtle differences in the specific results.

As shown in Figure 2-2 (a), electromagnetic waves can only propagate in regions 1 and 2. Instead of being a waveguide, Region 3 is a metal waveguide wall. However, in order to implement the mode matching method, an expression for the electric and magnetic fields must be written for the entire boundary. Region 3 can be treated like a waveguide by recessing the wall a small distance δ from the junction. Instead supporting propagating waves that satisfy the radiation condition as $z \to \infty$, region 3 supports standing waves that satisfy the appropriate boundary conditions for an electric wall at $z = \delta$. This method allows an approach to solving the step discontinuity problem that is similar to the bifurcated waveguide problem.

The modes in region 3 have the same transverse dependence as if region 3 were a semi-infinite guide. However, the ratio between the modal amplitude of the forward and reverse propagating wave at the boundary is determined by the phase accumulated from propagation and the reflection coefficient. Figure 2-3 shows that the coefficient c_{uv}^{-} is equal to $-c_{uv}^{+}e^{-j2\beta\delta}$. Therefore, as $\delta \to 0$, the electric field vanishes. This result is expected as the boundary condition (2.5) requires that the tangential electric field vanish on a perfect conductor. Shih[59] presents the equations for finite δ. For the purposes of analyzing the micromachined horn to circular section transition, only the case for $\delta = 0$ is considered.

The electric field equations do not have terms for the modes in region 3. Therefore, the equations corresponding to (2.44)- (2.47) are

$$\left(\overline{\alpha}^{+} + \overline{\alpha}^{-}\right) = \overline{\overline{Z}}_{\alpha}^{-\frac{1}{2}}\,\overline{\overline{H}}\,\overline{\overline{Z}}_{b}^{\frac{1}{2}}\left(\overline{b}^{+} + \overline{b}^{-}\right) \tag{2.53}$$

$$\overline{\overline{Z}}_b^{-\frac{1}{2}}\overline{\overline{H}}^T\overline{\overline{Z}}_\alpha^{\frac{1}{2}}\left(\overline{\alpha}^+ + \overline{\alpha}^-\right) = \left(\overline{b}^+ + \overline{b}^-\right) \tag{2.54}$$

$$\left(\overline{\alpha}^+ - \overline{\alpha}^-\right) = \overline{\overline{Z}}_\alpha^{\frac{1}{2}}\overline{\overline{M}}\,\overline{\overline{Z}}_\beta^{-\frac{1}{2}}\left(\overline{\beta}^+ - \overline{\beta}^-\right) \tag{2.55}$$

$$\overline{\overline{Z}}_\beta^{\frac{1}{2}}\overline{\overline{M}}^T\overline{\overline{Z}}_\alpha^{-\frac{1}{2}}\left(\overline{\alpha}^+ - \overline{\alpha}^-\right) = \left(\overline{\beta}^+ - \overline{\beta}^-\right), \tag{2.56}$$

where $\overline{\overline{Z}}_b$ is the impedance matrix for region 2. The same method of solving for the scattering matrices can be used in the step transition example as in section 2.2.2. This technique would involve substituting equation (2.53) into equation (2.56). An important note on this technique is that equation (2.56) can be written as

$$\overline{\overline{Z}}_\beta^{\frac{1}{2}}\begin{bmatrix}\overline{\overline{H}}^T \\ \overline{\overline{G}}^T\end{bmatrix}\overline{\overline{Z}}_\alpha^{-\frac{1}{2}}\left(\overline{\alpha}^+ - \overline{\alpha}^-\right) = \begin{bmatrix}\overline{b}^+ \\ 2\overline{c}^+\end{bmatrix} - \begin{bmatrix}\overline{b}^- \\ 0\end{bmatrix}. \tag{2.57}$$

This single matrix equation can be written as two equations, one which contains region 2 terms and one which contains region 3 terms. The two equations are

$$\overline{\overline{Z}}_b^{-\frac{1}{2}}\overline{\overline{H}}^T\overline{\overline{Z}}_\alpha^{-\frac{1}{2}}\left(\overline{\alpha}^+ - \overline{\alpha}^-\right) = \left(\overline{b}^+ - \overline{b}^-\right) \tag{2.58}$$

and

$$\overline{\overline{Z}}_c^{-\frac{1}{2}}\overline{\overline{G}}^T\overline{\overline{Z}}_\alpha^{-\frac{1}{2}}\left(\overline{\alpha}^+ - \overline{\alpha}^-\right) = \left(2\overline{c}^+\right). \tag{2.59}$$

The other magnetic field continuity equation (2.55) cannot be separated in this manner. This fact will be important when examining the transition between a rectangular and circular waveguide.

2.2.4 Transition from Rectangular to Circular Waveguide

The analysis of the transition between a rectangular and a circular waveguide as in Figure 2-4 proceeds along the same lines as the analysis for a step transition in a two dimensional guide presented in section 2.2.3. One important difference is that the eigenmodes in region 3 are not known in closed form. Therefore, the overlap integral $\left\langle \vec{e}^3_{UV}u_3, \vec{e}^1_{MN}\right\rangle_A$ is not usually computed. In these cases, the matrix $\overline{\overline{G}}$ is not known. As noted in section 2.2.3,

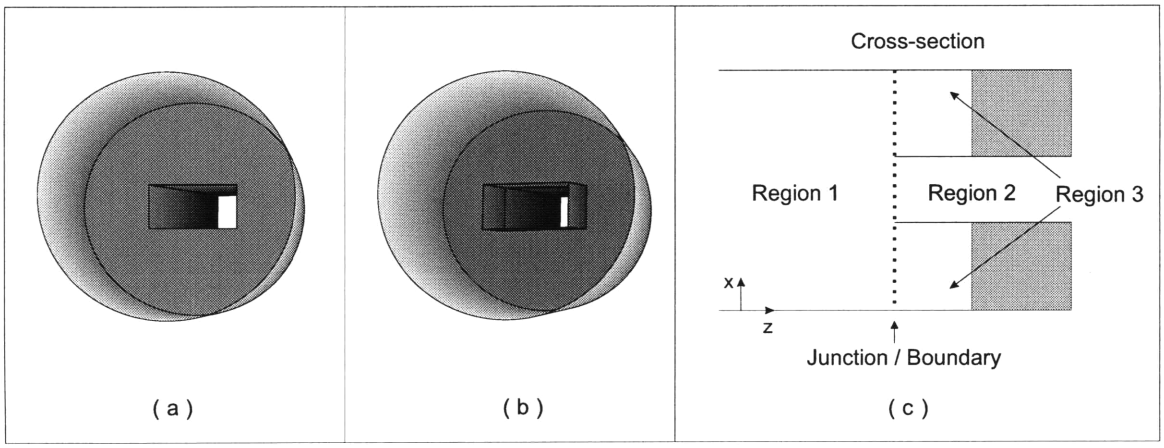

Figure 2-4: *(a) Junction of a rectangular and circular waveguide; (b) Recessed junction used for mode matching analysis; (c) Cross-section of recessed junction*

equation (2.55) cannot be separated into equations which contain terms exclusively from either region 2 or region 3. Therefore, equation (2.55) is generally not used, because it requires knowledge of the elements of matrix $\overline{\overline{G}}$.

In analyzing the transition between a rectangular and a circular waveguide, the major task is the calculation of the overlap integrals between rectangular and circular eigenmodes. While several research groups have reported successful mode matching analysis of rectangular to circular transitions[72, 73, 74, 75, 86, 87], few gave any details. Ke-Li Wu and Robert MacPhie[72] presented a few details, but I discovered that several of the equations and some of the data in the journal article they published are incorrect. Their paper did provide one particularly useful set of expressions which facilitated the computations for the overlap integrals. Wu and MacPhie provided expressions for eigenfunctions of a circular guide in Cartesian vectors and coordinates.

Analysis of this junction proceeds in a manner very similar to the procedure presented in section 2.2.3. In this case, however, the waveguides are three dimensional. The circular guide also supports degenerate sine and cosine modes as explained in appendix section A.2. Therefore, eigenmodes of four different forms (TE sine, TE cosine, TM sine, TM cosine) exist in the circular guide and eigenmodes of two forms (TE and TM) exist in the rectangular guide. Eight different overlap integrals must be calculated, and the matrix $\overline{\overline{H}}$ can be broken down in to eight submatrices.

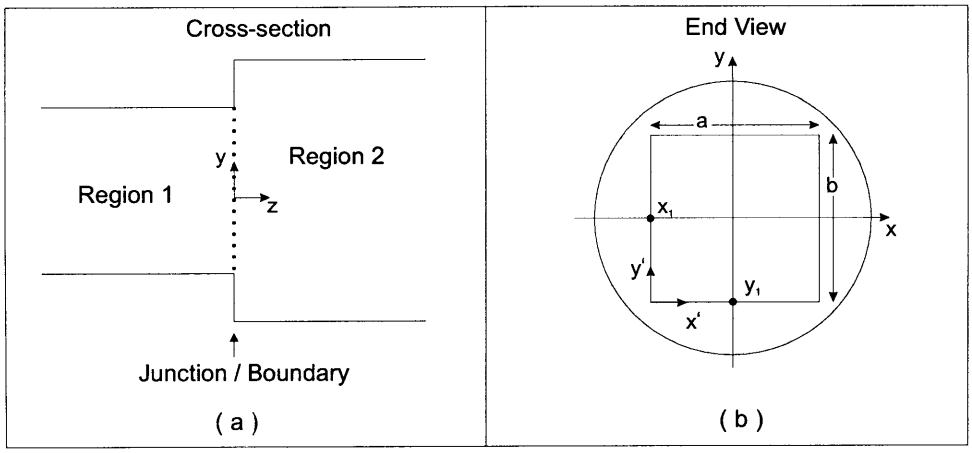

Figure 2-5: *(a) Cross-section of a smaller rectangular waveguide to larger circular guide junction; (b) End view of rectangular to circular waveguide transition with coordinate systems labelled*

In considering the junction of the micromachined horn with the circular machined section, it is more natural to consider the smaller rectangular guide as being region 1 and the circular guide as being region 2, as shown in Figure 2-5 (a). This change is easily accomplished by redefining $\overline{\alpha}$ and $\overline{\beta}$ as

$$\overline{\alpha} = \begin{bmatrix} \overline{a} \\ \overline{c} \end{bmatrix} \text{ and } \overline{\beta} = \left[\overline{b}\right], \tag{2.60}$$

where $\overline{c}$ contains the modal coefficients for the unused region 3 that is now on the same side of the boundary as region 1. With these new definitions equations (2.53), (2.54), and (2.56) can be rewritten as

$$\left(\overline{a}^{+} + \overline{a}^{-}\right) = \overline{\overline{Z}}_{a}^{-\frac{1}{2}} \overline{\overline{M}}^{T} \overline{\overline{Z}}_{\beta}^{\frac{1}{2}} \left(\overline{\beta}^{+} + \overline{\beta}^{-}\right) \tag{2.61}$$

$$\overline{\overline{Z}}_{\beta}^{-\frac{1}{2}} \overline{\overline{M}}\, \overline{\overline{Z}}_{a}^{\frac{1}{2}} \left(\overline{a}^{+} + \overline{a}^{-}\right) = \left(\overline{\beta}^{+} + \overline{\beta}^{-}\right) \tag{2.62}$$

$$\left(\overline{a}^{+} - \overline{a}^{-}\right) = \overline{\overline{Z}}_{a}^{\frac{1}{2}} \overline{\overline{M}}^{T} \overline{\overline{Z}}_{\beta}^{-\frac{1}{2}} \left(\overline{\beta}^{+} - \overline{\beta}^{-}\right). \tag{2.63}$$

The matrix $\overline{\overline{M}}$ has the form

$$\overline{\overline{M}} = \begin{bmatrix} \overline{\overline{H}}^C & \overline{\overline{K}}^C \\ \overline{\overline{H}}^S & \overline{\overline{K}}^S \\ \overline{\overline{Q}}^C & \overline{\overline{E}}^C \\ \overline{\overline{Q}}^S & \overline{\overline{E}}^S \end{bmatrix}, \tag{2.64}$$

where the submatrices that contain the overlap integrals between modes in the circular guide and the rectangular guide. The integrals which define each submatrix can be determined by expanding equation (2.62) as

$$\left(\begin{bmatrix} \overline{b}^+_{C,TE} \\ \overline{b}^+_{S,TE} \\ \overline{b}^+_{C,TM} \\ \overline{b}^+_{S,TM} \end{bmatrix} + \begin{bmatrix} \overline{b}^-_{C,TE} \\ \overline{b}^-_{S,TE} \\ \overline{b}^-_{C,TM} \\ \overline{b}^-_{S,TM} \end{bmatrix} \right) = \overline{\overline{Z}}_\beta^{-\frac{1}{2}} \begin{bmatrix} \overline{\overline{H}}^C & \overline{\overline{K}}^C \\ \overline{\overline{H}}^S & \overline{\overline{K}}^S \\ \overline{\overline{Q}}^C & \overline{\overline{E}}^C \\ \overline{\overline{Q}}^S & \overline{\overline{E}}^S \end{bmatrix} \overline{\overline{Z}}_a^{\frac{1}{2}} \left(\begin{bmatrix} \overline{a}^+_{TE} \\ \overline{a}^+_{TM} \end{bmatrix} + \begin{bmatrix} \overline{a}^-_{TE} \\ \overline{a}^-_{TM} \end{bmatrix} \right). \tag{2.65}$$

The technique presented in section 2.2.2 can be used to solve for the scattering matrices by substituting equation (2.62) into equation (2.63). Appendix B presents the results of this technique.

An alternative to rewriting the field matching equations would be to solve the problem in the direction described in section 2.2.2 and find a relationship between the scattering parameters for the problem solved in the opposite direction. It can be shown that these relationships are

$$\overline{\overline{S}}_{11} = \overline{\overline{S}}'_{22}\,,\ \overline{\overline{S}}_{22} = \overline{\overline{S}}'_{11}\,,\ \overline{\overline{S}}_{12} = \overline{\overline{S}}'^T_{21}\,,\ \text{and}\ \overline{\overline{S}}_{21} = \overline{\overline{S}}'^T_{12}, \tag{2.66}$$

where the solution in one direction is indicated by a $'$ while the solution in the other direction is not.

Appendix B contains a more detailed analysis of the rectangular to circular waveguide transition including computation of matrix elements.

2.3 Generalized Scattering Matrix

The generalized scattering matrix (GSM) technique is similar to the standard scattering matrix theory of circuit theory. The technique extends this general theory to describe both propagating and evanescent modes in multimode structures[60]. The GSM technique is used primarily when a complicated discontinuity can be decomposed in a set of simpler discontinuities[88]. The scatter parameters for each simple junction can be found easily, and then the matrices can be combined to describe the original structure. Generalized scattering matrices can also be cascaded to describe many junctions in series. For two discontinuities separated by some finite distance, the complete scattering matrix can be formed by cascading the two individual matrices with a propagation matrix describing the intervening distance.

The next chapter describes the technique by which the mode matching method and generalized scattering matrix method can be used to design electromagnetic horns.

This page intentionally left blank.

Chapter 3

Design of Millimeter-wave Horn Antennas

Millimeter-wave horn antennas can be designed using the technique of mode matching with generalized scattering matrices. Specifically, electromagnetic modeling of the quasi-integrated horn antennas provides information about the embedding impedance of the detector and about the field distribution at the aperture. From the aperture distribution, standard techniques can be applied calculate the far field pattern of the antenna. The horn antennas can be designed to optimize the far-field pattern and embedding impedance given the available design parameters.

3.1 Mode Matching Analysis of Horn Antennas

The mode matching method along with the use of generalized scattering matrices has been successfully used to describe smooth walled horns. A smooth-walled horn is modeled as a stepped series of waveguides each successive guide having a larger cross section than the previous[56, 67, 80]. This geometry is shown in Figure 3-1. The discontinuity of the junction between two waveguide sections of different cross section can be analyzed using the mode matching method, as described in Section 2.2. The mode matching analysis provides a generalized scattering matrix describing each junction, denoted in Figure 3-1 by a dotted line in the enlargement. The scattering matrix of a junction, e.g. S_1, is

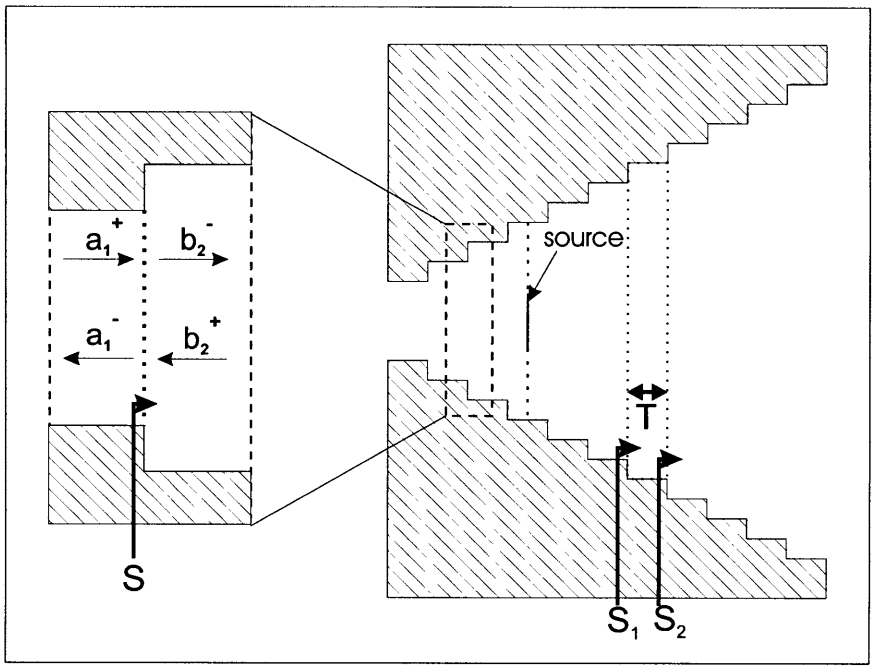

Figure 3-1: *Approximate geometry of a smooth walled horn used for the mode matching method.*

cascaded with a propagation matrix, T, describing the propagation of the modes along the short uniform waveguide section. This combination matrix is cascaded with the scattering matrix for the junction with the next waveguide section, e.g. S_2. By cascading all of the generalized scattering matrices and propagation matrices, a single matrix may be obtained which describes the entire horn structure. Because the mode matching method calculates the effects of higher order evanescent modes in the guides that make up the approximate horn structure, the results are quite accurate as long as enough steps per wavelength are used. In a horn with large flare angle (e.g. 35° half flare angle), approximately seventy (70) sections per wavelength are needed for accurate results[56]. For horns with smaller flare angles (e.g. 9° half flare angle), the number can be much smaller.

Eleftheriades has shown that the mode matching method accurately models the micro-machined horn antennas described in Section 1.2[39, 40, 56]. An overall scattering matrix for the structure on either side of the detector[1] is obtained. The method for using the overall scattering matrices to calculate the currents on the embedded dipole and the excitation

[1]By reciprocity, the antenna can be considered either an emitter (with an embedded source) or a receiver (with an embedded detector).

coefficients of the various waveguide modes is explained in [39, 56]. Modeling the antenna as a source, a unit source voltage is applied across the gap in the center of the embedded dipole. An expression for the source electric field, $\vec{E}_s$, as given in [56] is

$$\int_{S_d} \vec{J}(x',y') \cdot \overline{\overline{G}}\,(x,y,x',y')\,dx'\,dy' = \vec{E}_s = \begin{cases} \frac{-1}{\delta}, & |y| \leq \frac{\delta}{2}, |x| \leq \frac{w}{2} \\ 0, & \text{otherwise,} \end{cases} \tag{3.1}$$

where $\overline{\overline{G}}$ is the dyadic Green's function, S_d is the strip dipole surface, $\vec{J}$ is the dipole surface current, δ is the width of the gap in the center of the dipole, and w is the strip dipole width. The generalized scattering matrix for the antenna on either side of the dipole is used to determine the dyadic Green's function, $\overline{\overline{G}}$. The surface current, $\vec{J}$, on the dipole is expanded in a series of reasonable basis functions. Using equation 3.1 and the method of moments, the coefficients of these basis functions can be determined. Then, using Maxwell's Equations and boundary conditions, the field in the source section can be determined. The generalized scattering matrices can be used to propagate these fields to the aperture. This procedure for calculating the dipole surface currents is not modified by this thesis.

The mode matching method is preferred over other semi-analytical techniques, because the wide flare angle of the micromachined section excites higher order modes and provides strong coupling between modes. More approximate techniques do not model this type of structure well. Completely numerical techniques, such as the Transmission Line Method and method of moments, are much more costly in terms computer resources and computation time. In the more narrowly tapered machined section, approximations can be used to obtain accurate results[56]. In analyzing a gradually tapered waveguide, the modes are assumed to propagate without exchanging energy. This assumption can be verified by using a more accurate method like mode matching or by experiment[80]. In this adiabatic propagation approximation, only the phase of the mode needs to be accounted for according to the formula:

$$\phi = \int_0^L \beta(z)\ dz, \tag{3.2}$$

where $\beta(z)$ is the propagation constant of the mode as a function of z. Thus, the amplitude and phase of all of the modes at the aperture can be determined. Finally, the apertures are

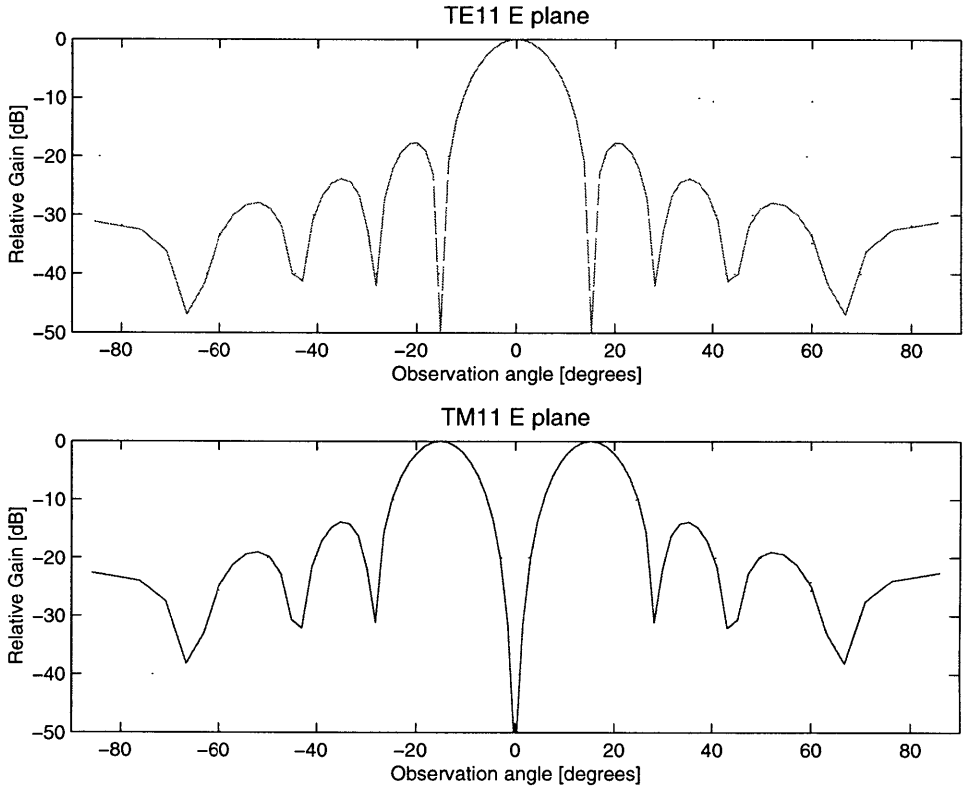

Figure 3-2: *Far-field patterns of the TE_{11}^C and TM_{11}^C waveguide modes.*

assumed to be large enough such that the modes at the aperture are adequately matched to free space such that reflection is negligible.

Once the complex weighting coefficients of the modes at the aperture of the horn can be determined, the problem becomes the design of a multimode horn. In the most famous example of multimode horn design, as Potter[89] noted that, the far-field patterns of the TE_{11}^C and TM_{11}^C modes have similar sidelobe patterns in the E plane as shown in Figure 3-2. TE_{11}^C is the TE_{11} mode in a circular guide, while TM_{11}^C is the TM_{11} mode in a circular guide. Since the TM_{11}^C mode does not have a far-field component in the H plane, the complex ratio of the weighting coefficients of the two modes can be adjusted to cancel sidelobes in the E plane without adversely affecting the H plane pattern.

George Eleftheriades wrote a FORTRAN code to model the quasi-integrated horn. In designing these horns with rectangular sections, an elegant design technique can be employed[56, 90] because the functional forms of the TE and TM rectangular modes are the same. Because the expressions for the TE and TM modes differ only by a constant

factor, expressions for the copolar and crosspolar fields *in the aperture* can be written which result in simple relations between the coefficients of the copolar and crosspolar fields and the coefficients of the modes. (See Section 3.2 for a definition of co- and crosspolarization.) Minimizing the crosspolar power relative to the copolar power results in an antenna with a good beam pattern. It should be noted that zero crosspolar power in the aperture does not correspond to zero crosspolar power in the far field according to the standard definition of crosspolarization[91]. This concept will be explained more fully in Section 3.2.

In this thesis, Eleftheriades's code was modified using the rectangular-to-circular scattering matrix from Section 2.2.4 to model the micromachined horn with embedded dipole and attached circular section. With code to model various geometries, a design methodology was needed to select the best design. Most horn design literature deals with the design of a pure mode or dual mode horn[80]. Even the literature dealing with multimode horns with more than two modes assumes that the most advantageous modes can be excited with the optimum relative ratio[92, 93, 94, 95, 96]. In the design of the micromachined antenna with circular section, relatively little can be done to control which modes are excited. At least four modes in the circular section are excited for any given geometry[2]. While the dimensions of the micromachined section and the location of the dipole within the micromachined cavity could theoretically be modified, Eleftheriades showed that the far-field pattern of a quasi-integrated antenna (micromachined antenna with attached machined section) is relatively insensitive to the location of the dipole within the micromachined cavity[56]. Also, micromachined antennas of a certain geometry were available for testing, so the circular sections were designed taking the micromachined portion as given. Thus, the amplitude of the mode weighting coefficients are determined exclusively by the step transition from rectangular to circular guide. The only design parameters are then the diameter of the throat, the length and the flare angle of the circular section. The two parameters, length and width, both contribute to changing the phase accumulated by the modes when propagating from the throat to the aperture. An iterative design process was used to select an array of test designs. For a given diameter, flare angles from 3^{o} to 12^{o} were tested along with lengths

[2]This minimum number of excited modes occurs when the throat of the circular section circumscribes the aperture of the micromachined section.

from 5λ to 20λ.

3.2 Far-Field Pattern Calculation

The two primary methods of calculating the far-field pattern of an aperture antenna are field radiation and edge diffraction[97]. For electrically large apertures, such as those designed in this thesis, the dominant method of far-field computation is the field radiation method. Using this method, the aperture field distribution is calculated, and a Fourier transformation of this field distribution yields the far-field distribution. For the case of a waveguide radiator, the aperture field is simply the sum of the appropriately weighted waveguide modes. For a horn radiator, the fields will have a phase taper across the aperture that should be taken into account. For narrow flare angle horns as considered in this thesis, this phase taper can be neglected with little effect on the far-field pattern[80]. References [80, 85, 97, 98] all offer slightly different interpretations and paths to obtain the expression. Kong[85] uses the spherical dyadic Green's function and Huygens' principle to derive a rigorous expression. Olver et al.[80] and Balanis[98] use the field equivalence principle and vector potential, while Jull[97] uses the concept of directly decomposing the aperture distribution into plane waves. Essentially the same expressions are derived using each approach. The derivation presented here follows that of Balanis with some notation changes.

By the field equivalence principle, a region with fields in it can be replaced with an enclosing boundary area with sources (e.g. electric and magnetic surface currents) on it. By properly choosing the sources, the fields outside the region are indistinguishable from the initial case of no enclosing boundary[85]. Expression for the electric, $\vec{F}$, and magnetic, $\vec{A}$, vector potentials can be written given the magnetic, $\vec{M}_s$, and electric, $\vec{J}_s$, surface currents, respectively. The expressions are

$$\vec{F} = \epsilon \int_S \int \vec{M}_s \frac{e^{-jkR}}{4\pi R} ds' \tag{3.3}$$

and

$$\vec{A} = \mu \int_S \int \vec{J}_s \frac{e^{-jkR}}{4\pi R} ds', \tag{3.4}$$

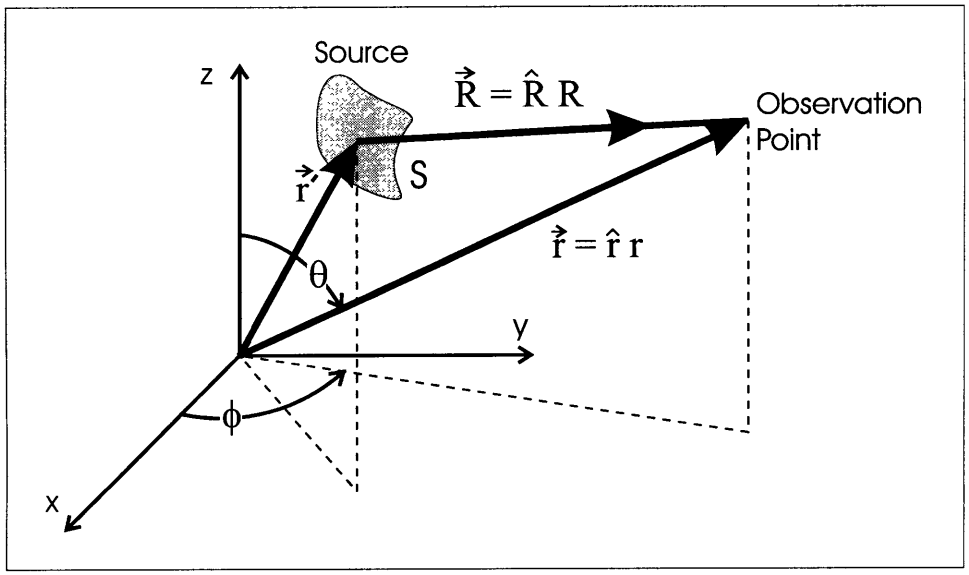

Figure 3-3: *Coordinate system for aperture antenna analysis.*

where S is the enclosing boundary and R is the distance from a source point in the aperture to the observation point in the far field. The coordinate system of the derivation is shown in Figure 3-3. In the far field, the approximation $R \approx r - \hat{r} \cdot r'$ is used in the exponential and the approximation $R \approx r$ is used in the denominator. The resulting vector potentials in the far field are

$$\vec{A} = \frac{\mu e^{-jkr}}{4\pi r} \int\int_S \vec{J}_s e^{j\vec{k}\cdot\vec{r}'} ds' = \frac{\mu e^{-jkr}}{4\pi r} \vec{N} \tag{3.5}$$

and

$$\vec{F} = \frac{\epsilon e^{-jkr}}{4\pi r} \int\int_S \vec{M}_s e^{j\vec{k}\cdot\vec{r}'} ds' = \frac{\epsilon e^{-jkr}}{4\pi r} \vec{L}, \tag{3.6}$$

where $\vec{k} = k\hat{r}$. From the solution to the inhomogeneous vector potential wave equation[98], the radiated fields are then given by

$$E_r = 0 \tag{3.7}$$

$$E_\theta = \frac{-jke^{-jkr}}{4\pi r} (L_\phi + \eta N_\theta) \tag{3.8}$$

$$E_\phi = \frac{jke^{-jkr}}{4\pi r} (L_\theta - \eta N_\phi) \tag{3.9}$$

and

$$H_r = 0 \tag{3.10}$$

$$H_\theta = \frac{jke^{-jkr}}{4\pi r}\left(N_\phi - \frac{L_\theta}{\eta}\right) \tag{3.11}$$

$$H_\phi = \frac{-jke^{-jkr}}{4\pi r}\left(N_\theta + \frac{L_\phi}{\eta}\right), \tag{3.12}$$

where the impedance is $\eta = \sqrt{\frac{\mu}{\epsilon}}$.

As Cartesian coordinates are often used in the aperture, the expressions in rectangular coordinates for N and L are

$$N_\theta = \int\int_S \left[J_x \cos\theta\cos\phi + J_y \cos\theta \sin\phi - J_z \sin\theta\right] e^{j\vec{k}\cdot\vec{r'}} ds' \tag{3.13}$$

$$N_\phi = \int\int_S \left[-J_x \sin\phi + J_y \cos\phi\right] e^{j\vec{k}\cdot\vec{r'}} ds' \tag{3.14}$$

$$L_\theta = \int\int_S \left[M_x \cos\theta\cos\phi + M_y \cos\theta \sin\phi - M_z \sin\theta\right] e^{j\vec{k}\cdot\vec{r'}} ds' \tag{3.15}$$

$$L_\phi = \int\int_S \left[-M_x \sin\phi + M_y \cos\phi\right] e^{j\vec{k}\cdot\vec{r'}} ds' \tag{3.16}$$

where the components of the electric and magnetic surface currents are determined by applying the boundary conditions

$$\vec{J}_s = \hat{n} \times \left(\vec{H}_a - \vec{H}\right) \tag{3.17}$$

$$\vec{M}_s = -\hat{n} \times \left(\vec{E}_a - \vec{E}\right) \tag{3.18}$$

over the enclosing boundary, S, where $\hat{n}$ is the outward pointing normal to the surface. $\vec{E}_a$ and $\vec{H}_a$ are the fields on the outside of the boundary, while $\vec{E}$ and $\vec{H}$ are fields inside the boundary. However, as stated above, the reason for using the enclosing boundary, S, is that the fields inside the boundary do not matter. Therefore, $\vec{E}$ and $\vec{H}$ can both be set to zero, and equations (3.17) and (3.18) can both be written in terms of the aperture fields, $\vec{E}_a$ and $\vec{H}_a$, alone. As written, equations (3.8) - (3.12) contain contributions from both the electric and magnetic fields in the aperture. Image theory can be used to show that these equations can equivalently be written using only an electric or magnetic field model[85, 98]. In the electric field model, the expressions

$$\vec{J}_s = 0 \tag{3.19}$$

and

$$\vec{M}_s = -2\hat{n} \times \vec{E}_a \tag{3.20}$$

are used, while in the magnetic field model, the expressions

$$\vec{J}_s = 2\hat{n} \times \vec{H}_a \tag{3.21}$$

and

$$\vec{M}_s = 0 \tag{3.22}$$

are used. In practice, all of the methods yield results which are only slightly different[80]. In this thesis, the electric field model was used because the mode amplitudes of the electric field at the aperture were calculated in the code.

The measured quantity in far-field measurements is proportional to the radiation intensity, which in normalized form is given by the expression

$$U(\theta, \phi) = \left(|E_\theta(\theta, \phi)|^2 + |E_\phi(\theta, \phi)|^2 \right). \tag{3.23}$$

Often in measurements of antennas which radiate linearly polarized radiation, the copolar and crosspolar components of the far field are desired. Several different definitions of the copolar and crosspolar field are available. The most widely used is Ludwig's third definition[91], which for an electric field primarily along the y direction in the aperture gives the quantities as

$$E_{copolar} = E_{copl} = \sin\phi E_\theta + \cos\phi E_\phi \tag{3.24}$$

$$E_{crosspolar} = E_{xpl} = \cos\phi E_\theta - \sin\phi E_\phi. \tag{3.25}$$

In a general sense, the copolar radiation is "the component of the far field parallel to the polarization of the electric field in the aperture," while the crosspolar radiation is perpendicular to that. This definition of co- and crosspolarization corresponds to the quantities measured in a far-field antenna range. The definition also assumes that the electric field in the aperture is predominantly oriented in the y direction.

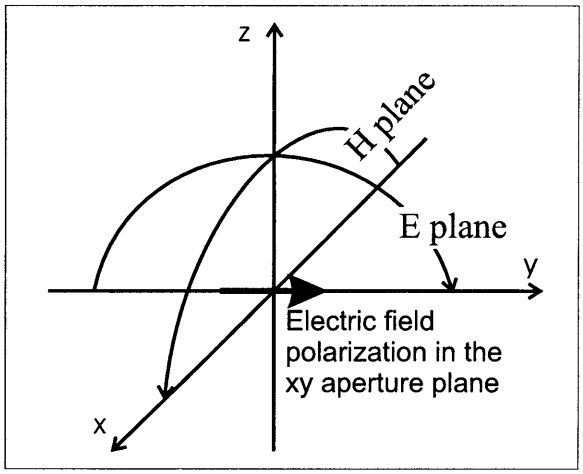

Figure 3-4: *E and H plane definitions for an aperture in the xy plane with an aperture electric field polarized in the y direction.*

Two terms used frequently in the discussion of antenna patterns are the E plane and the H plane. As with the definitions of copolarization and crosspolarization, the definitions of the E and H plane assume that the electric field in the aperture has a preferred direction. As shown in Figure 3-4 for an aperture in the xy plane, the E plane is the plane including the polarization direction, while the H plane is the plane perpendicular to the E plane. Therefore, for the case indicated in Figure 3-4 a measurement of the copolarization in the E plane involves a measurement of the electric field in the yz plane polarized in the y direction. A copolar measurement of the H plane involves a measurement of the electric field in the xz plane that is polarized in the y direction.

The far-field patterns of multimode horns tend to be quite frequency dependent because the pattern depends on the phase relation between different modes. A frequency different from the design frequency means that the apparent lengths of all the components of the antenna are not the design values. For example, measured in wavelengths, the machined section is longer at higher frequencies. Since the different modes have different propagation constants, they will accumulate different phase changes propagating down the machined section. Thus, as the frequency differs more from the design frequency, the relative phases between the modes will differ more from the design values. The effect of a 5 % change in frequency on the E plane pattern is shown in Figure 3-5. The effect on the H plane pattern is shown in Figure 3-6.

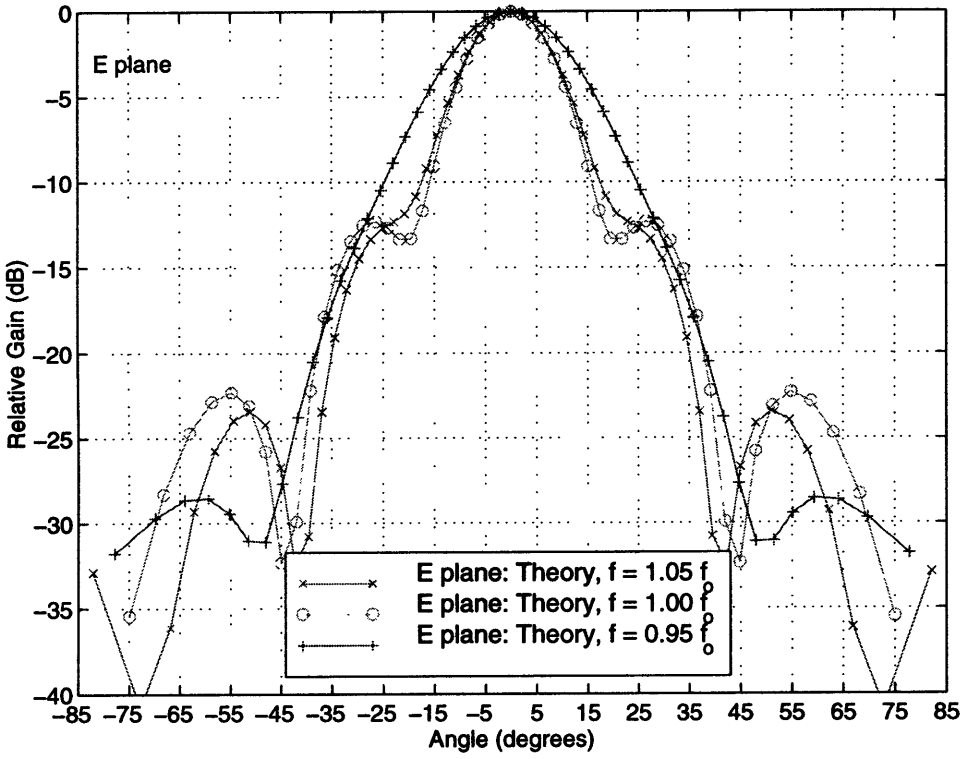

Figure 3-5: *E plane pattern computation for the design frequency, f_o, and $\pm 5\% f_o$. Initial radius* 1.91λ *and half flare angle* $5.67°$.

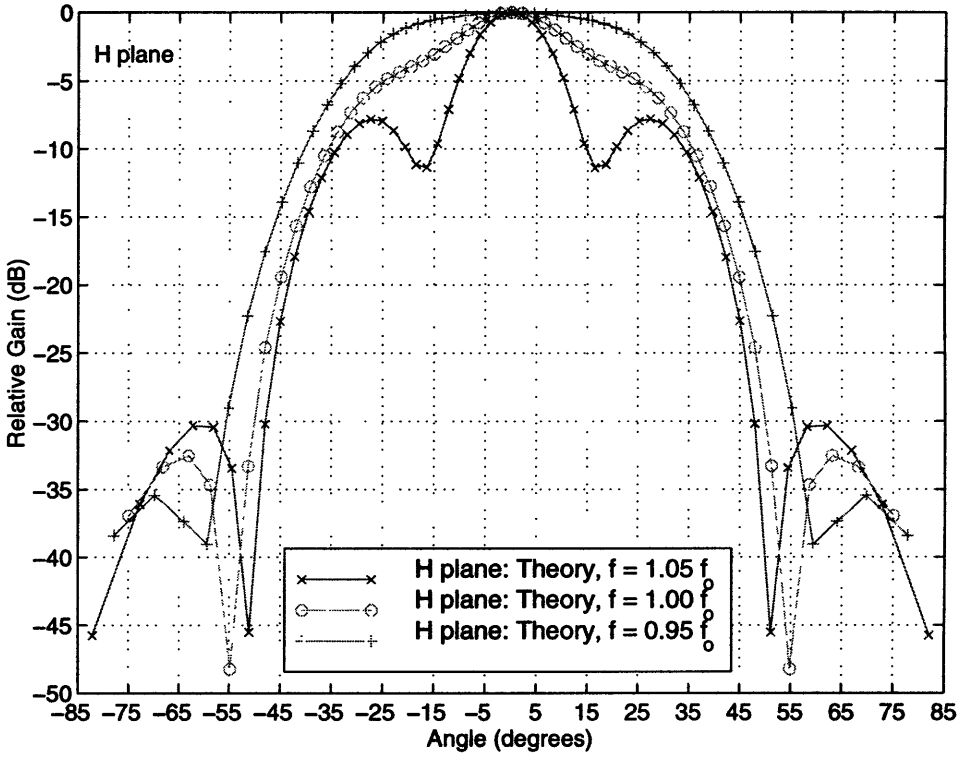

Figure 3-6: *H plane pattern computation for the design frequency, f_o, and $\pm 5\% f_o$. Initial radius* 1.91λ *and half flare angle* $5.67°$.

Table 3.1: *Calculated Embedding Impedance*

Design	Shape	Initial Dimension [λ]	Impedance [Ω]
1	Rect.	1.35	53.3 + j5.7
2-4	Circ.	1.91	60.3 - j3.2
2-4	Circ.	1.81 (5% lower freq.)	43.3 - j30.5
2-4	Circ.	2.00 (5% higher freq.)	70.9 + j18.4
5-6	Circ.	2.45	54.0 + j4.8

3.3 Device Embedding Impedance

As explained in Section 3.1, mode matching can be used to determine the impedance at the terminals of the dipole embedded in the micromachined horn. The knowledge of this impedance is very important as the detector must be matched to the embedding impedance to avoid an impedance mismatch loss. Under the approximation that modes propagate down the gradually flared section without exchanging energy and radiate without reflection (Section 3.1), the impedance is dependent only on the geometry of the micromachined horn and the initial radius of the circular machined section. Calculations of the embedding impedance for the designs presented in Section 3.4 are given in Table 3.1. Impedance values (of designs 2-4) for frequencies within a 10 % bandwith are presented to indicate the frequency dependence of the impedance.

3.4 Circular Section Designs

Circularly symmetric beam patterns with low sidelobes and a narrow main beam that couple well to a Gaussian beam profile are ideal for most applications. Most of the platelet horn designs did not have all of those traits. Designs with these ideal characteristics could not be attained with the available design parameters. By varying some of the other dimensions of the quasi-integrated horn designs, better performance might be attained. The main purpose of the designs selected was to verify the accuracy of the modeling code. The designs for the platelet horn array are in Table 3.2. A rectangular design was made as a calibration for the platelet horn array. If the far-field pattern of the rectangular platelet horn matched the predicted pattern for a smooth walled rectangular horn, then the circular platelet horns can

Table 3.2: *Platelet Horn Designs*

Design	Shape	Initial Dimension [λ]	Final Dimension [λ]	Design Angle [degrees]
1	Rect.	1.35	3.56	9
2	Circ.	1.91	2.89	4
3	Circ.	1.91	3.63	7
4	Circ.	1.91	3.38	6
5	Circ.	2.45	3.43	4
6	Circ.	2.45	3.92	6

Table 3.3: *Actual Platelet Horns*

Design	Initial Dimension [λ]	Actual Final Dimension [λ]	Actual Angle [degrees]
1	1.35	3.14	7.2
2	1.91	2.70	3.2
3	1.91	3.30	5.6
4	1.91	3.10	4.8
5	2.45	3.24	3.2
6	2.45	3.64	4.8

be assumed to be good approximations of smooth-walled circular horns.

The average thickness of the silicon wafers used in the platelet horn fabrication was 0.008" (8 mil). As measurements before the horns were fabricated indicated the the thickness was 0.007" (7 mil), the designs were made for 7 mil wafers. Therefore, for a horn length of 7λ, the aperture diameter was smaller than expected. The result is that the flare angle of the fabricated horns was smaller than the design. The actual dimensions for the platelet horns are given in Table 3.3.

When circular sections were machined, flare angles of 3° and 5° were chosen because tapered end mills are available in these flare angles. A length of 7λ and initial dimensions of 1.91λ and 2.45λ were chosen so that the patterns would be similar to the platelet horn designs.

Chapter 4

Fabrication and Experiment

After formulation of the electromagnetic model of the quasi-integrated horn and design of the circular horn sections, circular sections were fabricated. The circular conical sections were joined with a previously fabricated micromachined section in order to form the quasi-integrated horns. An antenna range and far-field measurement system were designed and built to measure the far field patterns of the horns. By comparing the far field patterns with the predictions of the electromagnetic modeling code, the validity of the electromagnetic model could be determined.

4.1 Fabrication

4.1.1 Platelet Horns

Conventional machining techniques become increasingly difficult as the antenna's operating frequency increases into the millimeter-wave range. In this region, platelet horn technology offers the advantage of using fabrication techniques that can easily produce precise and accurate dimensions. As the platelet horns are made from stacks of thin sheets or wafers, the techniques of chemical etching and laser machining can be used to open apertures in the sheets. Platelet horns have been successfully fabricated in the submillimeter-wave region up to 800 GHz[77].

Laser machining was selected over chemical etching as the method of opening apertures

in the sheets composing the platelet horn. Chemical etching does offer the advantage of using well established photolithographic techniques. However, chemical etching also requires that masks be fabricated which greatly increases the time and expense associated with the fabrication process. Laser machining is much faster than etching, but it does leave residue from the cutting process and a relatively rough inner surface. The cutting residue can be removed by cleaning the wafer after cutting. Laser machining restricts the types of materials out of which the horns can be fabricated, because the extreme heating can cause warping or charring.

Laser Machining

The Hybrid Circuits Lab in Group 63 at MIT Lincoln Laboratory uses a Nd:YAG laser in the construction of hybrid circuits and microelectronic packages. Rick Magliocco offered the use of the laser for the purpose of making platelet horns. The laser has a wavelength of 1.06 μm, and is generally used for cutting ceramics and dielectrics. While tests showed that silicon, aluminum, and stainless steel could also be laser cut, the thin metal wafers tended to warp. Refractory metals that would not experience these problems are an order of magnitude more expensive than any of the three materials tested and were not used. Silicon wafers did exhibit some charring but not as much as the steel sheets. Aluminum could be cut as cleanly as silicon, but it is also difficult to plate with gold. Sufficiently thin aluminum wafers were too warped even before laser machining to make them useful. Silicon wafers as thin as 8 mil (0.008") could easily be obtained. Thus, silicon wafers were chosen as the structural material for this first attempt at fabricating platelet horns. To our knowledge, this experiment represents the first time platelet horns have ever been made with a non-metal.

The laser system in Group 63 consists of a Nd:YAG laser with optics mounted on a computer-controlled translation stage. The control program accepts commands through specially formatted text files. The stage translates above a vacuum mount used to hold the samples in place during processing. I designed and machined a mount on which the silicon wafers could be placed during the laser machining process. The mount was placed on the vacuum stand so that the vacuum would hold the wafers in place during the cutting process as shown in Figure 4-1. The sequence of steps for starting the laser is listed in Table 4.1.

Table 4.1: *Operation steps for Nd:YAG laser at Lincoln Laboratory*

1	Start the control PC. Place the control files in the directory expected by the control program.
2	Execute the control program, ARNOLD.
3	Turn on the small video monitor that allows observation of the cutting in progress.
4	Turn on the laser stage power and adjust cutting parameters.
5	Open the iris completely to approximately 370.
6	Set the beam expander to approximately 65.
7	The 60mm laser output lens should be used and a flow of nitrogen across the lens should be started. The nitrogen helps prevent damage to the lens caused by debris from the cutting process.
8	Turn the laser cooler on before the laser is made operational. After turning the on-off key on the cooler, the cooler light should be lit and the interlock light should be off. If they are both off, press the cooler button and then the interlock button, waiting for the interlock to catch.
9	Adjust the supply current to approximately 33 amps.
10	Use the large foot pedal to activate the vacuum connected to the vacuum mount. The amount of vacuum drawn can be adjusted on the pump.

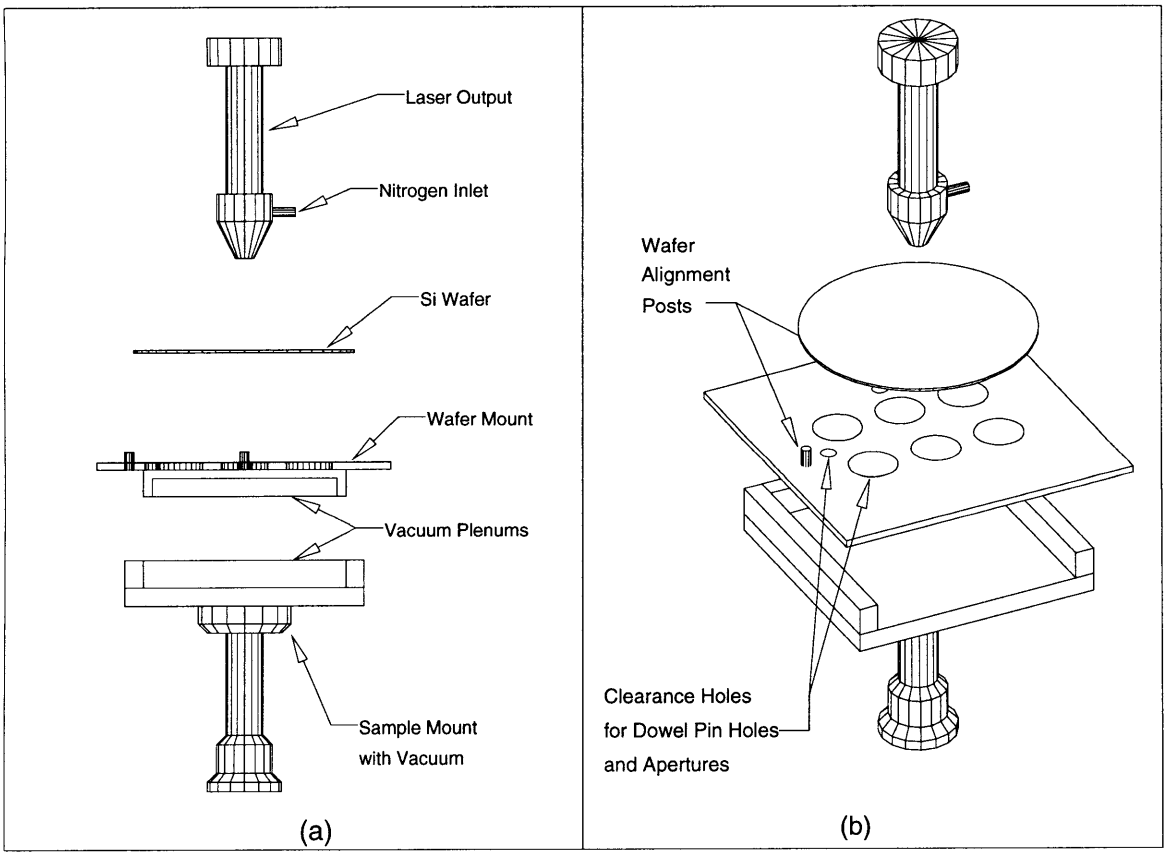

Figure 4-1: *(a) Side view of laser machining setup; (b) Perspective view of laser machining setup*

A diagram of the fabrication setup for laser machining is shown in Figure 4-1. Wafers were placed in a serial fashion on the vacuum mount. The control programs commanded the laser to cut six horn apertures, two dowel pin holes (used for alignment later in the fabrication), and a index number in each wafer. To open apertures in wafers, the laser beam would trace the edge of the aperture to be opened. The part of the wafer within the shape traced by the laser would then fall into the clearance holes in the mount. The laser needed to traverse the apertures between six and nine times in order to completely open apertures in 8 mil silicon wafers. The laser cut through the wafer on the first pass, but the wafer and the portion to be removed would fuse together. For some of the larger apertures, the aperture would not fall away and had to be removed by gently tapping it with a tweezer.

After laser cutting, the wafers were cleaned in a three step process used by Group 63. The wafer to be cleaned is placed in a beaker filled with a Citronox solution. Citronox is a detergent with a mild acetic acid. The beaker is placed in an ultrasonic cleaner for three minutes. The ultrasonic cleaner vibrates the wafer to dislodge residue. Clean-room tissue paper is placed in the beaker to prevent the wafer from breaking due to vibration against the beaker. Water is used to rinse the Citronox solution off the wafer. An acetone rinse removes the water, and then isoproponal is used to remove the acetone. Acetone leaves a residue upon evaporating, while isopropanol evaporates without leaving a residue. Thus, isopropanol is used in the last cleaning step.

After cleaning, the wafers were aligned into stacks. Dowel pins placed in the alignment holes ensure that the wafers line up correctly. Substacks of eight wafers were created as a small number of wafers could be aligned much more easily than the entire stack of fifty-one wafers. Also, as will be explained in the section on metallization, short stacks were needed to ensure that the sidewalls would be adequately covered with gold during sputtering. After metal coating of the substacks, the substacks could easily be aligned to form the complete horn structure. Wafers were glued together using a cyanobond adhesive.

Metallization

While several processes exist for wet plating of gold on silicon[99], the processes are difficult and to our knowledge not readily available on campus at MIT or at Lincoln Laboratory.

Techniques such as evaporation and sputtering are usually used for metal deposition in microelectronics applications[100]. Because the vertical sidewalls of the apertures are critical areas for metal to be deposited, a non-directional deposition process is required. Sputtering is not directional and can be used to cover the sidewalls of holes with an aspect ratio up to 1:1. Evaporation tends to be directional; however, some evaporators are equipped with "shakers" that change the angle of the sample relative to the target enabling sidewall coverage. Since a sputtering system was available in Group 63 at Lincoln Laboratory, sputtering was used for depositing metal on the wafers.

The sputtering system in Group 63 is a d. c. sputtering system using argon. A large d. c. bias is applied between the target (the material to be sputtered, e.g. gold) and the bottom electrode on which sits the sample to be coated, e.g. the silicon wafers. The large voltage creates a strong electric field that strips electrons from the argon atoms. The positively charged argon ions are accelerated to the target, bombarding it and causing atoms of the target to be dislodged. The non-uniform angles at which argon ions strike the target and the number of different interactions that can occur at the surface of the target cause atoms to be ejected from the target at a wide range of angles. This randomness is the characteristic that allows sputtering to be used for coating vertical structures. To help ensure uniform coverage, the stage on which the samples are placed also rotates at approximately 15 rpm.

After pumping the sputtering chamber to approximately 10^{-6} torr to remove most of the water vapor and other impurities, the chamber is back filled with argon to approximately 4 mtorr. To attain better sidewall coverage, sputtering was performed with one side of the wafer facing the target. The wafers are flipped, and sputtering is performed again. For better adhesion, a thin (300Å) layer of TiW is sputtered before the gold. For a rough estimate of the amount of gold that needed to be deposited, the skin depth was calculated using $d_p = \sqrt{\frac{2}{\omega\mu\sigma}} = \delta$, where $\omega = 2\pi f$, μ is the permeability, and σ is the conductivity[85]. For gold, $\sigma = 49 \times 10^{-4}\,(\Omega - cm)^{-1}$[101], and thus, the skin depth at 190 GHz is approximately, $\delta = 0.165\mu m$. However, this figure assumes very low impurity, well-ordered gold, which is not necessarily what results from sputtering. Thus, I wanted to sputter a few skin depths (approximately $0.5\mu m$) with the wafer in each orientation. The amount of gold sputtered was measured by a sensor in the sputtering chamber. The sensor was not properly calibrated,

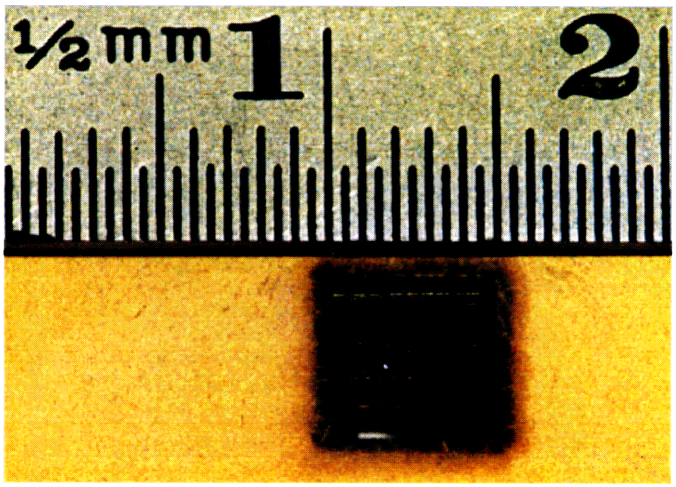

Figure 4-2: *Rectangular platelet horn viewed at an angle. One sidewall can be seen with highlights marking the individual plates. Pre-electroplating.*

though, so less metal was deposited.

Far-field pattern measurements indicated that the platelet horns were very lossy. After deducing that the sidewalls were inadequately coated with gold, I learned of the miscalibration of the sensor in the sputtering system. Only one-third as much gold as desired was deposited. Using the sputtered metal as a base conducting layer, wet plating of gold was performed. Backplating which occurred after the sample was first put into solution resulted in the removal of all the gold from some areas of the horns. The exact rate of plating was unknown for this process, and thus, plating was allowed to occur for several minutes after noticeable buildup was observed. The solution used in gold plating was Techni Gold 25 from Technic, Inc[102]. Five of the six horns had large areas not covered with gold. One possible reason for this lack of coverage is that the sputtered metal did not have good adhesion and came off through backplating into the plating solution. The sputtered metal could have adhered to laser cutting residue that came off at some point in processing. Cyanobond adhesive could have seeped to the center of the wafer and covered the sidewalls preventing gold from adhering. The most likely explanation is that a conduction path did not exist between the electrode and part of the wafers.

Figure 4-2 shows a rectangular platelet horn with ruler for size comparison. Figure 4-3 shows a circular platelet horn. The junctions between the different wafers can be seen as highlights. A region around the aperture of the horn is darker because the sputtered

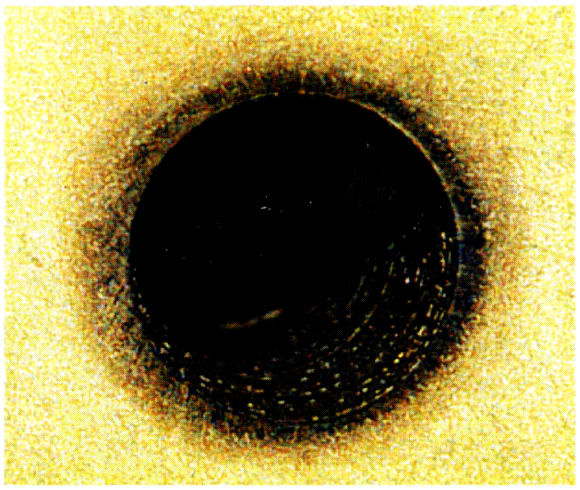

Figure 4-3: *Circular platelet horn viewed at an angle. The sidewalls can be seen with highlights marking the individual plates. Pre-electroplating.*

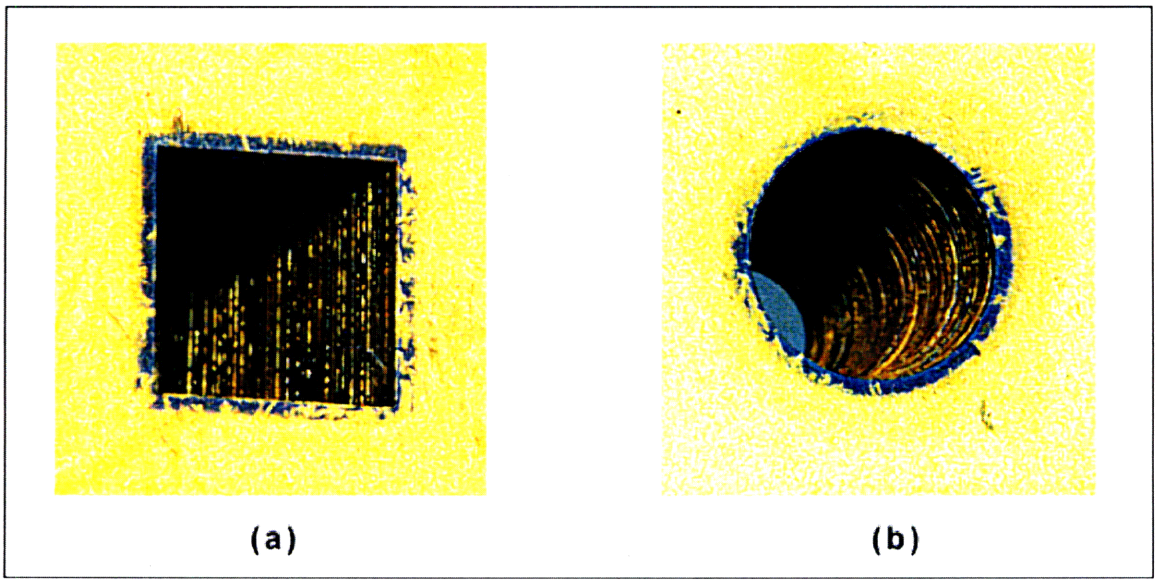

Figure 4-4: *Platelet horns viewed at an angle. Post-electroplating. (a) rectangular horn with large patches uncoated with gold (b) circular horn with nearly uniform gold coating*

gold did not stick to that area as well as to the other areas. The most probable reason for this lack of coverage is that the area near the point of laser cutting was contaminated by debris from the cutting process. A dip in HF (hydroflouric acid) before sputtering could be used to remove this and any other residue. Even though a photograph down a hole will naturally be dark, the inside of these horns are darker than they should be because the layer of gold pre-electroplating is very thin. Comparison with the post-electroplating photograph in Figure 4-4 demonstrates this difference. The post-electroplating photographs illustrate the effect mentioned in Section 4.1.1 in which one of the horns received a uniform coat of gold while the others did not. Regions within the horn covered with gold are gray in a black and white version of the thesis, while uncoated areas are black.

4.1.2 Conventionally Machined Horns

In order to test a method of fabricating conical millimeter-wave horns that would not be faced with the same difficulties as the platelet horns, circular horns were fabricated out of blocks of brass. Even after electroplating, the platelet horns could have suffered from current discontinuity problems. Any small gaps between wafers would prevent current flow. These current discontinuities would violate the assumptions made about the propagation of modes down the platelet horns. Before electroplating, the platelet horns were inspected and small gaps did exist between the wafers. The gaps resulted from not letting the adhesive cure before removing the compressing force on the wafers when the stacks were first formed.

The Laboratory of Nuclear Science (LNS) machine shop performed the fabrication. The designs submitted to the LNS machine shop used 3° and 5° half flare angles, as endmills with those angles are standard, but the horns were actually machined on a lathe. The horns were electroplated in Group 63 at Lincoln Laboratory. To prevent oxides from migrating out of the brass and up through the gold, a nickel flash layer of at least 1.3μm (50 microinches) must be plated before the gold layer. This nickel layer also acts as a good adhesive layer. The nickel solution, Watts Nickel Pure, was obtained from Technic, Inc. The same gold plating solution was used as in the electroplating of the platelet horns.

A photograph of a conventionally machined horn section in Figure 4-5 shows the

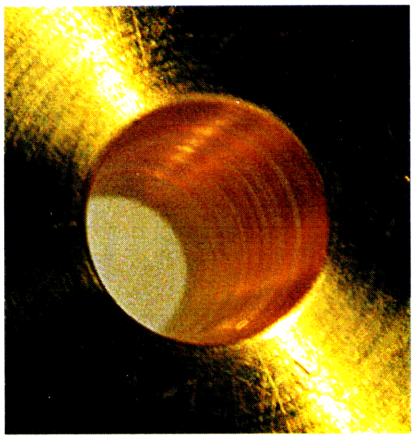

Figure 4-5: *Circular conventionally machined horn viewed at an angle. Gold-plated.*

uniform coating of gold achievable by electroplating metal. Surface roughness from the use of the lathe is evident. The roughness should not distort the fields much though as it is much less than the wavelength of the radiation. The roughness is also much less than that which exists in the platelet horns.

4.2 Experiment

In order to measure the far-field patterns of millimeter-wave horn antennas, an antenna range measurement system was constructed.

Measurement of the far-field pattern of an antenna can be performed by illuminating the antenna under test with uniform plane waves and then rotating the test antenna. Two major types of antenna pattern measurement systems are far-field antenna ranges and compact antenna ranges. A good overview of many subjects related to antenna measurements is provided in [103, 104, 105]. In a far-field range, the assumption that the test antenna is illuminated by plane waves is valid if the curved phase fronts emitted by the source have a large radius of curvature. The standard definition for the far field is that the source and receiver be separated by a distance at least $\frac{2D^2}{\lambda}$, where D is the largest aperture dimension of either the source or receiver[85]. This distance corresponds to a maximum phase error across the aperture of $\frac{\pi}{16}$. Typically, a greater distance than this is used[105]. A second type of antenna range, the compact antenna range, uses a mirror or lens to collimate the

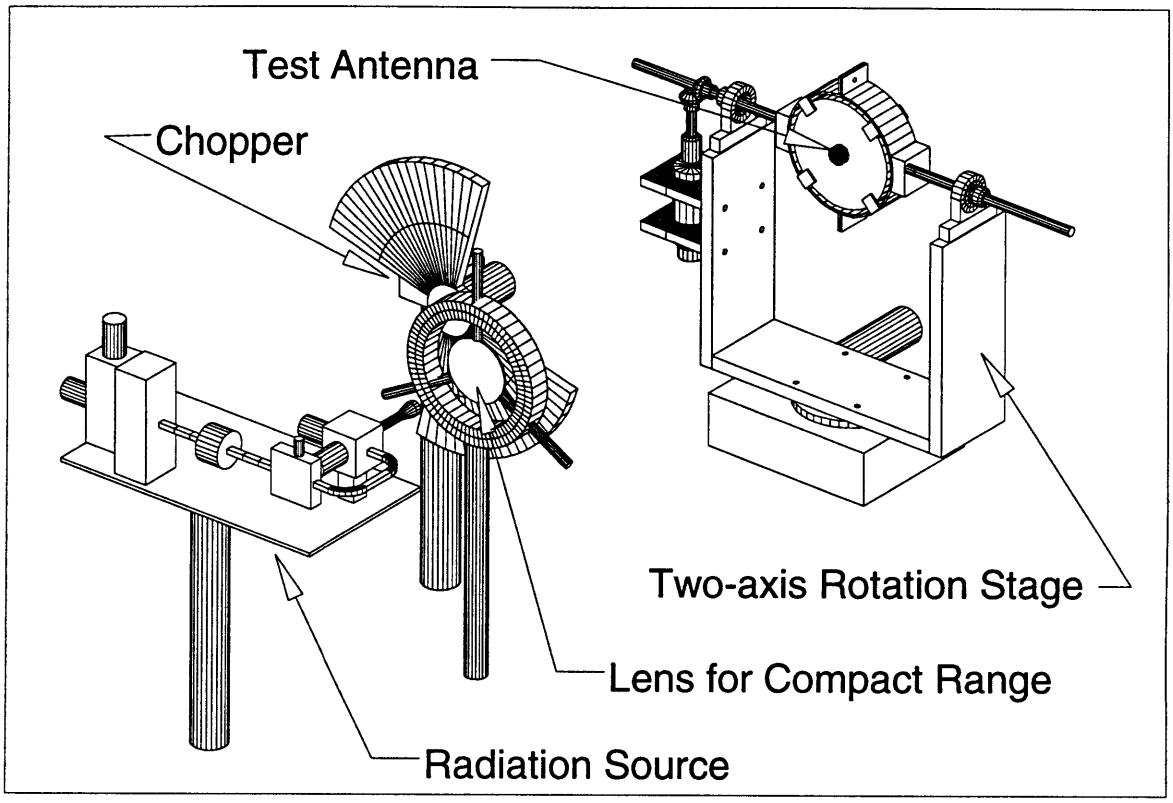

Figure 4-6: *Overview of antenna range system.*

source beam and create a "quiet zone" in which the source radiation approximates a plane wave[106, 107, 108]. Compact antenna ranges are often used at lower frequencies because the $\frac{2D^2}{\lambda}$ distance is extremely large. (Generally, D scales as λ, and thus, $\frac{2D^2}{\lambda} \propto \lambda$.) At millimeter wave frequencies, compact ranges are used when power is scarce, because more of the power emitted by the source is received by the antenna under test. Our measurement facility is configured to perform as both types of ranges. A diagram of the antenna range in compact range configuration is shown in Figure 4-6. For far field range measurements, the lens is removed, and the rotation stage is moved further from the source.

4.2.1 Experimental Setup and Technique

Measurement hardware

The measurement hardware consisted of the basic components of an antenna measurement system, a radiation source, a device to move the antenna in the far field, and a device to

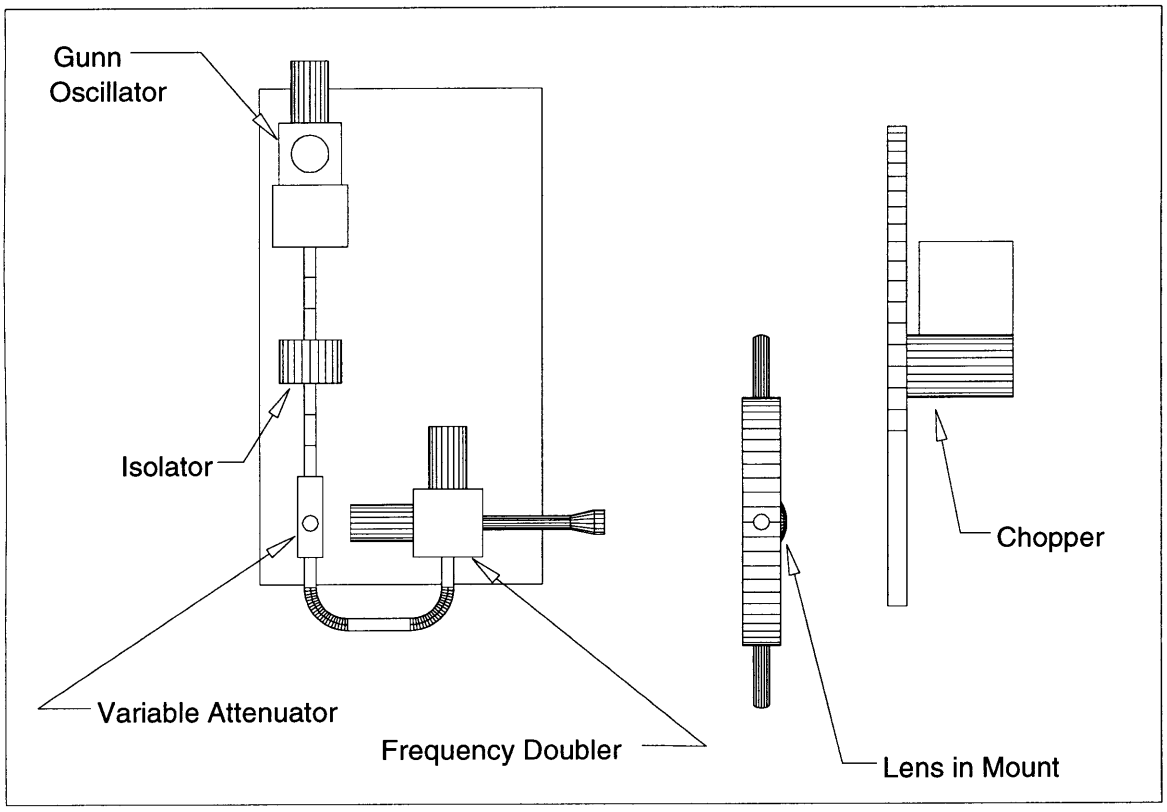

Figure 4-7: *Schematic detail of radiation source, lens, and chopper.*

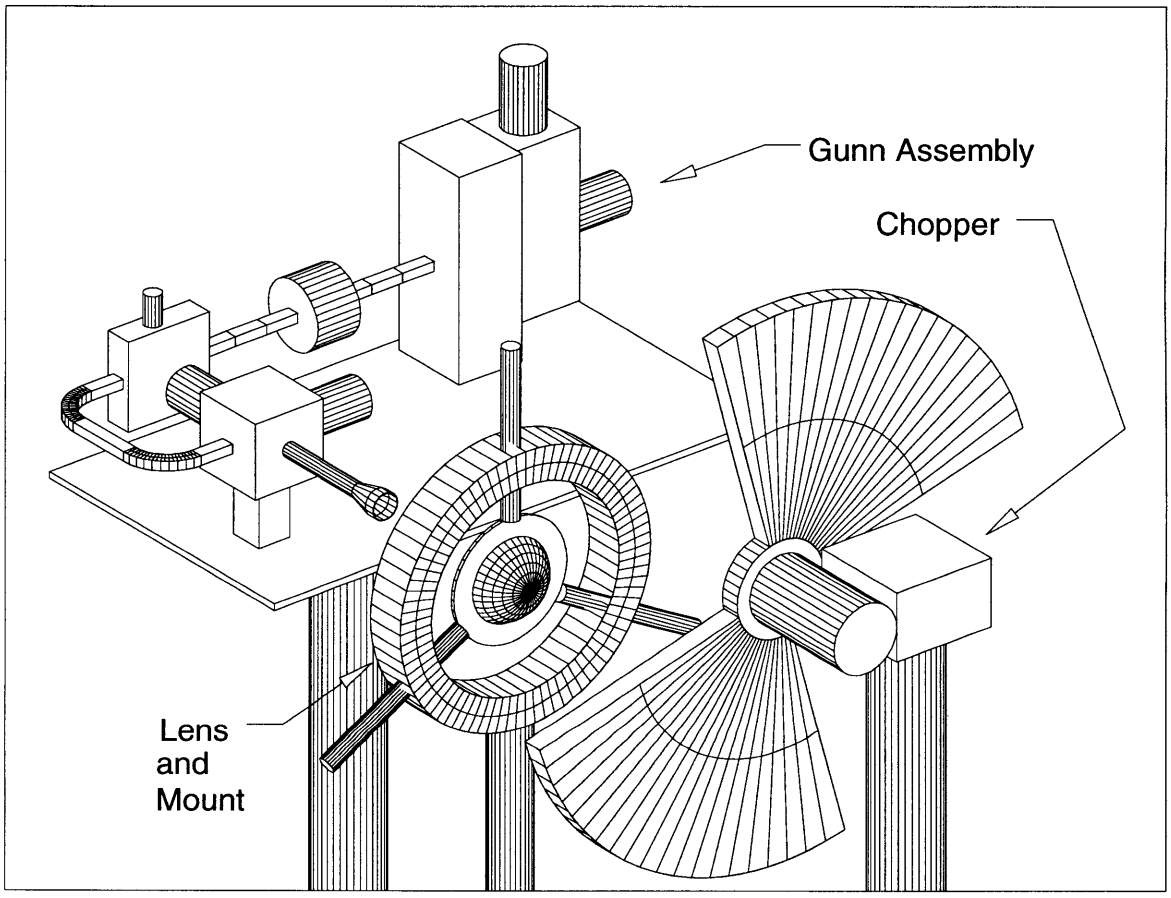

Figure 4-8: *Perspective detail of radiation source, lens, and chopper.*

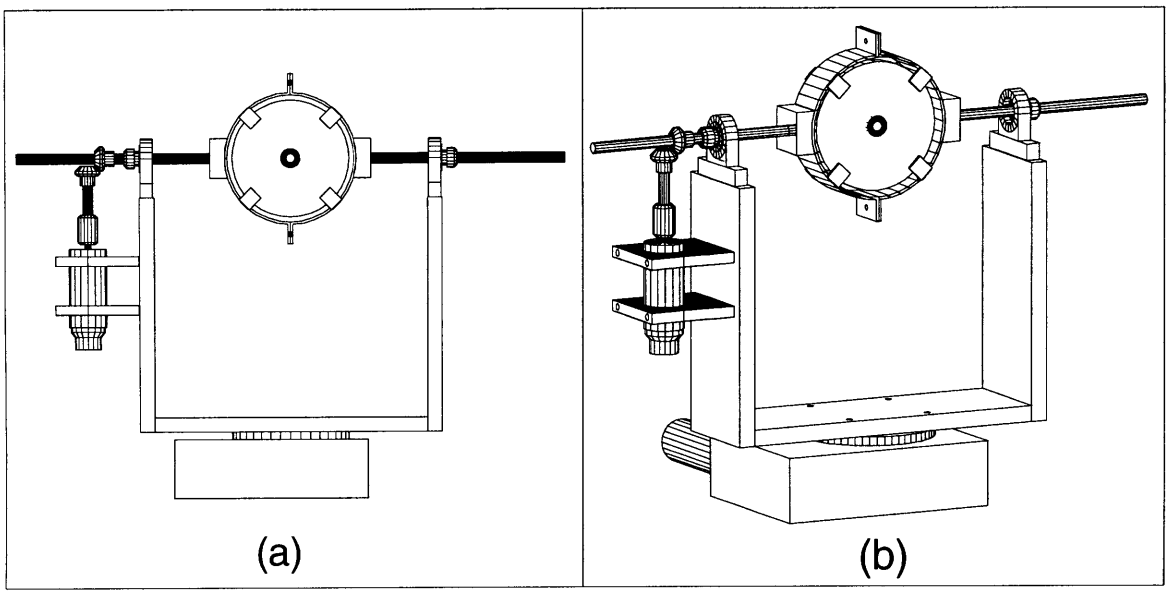

Figure 4-9: *(a) Front view of two-axis rotation stage with test antenna mounted; (b) Perspective view of (a)*

measure the detected radiation.

Radiation is obtained from a whisker diode doubler pumped by a Gunn diode. The frequency of oscillation of the Gunn oscillator can be varied from 77 GHz to 114 GHz. By tuning the Gunn oscillator to 95 GHz, the doubled frequency would be the design frequency of 190 GHz. For this experimental setup, $D \approx 8$mm, so the $\frac{2D^2}{\lambda}$ distance is approximately 75 mm. The distance between the source and receiver must be made much greater than that to avoid reflections off of the equipment and to give the rotation stage adequate clearance for rotation. Because the doubler only has an efficiency of fifteen to twenty percent and the microbolometers that we had were not very sensitive, the measurement range was frequently used in the compact antenna range configuration. The collimating element is an aspherical teflon lens with a 6 cm focal length. The diameter of the lens should be at least three times the size of the antenna under test to ensure that the "quiet zone" adequately covers the antenna under test[103]. A schematic view of the radiation source assembly is shown in Figure 4-7, and a perspective view is shown in Figure 4-8.

In order to traverse the test antenna through all possible angles, a two-axis rotation stage was designed and constructed. The azimuth, or horizontal, rotation is provided by a rotation stage from DynaOptic Motion[109]. Roll, or vertical, rotation is provided by a

d.c. motor coupled to a shaft by anti-backlash mitered gears. A CAD drawing of the stage with a test antenna mounted is shown in Figure 4-9. In Figure 4-9, the test antenna is the small circular section centered at the intersection of the two axes of rotation. The larger circular section around it is simply a spacer. This configuration was used when testing the conventionally machined antennas. The platelet horns were cut into three inch silicon wafers which fit into the clamps without the need for a spacer. Rotation in both directions is controlled by a motor controller also from DynaOptic Motion. The motor controller can be commanded through a GPIB (General Purpose Interface Bus) by using a PC. Rotation of the test antenna in the two axes measures the copolar and crosspolar radiation by Ludwig's Third Definition[91]. To measure copolar radiation, the dipole must be aligned with the polarization direction of the source. To measure crosspolar radiation, the dipole should be rotated 90° from the polarization direction of the source. Definitions of the copolar and crosspolar field as well as the E and H planes are given in Section 3.2.

In the standard configuration, the radiation from the source was polarized vertically. Thus, the orientation of the dipole must be vertical in order to measure the copolar field. An azimuthal sweep of the rotation stage measures the H plane. A roll of the antenna on the axis of the shaft is required for measurement of the E plane. Because a vertical roll causes the antenna to point at the top and bottom of the range which are at different distances from the test antenna, the measurement is not completely symmetric. Being able to measure the E plane with an azimuthal rotation is desirable. In order to make an E plane measurement by performing an azimuthal rotation, a wire grid polarizer is used to change the polarization of the source and the test antenna is rotated 90°. By using a polarizer, the power available is reduced, and the radiation has components in both orthogonal polarizations (horizontal and vertical). Thus, the received power includes a contribution from crosspolarization. Since the measured crosspolar level of the horn peaks at -13dB and falls off at least as fast as the copolar pattern, the effect is negligible.

The detecting element was a niobium (Nb) microbolometer located at the center of the dipole on the Si_3N_4 membrane in the micromachined cavity, as shown in Figure 1-2. As shown in the schematic of the measurement system, Figure 4-10, the microbolometer is supplied with a constant bias voltage. Incident radiation heats the bolometer and causes its

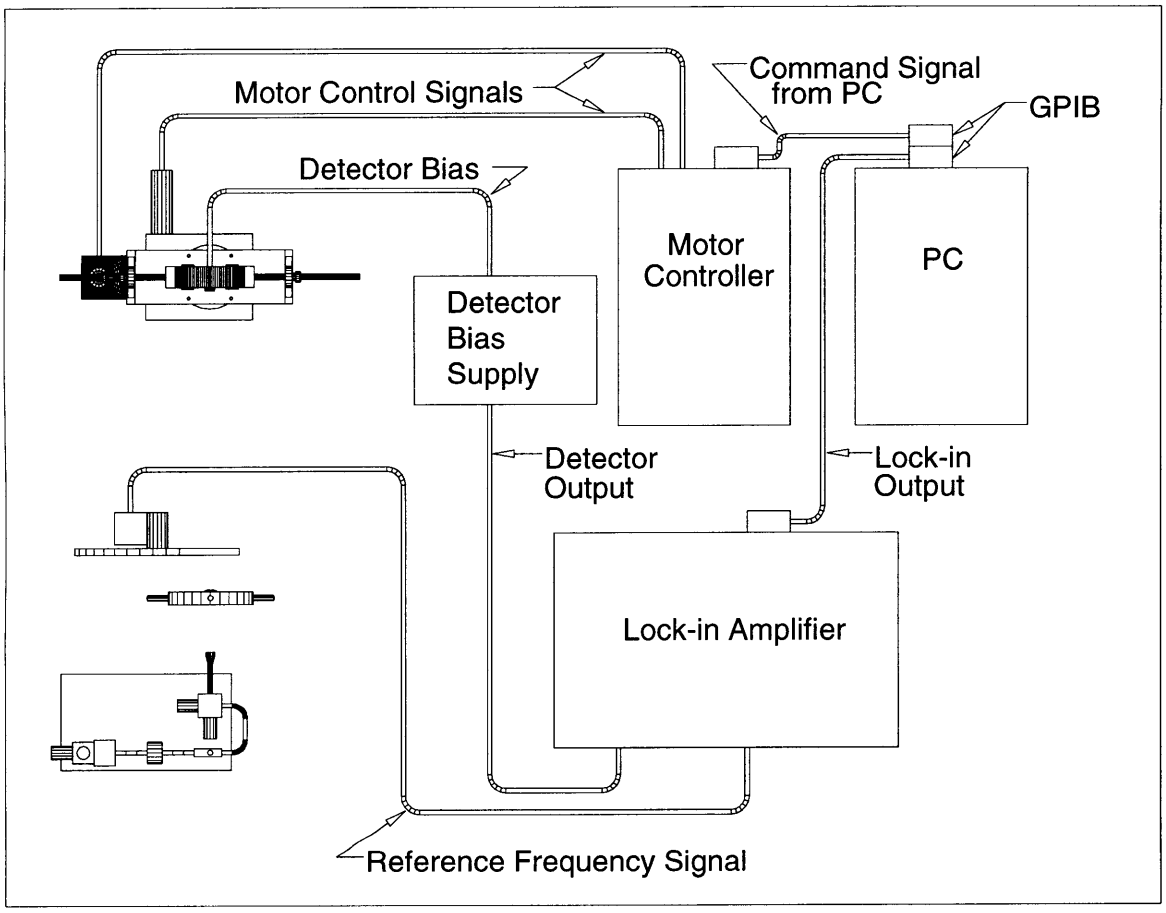

Figure 4-10: *Schematic of entire measurement configuration.*

resistance to change, which causes the current through the device to change. The source beam is periodically blocked with a rotating chopper and the reference signal from the chopper is fed into a lock-in amplifier along with the output signal, i.e. the current through the device. The lock-in uses the reference signal from the chopper to implement a very narrowband filter, so that the detector signal is separated from the noise. The output signal from the lock-in can be read by the controlling PC. The dynamic range of the measurement is the ratio between the maximum output signal and the noise signal.

Measurement software

A personal computer (PC) is used to control the entire measurement system, as shown in Figure 4-10. A General Purpose Interface Bus (GPIB) connects the PC, the motor controller, and the lock-in amplifier. Thus, the PC can both direct the movements of the motors and read the output from the lock-in. A LabView program to coordinate controlling motor movement and taking measurements was written by Arifur Rahman and enhanced by Konstantinos Konistis. The antenna under test can be scanned through either or both of the angles. By centering the test antenna and then scanning in either of the two orthogonal directions, the principle planes (E and H) can be measured.

Measurement Procedure

In order to perform far-field measurements, the circular horn designs had to be attached to the micromachined portions to form a complete quasi-integrated horn. Single elements of a micromachined Nb bolometer array fabricated by Arifur Rahman were used for this purpose. Two difficult procedures were required, i.e., joining the two horn sections and connecting the bias lines to the bias pads on the back side of the device. Research scientist, Gerhard de Lange, provided many useful suggestions and tips in all aspects of the measurement procedure, especially in this area of aligning and affixing the two sections of the quasi-integrated horn. To connect the bias lines, thin copper wires were attached to the pads using room-temperature curing silver epoxy. To join the circular section to the micromachined horn, the horns had to be aligned from the front side, flipped over, and then affixed from the back side, as the circular sections were larger than the bolometer array. The conventionally

machined rectangular section was smaller than the array and had to be affixed from the front side. Putting adhesives on the front of the bolometer array is very risky as was discovered by performing this procedure. Acetone removed the silver paint used to provide adhesion between the machined and micromachined section. However, this solution ran into the micromachined horns covering the membrane with a thin layer of silver and ruining some devices. Therefore, a different, temporary but strong adhesive had to be used to hold the two sections of the quasi-integrated horn together while they were flipped. A very thin layer of vacuum grease was found to provide sufficient adhesion. Once the sections were flipped over, bees wax was heated and poured onto the joint, forming a bond strong enough to hold the two sections together. Gerhard de Lange had used a similar technique previously.

After joining the circular section and the micromachined horn to form a complete quasi-integrated horn, the horn was mounted on the two-axis rotation stage shown in Figure 4-9. The circular clamps on the rotation stage were designed to hold the three inch silicon wafers used to make the platelet array. Thus, for the single element machined horns, a spacer was used to place the horn in the center of the clamp.

With the antenna range in far-field configuration, the two-axis rotation stage was moved by hand to find the center of the quiet zone. When the test antenna was aligned to the source, the lens could be used to increase power received by the antenna. The source was chopped with the chopper signal fed to the lock-in amplifier as a reference signal. The devices were biased with 0.5 - 1.5 mA. The device impedance varied from 70Ω to 180Ω. The current signal from the device was amplified and sent to the lock-in amplifier for detection. Because the resistance of the device changed when illuminated, the current signal would change at the same frequency as the chopper. Therefore, by using the reference signal from the chopper, the lock-in could detect the proper signal. The magnitude of the signal was assumed to be linearly proportional to the received power, as is true for bolometric detectors. This magnitude was the quantity read by the PC to determine the beam pattern of the horn antenna. The software described previously was used to control the entire process.

4.3 Data

The far-field patterns of conventionally machined and platelet horns with rectangular and circular cross-section were measured. The horns with rectangular cross section could be used as calibration standards because the accuracy of the far-field pattern prediction code of George Eleftheriades had been previously verified. The accuracy of the measurement range in compact range as well as far-field range configuration was verified through the testing of quasi-integrated horns with rectangular machined sections as shown in Figures 4-11 to 4-15. The validity of assuming that platelet horns can approximate smooth-walled horns was tested by measuring quasi-integrated horns with rectangular platelet sections as in Figure 4-16. Quasi-integrated horns with circular platelet horns were tested to determine the validity of the modeling code as in Figures 4-17 to 4-20. Finally, in Figures 4-21 to 4-24, quasi-integrated horns with circular machined sections were tested as an additional check of the modeling code and as another evaluation of the validity of assuming platelet horns adequately approximate smooth-walled horns.

If the test antenna is not exactly aligned with the source at the beginning of a measurement, the peak of the measured pattern would not occur at 0°. In these measurements, the data were centered so that the peak of the main beam corresponded to a 0° observation angle. Shifting the pattern was accomplished by duplicating the leftmost or rightmost data point, as appropriate. Therefore, a series of equal data points at one extreme of the pattern indicates that the pattern was shifted.

A list of the data figures along with the key features of each measurement is presented in Table 4.2.

4.3.1 Rectangular Machined Horn

The micromachined section with rectangular machined section has been well characterized[56, 53]. By measuring the far-field patterns of this configuration, the accuracy of the antenna range could be verified. For definitions of copolarization, crosspolarization, E plane, and H plane, see Section 3.2.

Initially, the beam pattern of the rectangular platelet horn was measured. The beam

Table 4.2: *Far-field measurement figures.*

Figure	Horn Cross-Section	Machining Method	E or H Plane	Comment
4-11	rectangular	conventional	H plane	compact range
4-12	rectangular	conventional	H plane	far-field range
4-13	rectangular	conventional	H plane	crosspolar level
4-14	rectangular	conventional	E plane	compact range
4-15	rectangular	conventional	E plane	with polarizer
4-16	rectangular	platelet	H plane	compact range
4-17	circular	platelet	E plane	pre-electroplating
4-18	circular	platelet	H plane	pre-electroplating
4-19	circular	platelet	E plane	post-electroplating
4-20	circular	platelet	H plane	post-electroplating
4-21	circular	conventional	E plane	smaller init. radius
4-22	circular	conventional	H plane	smaller init. radius
4-23	circular	conventional	E plane	larger init. radius
4-24	circular	conventional	H plane	larger init. radius

pattern agreed with the predictions, but the power received was extremely low. The machined rectangular horn was then tested for calibration purposes. At least five times as much signal could be received using the machined section as with the platelet horn.

H plane measurements of the rectangular machined section shown in Figure 4-11 provided verification that the antenna range could be used to make accurate far-field measurements. This measurement was made with the compact antenna range configuration indicating that the lens was large enough not to cause distortion of the far-field pattern. The variations $3^o - 4^o$ on either side of the peak of the beam are due to standing waves between the face of the horn flange and the source. In this configuration, the dynamic range is approximately 25 dB.

H plane measurements were also taken with the range in the far-field configuration, i.e. without a lens, to verify conclusively that the lens did not distort the far-field pattern. As shown in Figure 4-12, the measured pattern agrees very well with predictions and thus with the compact range measurements as well. The dynamic range of this measurement was only 15 - 20 dB, however. A significant portion of the source power was lost without the use of the lens to collimate the source beam. From this measurement, one can conclude that the compact antenna range is a valid measurement system. This conclusion is important for measurement of the platelet horns as the available and received power is not as high as

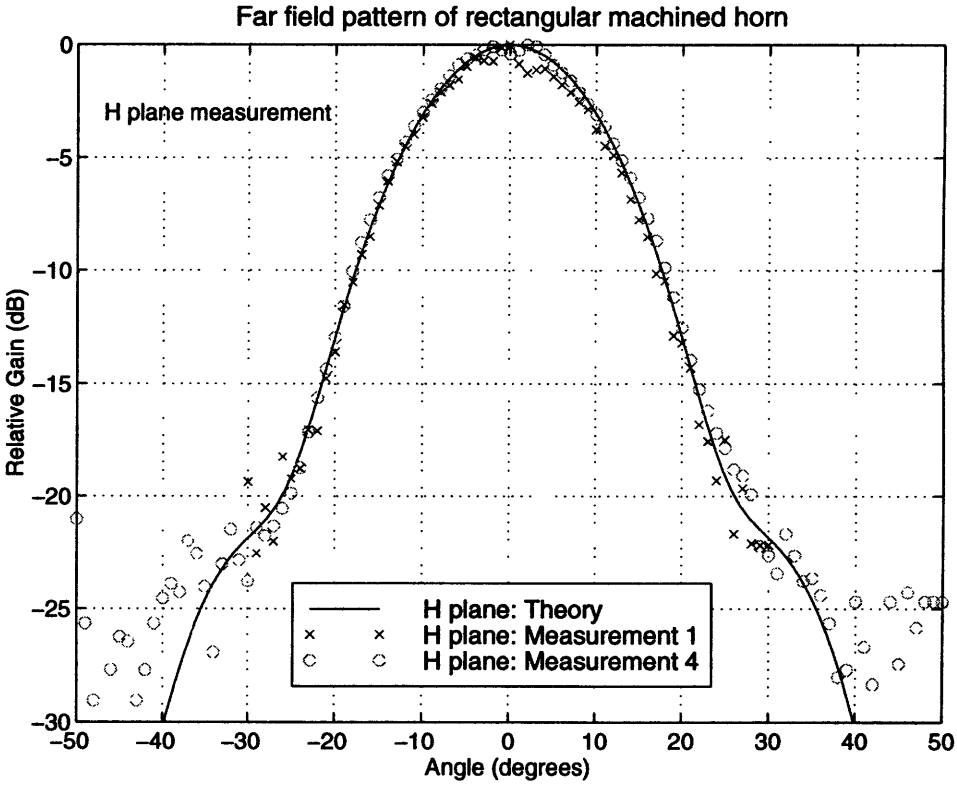

Figure 4-11: *H plane pattern of rectangular machined horn. Compact range measurement. This horn had a half flare angle of* 9° *and initial side of* 1.35λ.

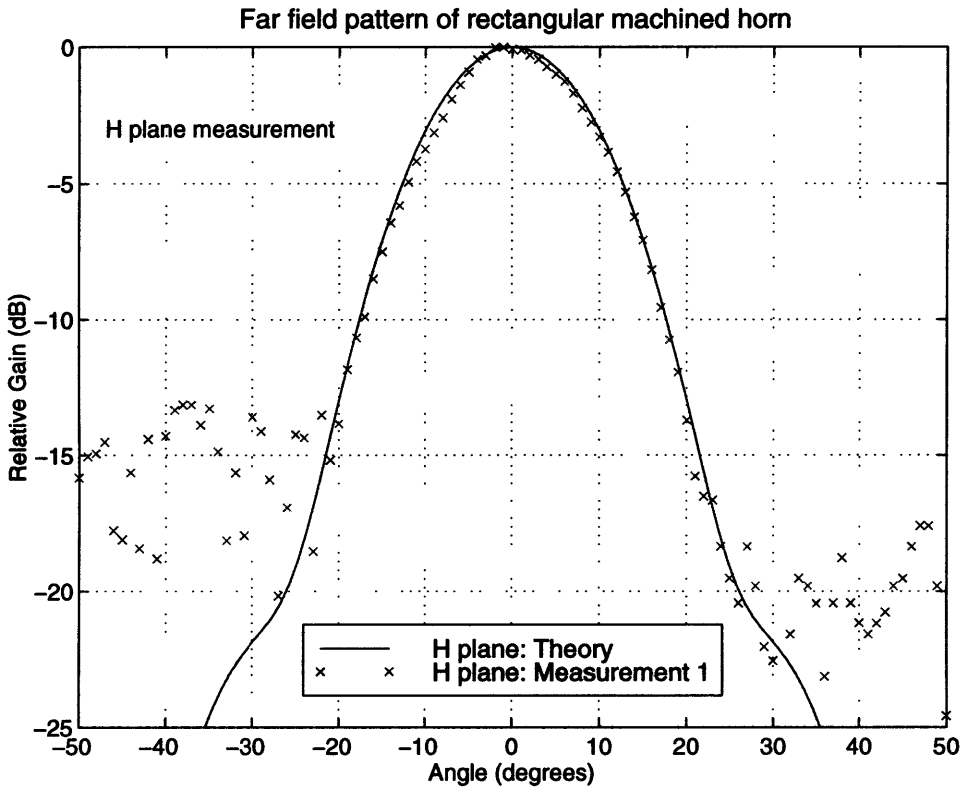

Figure 4-12: *H plane pattern of rectangular machined horn. Far-field range measurement. This horn had a half flare angle of* 9^{o} *and initial side of* 1.35λ.

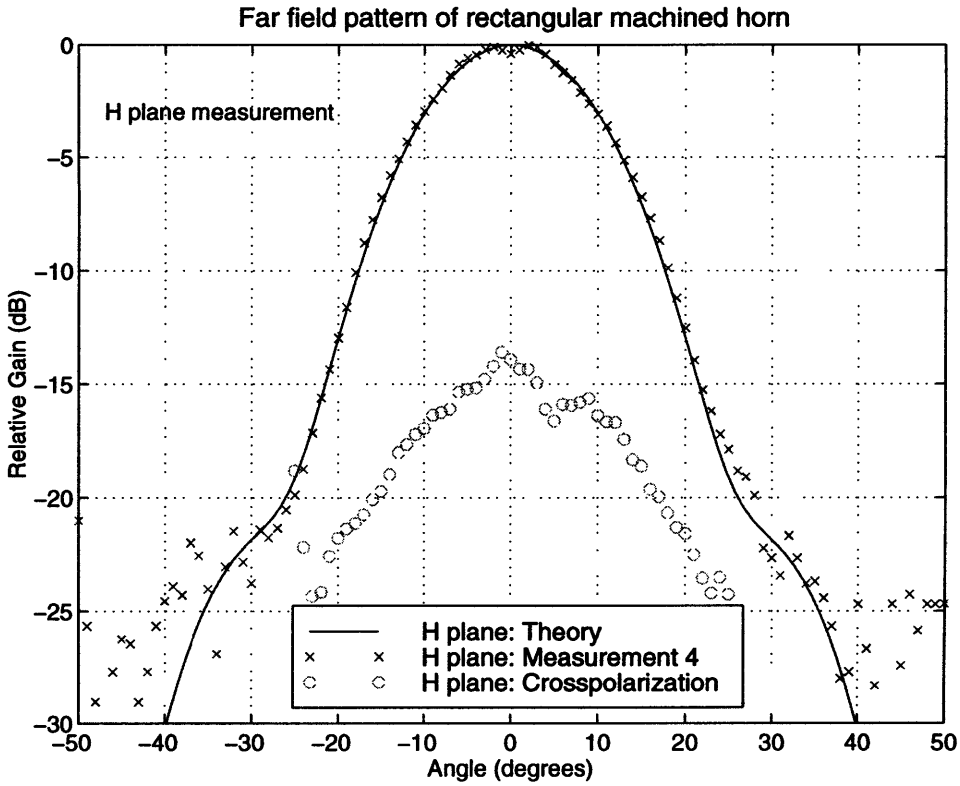

Figure 4-13: *H plane pattern of rectangular machined horn. Compact range measurement. This horn had a half flare angle of* 9° *and initial side of* 1.35λ.

with the machined horns.

Finally, the crosspolar level in the H plane was measured. The crosspolar level is shown in Figure 4-13 along with a measured copolar level. Even though Eleftheriades's code predicts zero (-60 dB) crosspolarization for the principle planes, the higher measured level is not surprising. Idealizations in electromagnetic models tend not to affect copolar predictions as much as crosspolar predictions[110]. Also, because measuring the crosspolarization required rotating the test antenna and was not performed with the exact same alignment of all the apparatuses as the copolarization measurement, the level of the crosspolarization with respect to the copolarization could be in error.

E plane patterns did not agree as well with the predictions of Eleftheriades's code. As shown in Figure 4-14, the measured patterns tracks the theory for approximately 5 dB before deviating. If the manner of deviation is asymmetric, the deviation is probably due to the experimental configuration. (A computation error would most probably imply that

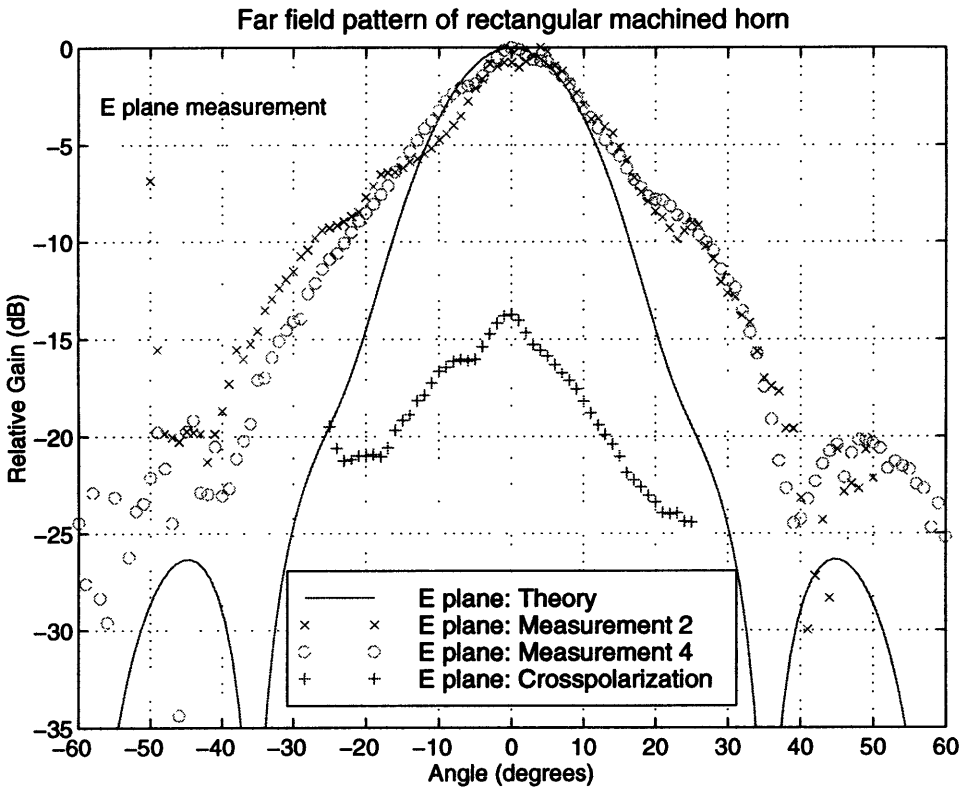

Figure 4-14: *E plane pattern of rectangular machined horn. Compact range measurement without polarizer. This horn had a half flare angle of* 9° *and initial side of* 1.35λ.

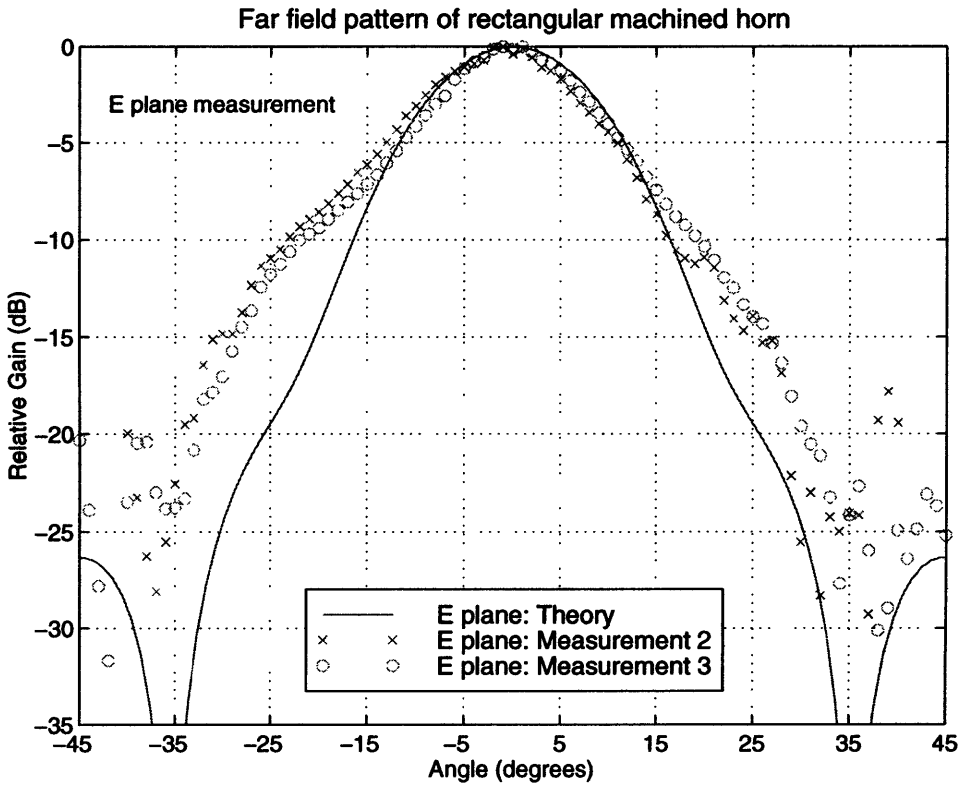

Figure 4-15: *E plane pattern of rectangular machined horn. Compact range measurement with polarizer. This horn had a half flare angle of* 9° *and initial side of* 1.35λ.

the weighting of a particular mode was incorrect. Since all the modes are symmetric about $\theta = 0$ in the principle planes, asymmetries must be due to misalignments or measurement errors.) Scattering from the metal mount of the horn or from another apparatus probably accounts for the asymmetry. As explained in Section 4.2.1, a measurement of the E plane corresponds to a roll of the test antenna. This rotation causes the antenna to point toward the absorber on the tabletop and then toward the ceiling. This difference could cause an asymmetry. To eliminate or reduce this effect, a wire-grid polarizer was used to change the polarization of the source so that the measurement could be made with an azimuthal rotation. Shown in Figure 4-14, the crosspolar level is low enough so that measurements with the polarizer can be assumed to be free from crosspolar contamination. Other explanations for the deviation are offered in Section 4.4.

E plane measurements with the polarizer shown in Figure 4-15 agreed with theory to a level of approximately 8 dB but still showed deviation. This measurement indicates that

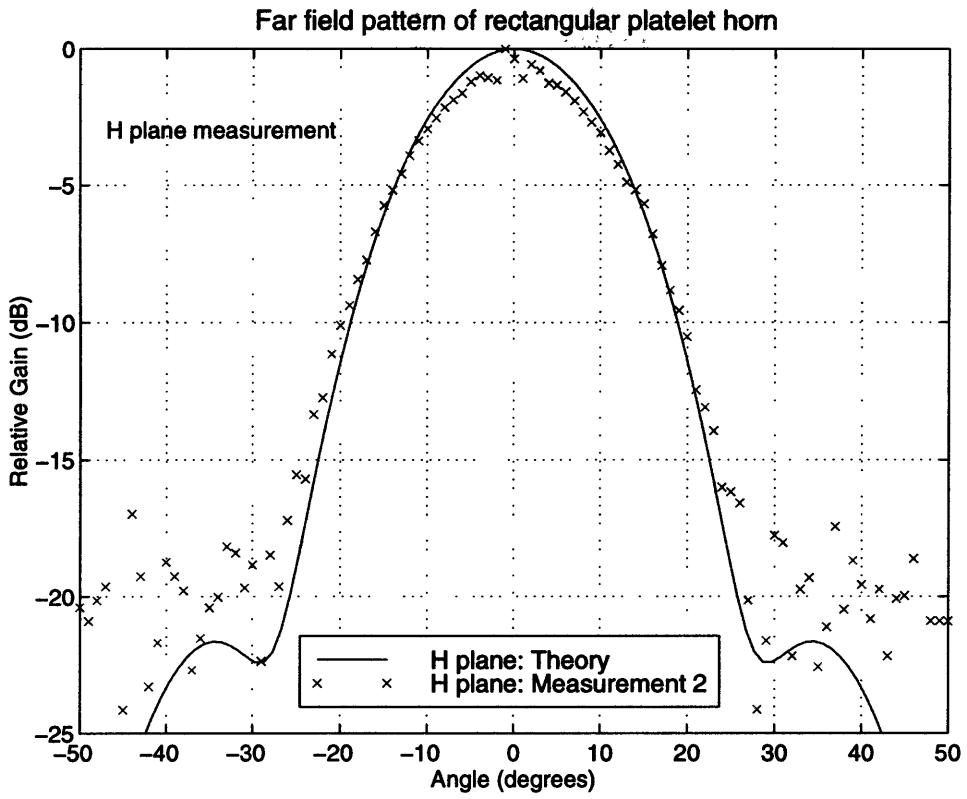

Figure 4-16: *H plane pattern of rectangular platelet horn. Compact range measurement. This horn had a half flare angle of* $7.17°$ *and initial side of* 1.35λ.

the deviation in the E plane measurement was not simply the fact that the test antenna was first pointed at the table and then at the ceiling.

These measurements of the far-field patterns of the quasi-integrated horn with rectangular machined section indicated that accurate measurement of far-field patterns is possible using either the far-field or compact antenna range. However, if asymmetries are noted, the measurement should be questioned and changes made to the measurement configuration to eliminate the asymmetry.

4.3.2 Rectangular Platelet Horn

As with the rectangular machined horn, the H plane measurements of the rectangular platelet horn agreed quite well with theory as shown in Figure 4-16. No E plane measurements were made, because it was assumed that more accurate measurements could be made after

a thicker gold layer was deposited through electroplating. The H plane measurements were taken before electroplating. Thus, much less signal could be detected than with the machined horn, and the dynamic range of the measurements was limited to approximately 17 dB. After gold plating, coverage was not uniform; therefore, no measurements were taken. The agreement with theory does further indicate that the antenna range is accurate and that platelet horns can be used as good approximations of smooth walled machined horns.

As mentioned in Section 4.1.1, the six platelet horns were electroplated, but only one horn (platelet horn design #3) had a continuous coating of gold. The rectangular platelet horn (platelet horn design #1) could not be retested, because it did not receive a continuous coating of gold.

4.3.3 Circular Platelet Horns

E plane measurements of a circular platelet horn shown in Figure 4-17 show a close correlation between theory and measurement. As with the measurement of the rectangular platelet horn, this measurement was performed before electroplating. As previously noted, the gold coating was very thin, and thus, the horn was very lossy. The dynamic range was limited to approximately 13 - 14 dB.

A measurement of the H plane pattern of the 3.25° circular horn shown in Figure 4-18 did not agree as well with theory as the E plane measurement did. Because the measured pattern is symmetric, it is likely that the deviation is not caused by measurement error. Possible causes of the deviation from theory are mentioned in Section 4.4. The originally postulated cause for this difference was the existence of excessive loss in the platelet horn due to a thin gold coating. Thus, at this point, the electroplating described in Section 4.1.1 was performed.

Unfortunately, the horn on which the previous tests were performed did not receive a continuous gold plating in the electroplating and could not be used for further measurements. The single horn that did receive a continuous gold coat was tested with results similar to the pre-electroplating measurements. The E plane measurements shown in Figure 4-19 agreed

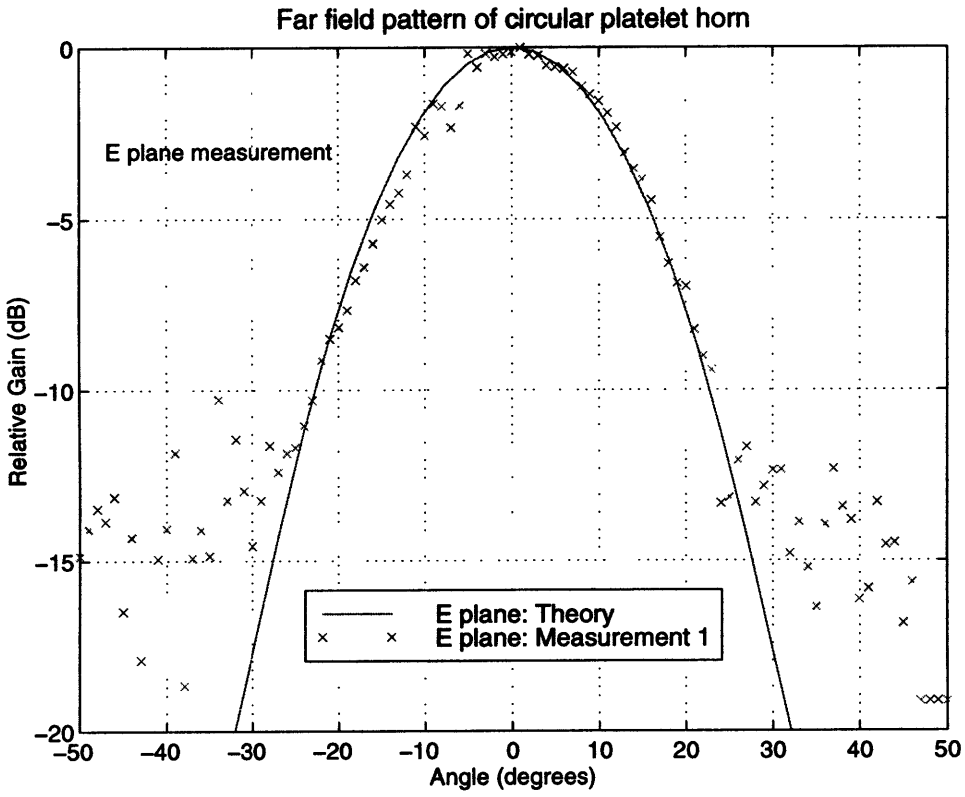

Figure 4-17: *E plane pattern of circular platelet horn. Compact range measurement. Pre-electroplating. This horn had a half flare angle of* 3.25° *and initial radius of* 0.95λ.

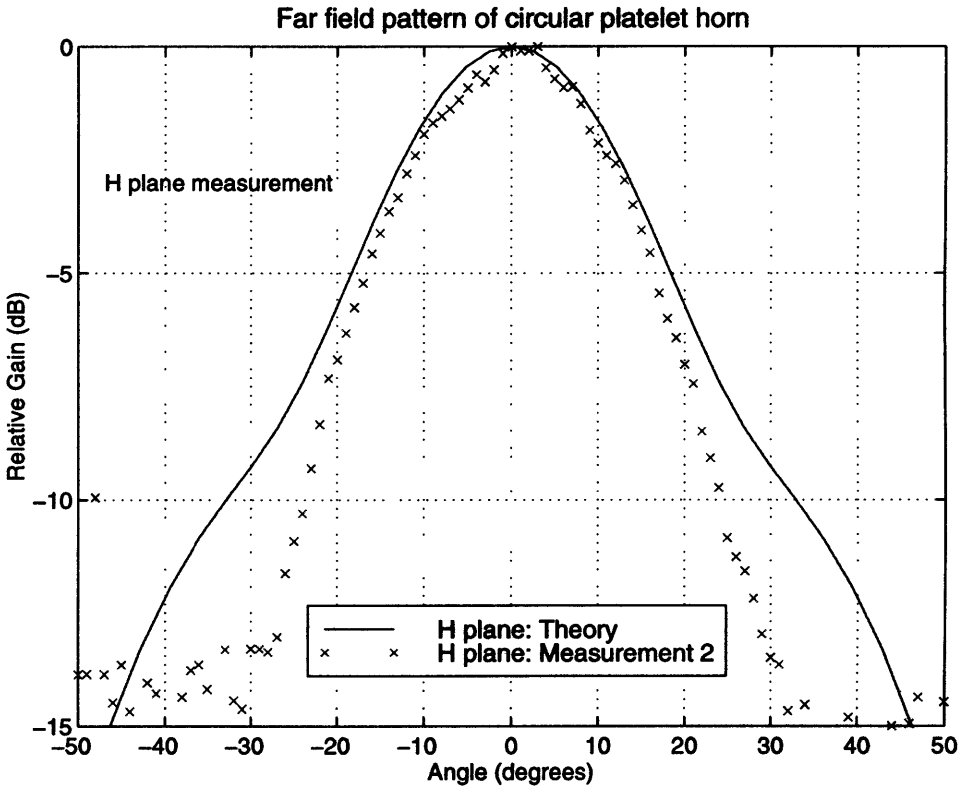

Figure 4-18: *H plane pattern of circular platelet horn. Compact range measurement. Pre-electroplating. This horn had a half flare angle of* 3.25° *and initial radius of* 0.95λ.

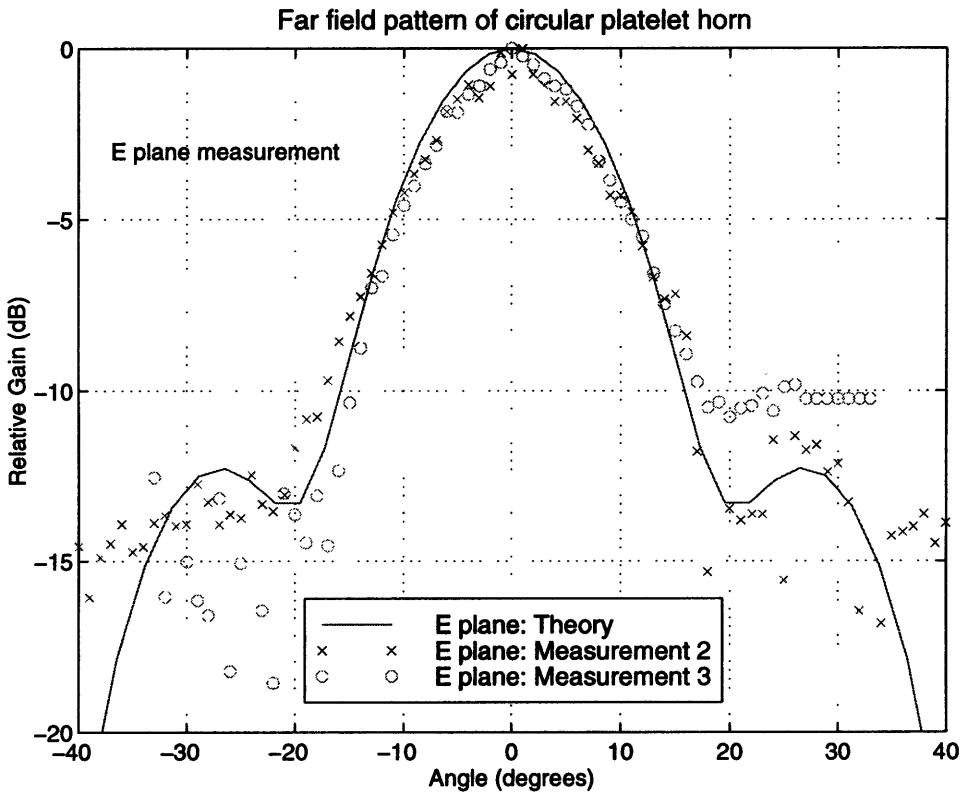

Figure 4-19: *E plane pattern of circular platelet horn. Compact range measurement. Post-electroplating. This horn had a half flare angle of* 5.67° *and initial radius of* 0.95λ.

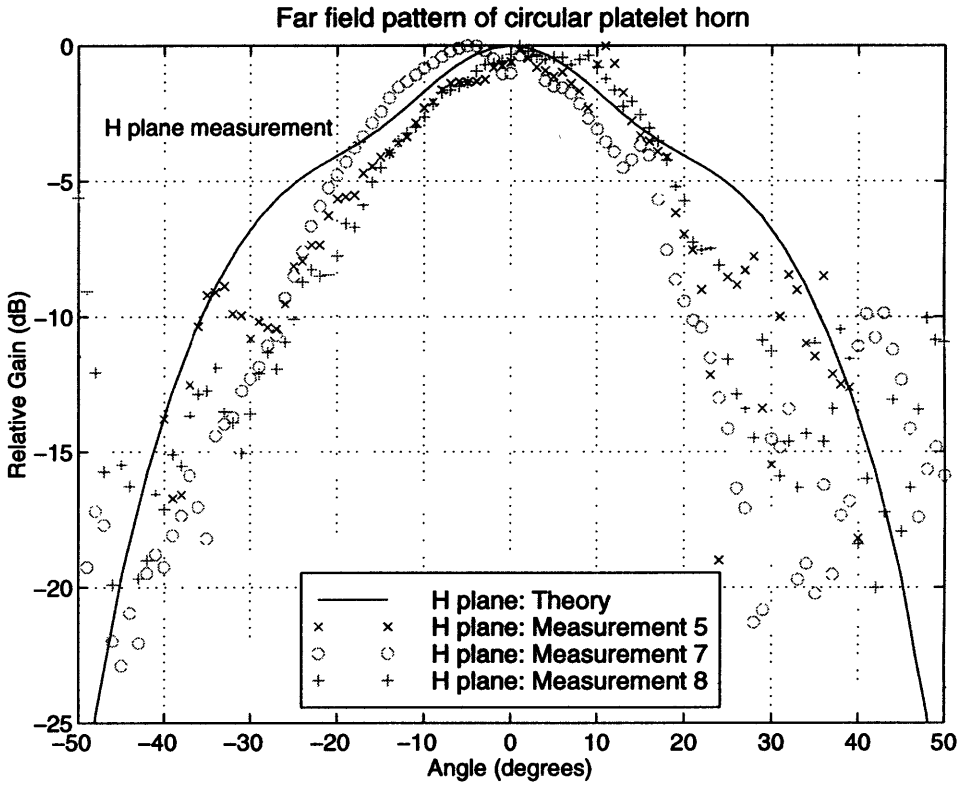

Figure 4-20: *H plane pattern of circular platelet horn. Compact range measurement. Post-electroplating. This horn had a half flare angle of* 5.67° *and initial radius of* 0.95λ.

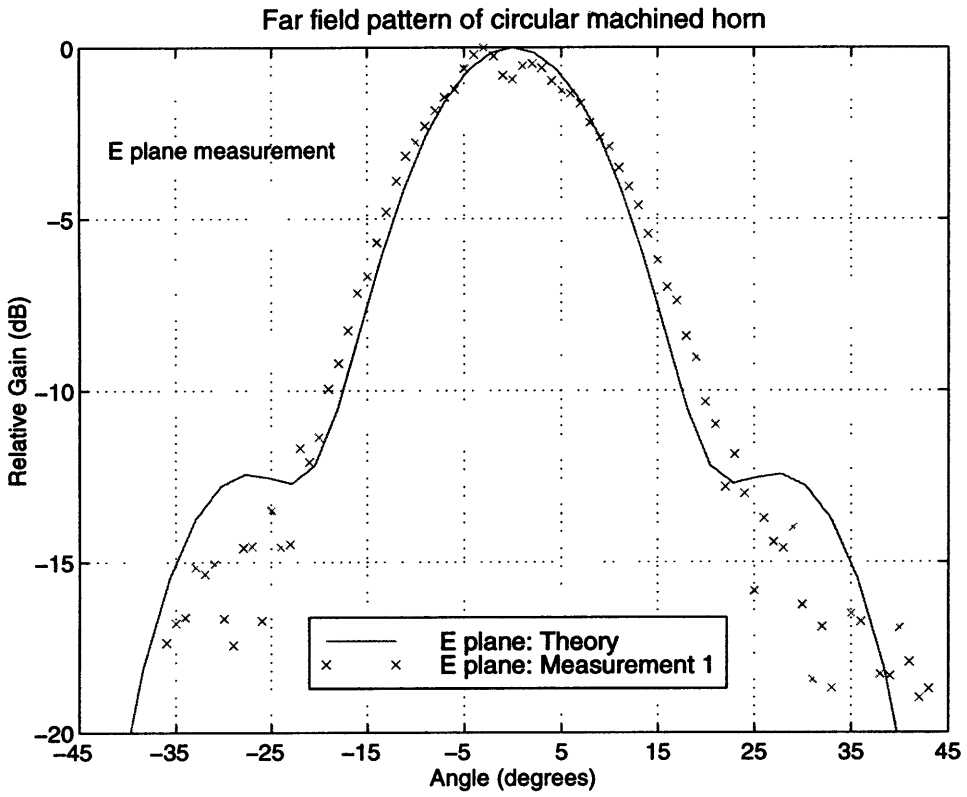

Figure 4-21: *E plane pattern of circular machined horn. Compact range measurement. This horn had a half flare angle of* 5.00° *and initial radius of* 0.95λ.

well with theoretical predictions. However, the H plane measurements shown in Figure 4-20 did not agree as well. The H plane measurements showed significant asymmetries that were probably due to measurement error as noted earlier. The beam pattern was narrower than the beam pattern of the theoretical predictions as in the pre-electroplating measurements. The device used to make these measurements ceased to function before the asymmetries in the beam pattern could be corrected or before further tests could be performed.

To investigate whether the problem of current discontinuity accounted for the deviation, horns were machined out of a solid piece of metal.

4.3.4 Conventional Machined Horns

Measurements of the quasi-integrated horn with circular machined sections displayed similar agreement and discrepancy with theory as did the measurements of the circular platelet

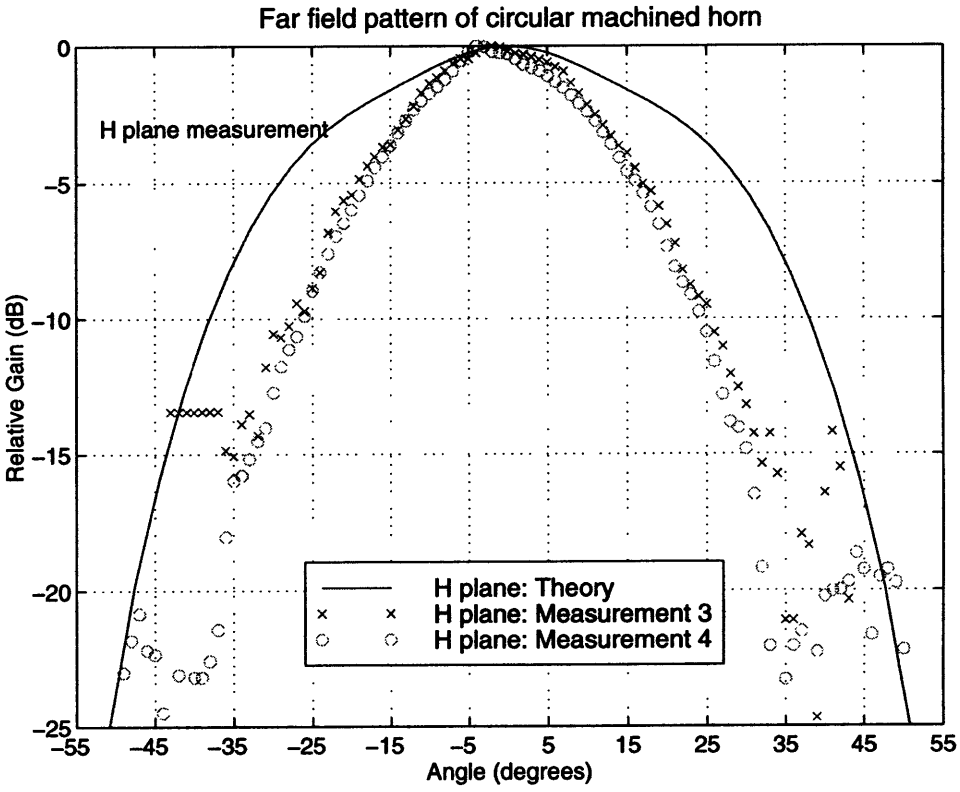

Figure 4-22: *H plane pattern of circular machined horn. Compact range measurement. This horn had a half flare angle of* 5.00° *and initial radius of* 0.95λ.

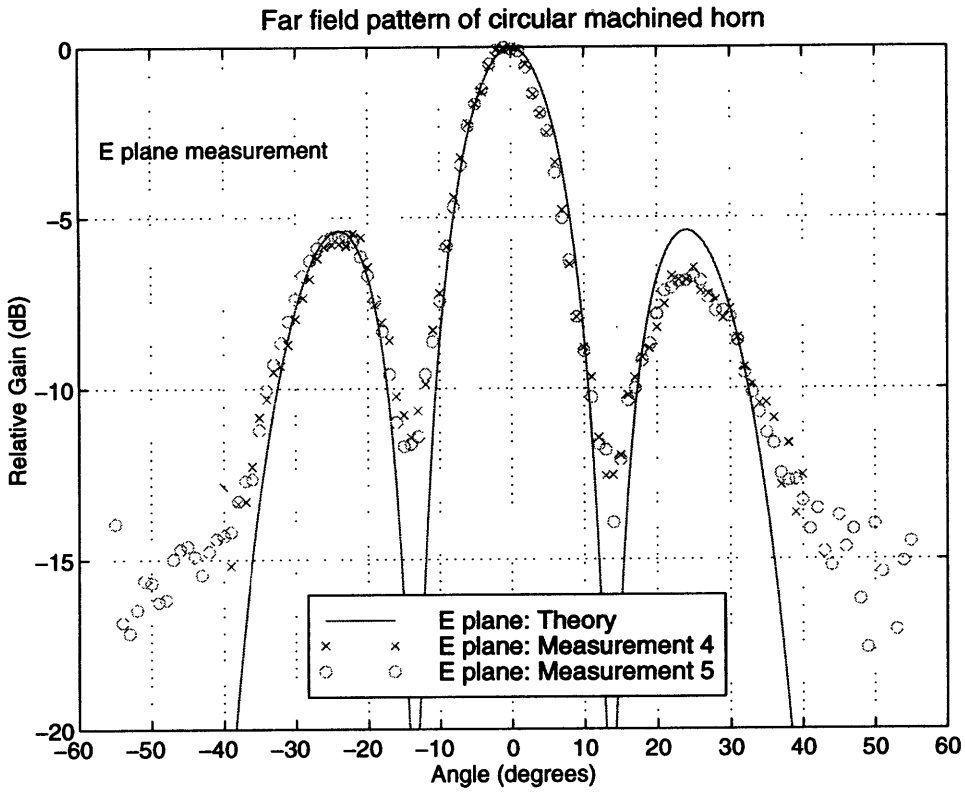

Figure 4-23: *E plane pattern of circular machined horn. Compact range measurement. This horn had a half flare angle of* 5.00° *and initial radius of* 1.22λ.

horns. Specifically, for the case of a circular horn with initial radius 0.95λ which circumscribes the aperture of the micromachined antenna, the E plane shown in Figure 4-21 agreed well with theory, while the H plane shown in Figure 4-22 did not agree well. The discrepancy between the theory and measurement in the H plane of this horn is the largest of any measured. Even though the measured beam is much narrower than the predicted, the general shape is the same.

Measurements of a conventionally machined circular horn section provided the most compelling evidence that the modeling code is functioning correctly. The E plane agrees extremely well with predictions, as shown in Figure 4-23. The notable characteristic of the E plane measurement is the presence of three narrow lobes. These lobes indicate that higher order modes are being excited and the mode matching program correctly predicts their relative amplitude and phase. The excitation of higher order modes is expected as the step between the micromachined guide and the circular machined section is large. Though

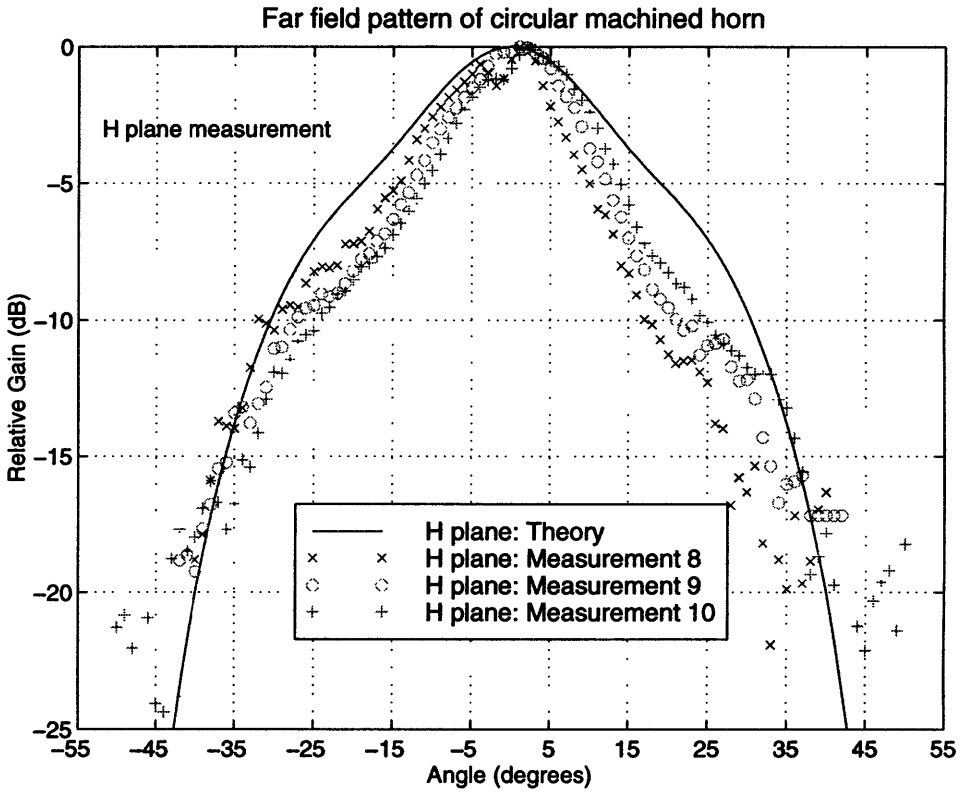

Figure 4-24: *H plane pattern of circular machined horn. Compact range measurement. This horn had a half flare angle of* 5.00° *and initial radius of* 1.22λ.

the sidelobes are slightly asymmetric, this difference is easily explainable by measurement error as mentioned previously and as discussed in Section 4.4. Because the step between the two sections was so large, centering the micromachined section to the circular section was more difficult. This misalignment could account for the asymmetry. Even though the H plane measurement did not agree exactly with theory as shown in Figure 4-24, the discrepancy was not large.

All of the microbolometers ceased to function before measurements could be taken of any other horns.

4.4 Differences Between Theory and Measurement

Modifications of the experimental setup could eliminate some sources of measurement error. For example, the axes of rotation of the test antenna did not pass through the center of the aperture. Thus, the test antenna samples a slightly different part of the incident field at every rotation angle. Because the incident field is not composed of perfect plane waves, this sampling difference will lead to errors. This problem can be corrected for azimuthal rotations by placing a xy translation stage on top of the rotation stage and moving the test antenna to the center of rotation of the rotation stage. To correct the problem in the roll of the test antenna, the mount needs to be redesigned. To ensure that the test antenna is in the center of the quiet zone, a xz translation stage should be placed underneath the rotation stage so that the entire apparatus can be moved vertically and horizontally through the quiet zone. Adding this translation stage would also allow for a more accurate sampling of the quiet zone. Another source of error is standing waves between different apparatuses in the experimental setup. To minimize their effects, a translation stage should be placed at the bottom of the stack of translation and rotation stages. By taking a measurement and then moving the test antenna $\frac{\lambda}{4}$ toward or away from the source, a series of measurements could be obtained which when averaged would minimize standing wave effects.

Increasing the dynamic range or equivalently decreasing the noise level of the measurements would be beneficial in obtaining measurements. The time required to take a single measurement would be substantially reduced. Extra dynamic range would allow

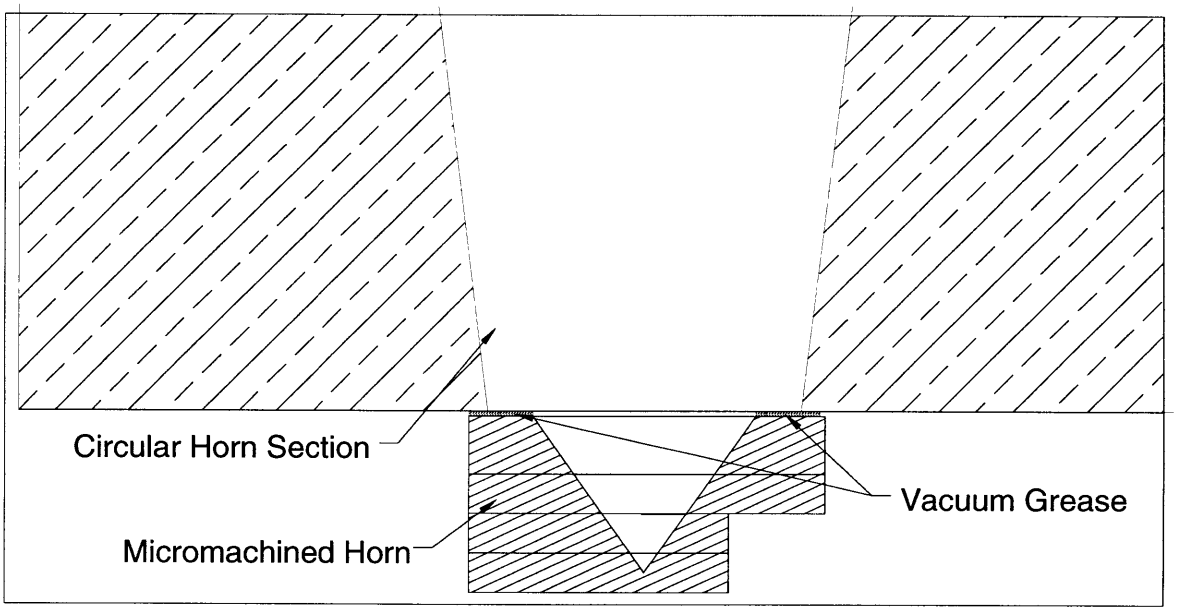

Figure 4-25: *Geometry of a gap created by vacuum between the micromachined and machined horn sections of the quasi-integrated horn antenna.*

the sidelobes to be measured giving a better evaluation of the accuracy of the simulation. The test antenna could be moved farther into the far field reducing effects of non-uniform illumination of the test antenna. By using a more powerful source, the dynamic range of the measurements could be increased. Using a detector bias that had less noise, such as a battery or a Keithley Programmable Current Source, could reduce the noise level. Finally, using more sensitive bolometers would provide increased dynamic range.

While calculations presented in Section 3.2 indicate that the far-field pattern does change with frequency, this mechanism is probably not responsible for the discrepancy between theory and measurement. The data sheets provided with the Gunn oscillator are assumed to accurately reflect the frequency of operation for different settings. Also, the patterns computed for different frequencies in Figures 3-5 and 3-6 do not match the data in Figures 4-19 and 4-20 better than the computed pattern for the design frequency. To obtain more data in the future, the far-field pattern could be measured for different frequencies.

Because the E plane far-field measurements of the quasi-integrated horn with rectangular machined section at both 95 and 190 GHz did not agree with the predictions of Eleftheriades's code, an explanation for those discrepancies could also explain discrepancies with a circular machined section. In measurements of the rectangular machined section, one pri-

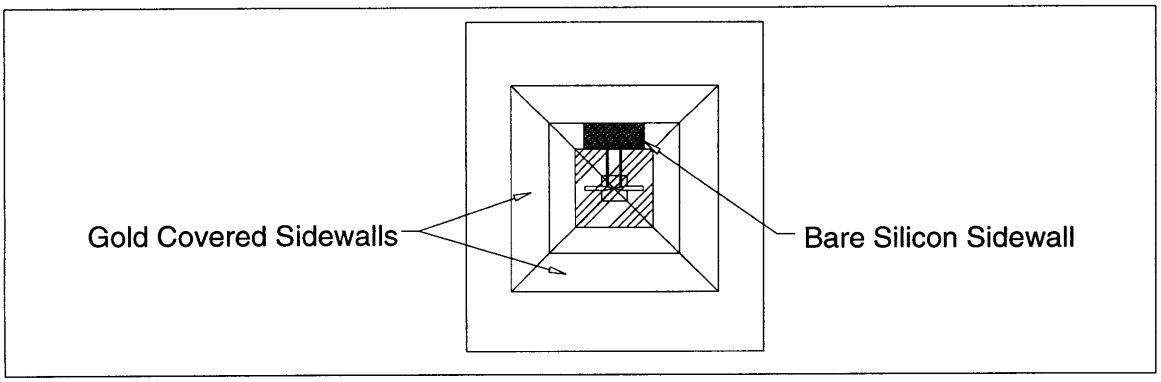

Figure 4-26: *Geometry of the section of micromachined horn not covered with gold during evaporation.*

mary plane exhibited very good agreement with data while the other did not. A similar effect was seen with circular machined sections. The fact that the discrepancy in measurement was seen at 95 GHz as well as at 190 GHz was significant since the 95 GHz measurements were performed by Arifur Rahman using a completely different experimental setup[42]. The micromachined and machined horns were different, as well. These facts indicate a systematic deviation which is not due to the measurement apparatus. The micromachined sections for quasi-integrated antennas at both frequencies were fabricated using the same procedure. Therefore, some effect caused by fabrication would affect the far-field patterns of both the 95 GHz and 190 GHz antennas.

A plausible mechanism involves a gap in the gold coating of the micromachined horn antenna sidewalls. When gold is evaporated on the sidewalls of the device wafer, a shadow mask is used to prevent gold from covering the membrane. The portion of the shadow mask blocking gold from the membrane must be supported from at least one side. Thus, a section of the sidewall is bare silicon as shown in Figure 4-26. As described in Section 5.2, a two-step evaporation could be used in which gold would be deposited with the shadow mask in the original orientation and then again with it rotated by 90° or 180°. With the existing gap in gold coverage, the boundary conditions are not the same as those assumed in the mode matching analysis. The eigenmodes of the sections modeling the device wafer will not be the same as those for a rectangular waveguide. This explanation was proposed because a mechanism was sought which could have an asymmetric effect[111] on the beam patterns, affecting one plane of radiation and not the other. Even though the E plane

is distorted in the rectangular case and the H plane is distorted in the circular case, the explanation is reasonable. The waveguide modes in each horn shape are different and could be affected differently. Analyzing this geometry in even a semi-quantitative manner would require extensive calculations. Measurements presented in [112, 113] indicate that bare Si sidewalls in the micromachined section result in a discrepancy between predictions of the mode matching code and measurement. Specifically, [112] indicates that the far-field pattern predictions are distorted in a manner similar to that which was observed in this thesis.

Another possible mechanism involves a gap between the micromachined horn and machined section. Since vacuum grease was used to affix the two sections together before bees wax could be used to attach them more securely, a small non-conducting gap exists between the two structures as illustrated in Figure 4-25. This problem is similar to the problem with gaps between wafers in the platelet horn. In the case of the platelet horn, the circular waveguide modes needing longitudinal current to support their propagation (TM modes) would have been attenuated[114]. For a gap between the machined and micromachined section, the situation would be slightly different. Current discontinuity would again be an issue. However, the geometry that needs to be considered is the radiation of the micromachined horn into a region of quasi-free space and then the coupling of the machined section to that region. This geometry is certainly not that which was modeled by the mode matching analysis described in Section 2.2.4.

We believe that these proposed deviations from assumptions in the model can explain the discrepancies between measurement and theory. To provide an external check for the mode matching portion of the code, a qualitative analysis of the implementation of the mode matching was performed in Appendix C. This analysis along with checks of the code against published data indicates that the mode matching is implemented correctly and deviations are due to fabrication or measurement issues.

Chapter 5

Conclusions

5.1 Conclusions

This thesis presents work performed on the modeling, design, and testing of quasi-integrated millimeter-wave horn antennas. Motivation for the development of these antennas was presented. The mode matching method was explained, and an electromagnetic model of a junction between a rectangular and circular guide has been formulated and implemented. This model has been applied to the design of quasi-integrated millimeter-wave horn antennas with circular machined sections. Smooth walled circular horn sections have been fabricated using conventional and laser machining. Far-field and compact antenna ranges were constructed and used to measure the far-field patterns of quasi-integrated horns. The data agrees well with predictions of the model. Reasonable explanations for the discrepancies between theory and experiment have been proposed.

5.2 Future Work

As described in Chapter 1, extensive interest exists in developing millimeter-wave frequency range systems for both commercial and military applications. Micromachining technology allows the development of millimeter-wave systems at much lower cost than traditional techniques. Thus, further development of millimeter-wave detection systems using the quasi-integrated horn technique should be pursued.

In order to obtain complete verification of mode matching code, the differences described in Section 4.4 should be resolved. Using a two-step evaporation process to cover the device wafer sidewalls with gold would eliminate the conductivity gap in the micromachined horn section. Developing a technique for adhering the machined and micromachined sections that did not use vacuum grease could remove or reduce the gap between the two sections. Acquiring translation stages to ensure that the test antenna is at the center of rotation of both axes of the two-axis rotation stage would eliminate measurement errors associated with rotating the antenna out of the center of the source field. Moving the entire measurement range inside a completely enclosed anechoic chamber would reduce reflections off of laboratory equipment. Another method for verifying the mode matching code experimentally would be to obtain rectangular and circular waveguide and measuring the scattering coefficients of the junction.

This work can be continued by pursuing different projects. Using relations derived in [65, 66, 115], the mode matching code can be modified to model the junction between a circular and a circular corrugated waveguide. A short smooth walled circular section could be used as a transition between the rectangular micromachined horn and the corrugated output horn. Alternatively, the relations for the transition between a rectangular guide and a rectangular or circular corrugated guide could be calculated. One of these configurations can provide superior performance to the smooth walled circular section[76].

Different fabrication techniques for the machined section can be attempted such as the use of metal platelet horns. The use of diffusion bonding to join the wafers into stacks would eliminate current discontinuities. Platelet horn technology has advantages over conventional machining in production of corrugated horns and non-circular apertures. Wet-etching has been used[76, 77] to define apertures in metal wafers. This techniques would eliminate the warping caused my laser machining metal wafers. At higher frequencies, two exciting new horn fabrication technologies have emerged. Laser milling has been used to create horns with corrugated and smooth walls[116]. Wet-etching of semiconductors has also been used to create square horns with flare angles other than 70.6°[117].

Different fabrication techniques for the microbolometer could result in detectors with higher performance. A research group in Finland has fabricated Nb microbolometers with

very high responsivity using a polyimide layer between the microbolometer and the silicon nitride membrane[118]. Alternative detector materials such as vanadium dioxide have also been used to fabricate microbolometers with very high responsivity as mentioned in [43].

This page intentionally left blank.

Appendix A

Derivation of Eigenmodes

The derivation presented in this appendix draws upon several sources. This composite method was chosen so that the expressions for the modes are particularly well suited for the mode matching technique. Following the technique found in Collin[83] and Kong[85], the expressions for the eigenmodes are derived using Maxwell's equations without the use of Hertzian or scalar potentials. A modification of Marcuvitz's[81] normalization constant is used. Conventions are a $e^{j\omega t}$ time dependence and a uniform, hollow waveguide with $\hat{z}$ as the longitudinal axis. With a longitudinal, z, dependence of $e^{\mp j\beta z}$, the substitutions

$$\nabla_z \times \vec{a} \rightarrow \mp j\beta\hat{z} \times \vec{a} \tag{A.1}$$

$$\nabla \cdot \vec{a}_z \rightarrow \mp j\beta a_z \tag{A.2}$$

can be used in addition to the standard

$$\frac{\partial}{\partial t} \rightarrow j\omega. \tag{A.3}$$

The longitudinal dependence term, $e^{\mp j\beta z}$, has been suppressed in most of the equations. If the sign of a term is indicated to vary with $\pm$ or $\mp$, the upper sign corresponds to the upper sign of $e^{\mp j\beta z}$ and the lower sign to the lower sign.

A.1 General Expressions

Expressions relating the electric and magnetic components of any electromagnetic field are derived from Maxwell's equations and the constitutive relations. Fields in a waveguide are generally described in terms of components transverse to the waveguide axis and components parallel to the axis. In order to facilitate this process, Maxwell's equations are broken down into equations relating the transverse field components and equations relating longitudinal components. The ∇ operator can be broken into a transverse, ∇_t and a longitudinal, $\nabla_z = \hat{z}\frac{\partial}{\partial z}$ component. Using these definitions, the curl of a vector can be broken down into transverse and longitudinal components

$$\nabla \times \vec{A} = (\nabla_t + \nabla_z) \times (\vec{a}_t + \vec{a}_z) = \underbrace{(\nabla_t \times \vec{a}_z + \nabla_z \times \vec{a}_t)}_{\text{transverse}} + \underbrace{\nabla_t \times \vec{a}_t}_{\text{longitudinal}} . \tag{A.4}$$

Maxwell's equations in free space (or a lossless guide with axial symmetry and filled with an isotropic dielectric) (2.11-2.14) then become

$$\nabla_t \times \vec{H}_z \mp j\beta\hat{z} \times \vec{H}_t = j\omega\epsilon\vec{E}_t \tag{A.5}$$

$$\nabla_t \times \vec{H}_t = j\omega\epsilon\vec{E}_z \tag{A.6}$$

$$\nabla_t \times \vec{E}_z \mp j\beta\hat{z} \times \vec{E}_t = -j\omega\mu\vec{H}_t \tag{A.7}$$

$$\nabla_t \times \vec{E}_t = -j\omega\mu\vec{H}_z \tag{A.8}$$

$$\nabla_t \cdot \vec{E}_t = \pm j\beta e_z \tag{A.9}$$

$$\nabla_t \cdot \vec{H}_t = \pm j\beta h_z. \tag{A.10}$$

Note that the constitutive relations for an isotropic dielectric (e.g. free space), equations (2.9) and (2.10), have been used. The homogeneous Helmholtz equations (2.15) and (2.16) can also be decomposed into transverse and longitudinal components

$$\nabla_t^2\vec{E}_t + k_c^2\vec{E}_t = 0 \tag{A.11}$$

$$\nabla_t^2 e_z + k_c^2 e_z = 0 \tag{A.12}$$

$$\nabla_t^2 \vec{H}_t + k_c^2 \vec{H}_t = 0 \tag{A.13}$$

$$\nabla_t^2 h_z + k_c^2 h_z = 0, \tag{A.14}$$

where $k_c^2 = k^2 - \beta^2 = \omega^2 \mu\epsilon - \beta^2$. These sets of equations describe the electromagnetic fields in a waveguide. Traditionally, the solutions of the field quantities take two forms, transverse electric (TE) solutions which do not have an axial component of the electric field and transverse magnetic (TM) solutions which do not have an axial component of the magnetic field.

A.1.1 TM modes

Modes which do not have a longitudinal component of the magnetic field are called TM modes or E modes. For these modes, equation (A.12) is solved for e_z, where $\vec{E}_z = \hat{z} e_z$, and this component is used to determine the other field components. This component plays the same role as the Hertzian potential in the Hertzian potential method for mode derivation. The vector identity, $\nabla_t \times \nabla_t \times \vec{a}_t = \nabla_t (\nabla_t \cdot \vec{a}_t) - \nabla_t^2 \vec{a}_t$, is used to rewrite the transverse curl of equation (A.8), i.e.

$$\nabla_t \times \nabla_t \times \vec{E}_t = \nabla_t \left(\nabla_t \cdot \vec{E}_t \right) - \nabla_t^2 \vec{E}_t = -j\omega\mu \vec{H}_z = 0. \tag{A.15}$$

Substitutions using equations (A.9) and (A.11) result in

$$\vec{E}_t = \frac{\mp j\beta}{k_c^2} \nabla_t e_z. \tag{A.16}$$

However, as it is preferable for the transverse electric field component to have a sign that does not vary with the direction of wave propagation e_z is redefined to be $\pm e_z$[1] so that

$$\vec{E}_t = \frac{-j\beta}{k_c^2} \nabla_t e_z. \tag{A.17}$$

[1]Because e_z is the solution to a *homogeneous* Helmholtz equation, it can be multiplied by any constant and still be a solution. This fact will be used again later for normalizing the modes.

Then, $\hat{z}\times$ equation (A.5) yields $\vec{H}_t = \pm Y_e \left(\hat{z} \times \vec{E}_t\right)$ where Y_e is the TM mode admittance, $\frac{\omega\epsilon}{\beta} = \frac{kY}{\beta}$. Y is the admittance of the medium, $Y = \sqrt{\frac{\epsilon}{\mu}} = \frac{1}{Z}$. However, so that the mode definition will be symmetric with the TE mode definition to be presented in the next section, $\vec{H}_t$ is redefined so that

$$\vec{H}_t = Y_e \left(\hat{z} \times \vec{E}_t\right). \tag{A.18}$$

This definition shifts the sign variation to the complete mode expression, i.e. $\vec{H} = \pm\vec{H}_t e^{\mp j\beta z}$ is used instead of $\vec{H} = \vec{H}_t e^{\mp j\beta z}$. The complete mode expressions are

$$\vec{E} = \vec{E}_t e^{\mp j\beta z} \pm \vec{E}_z e^{\mp j\beta z} = \frac{-j\beta}{k_c^2}\nabla_t e_z e^{\mp j\beta z} \pm \hat{z} e_z e^{\mp j\beta z} \tag{A.19}$$

$$\vec{H} = \pm\vec{H}_t e^{\mp j\beta z} = \pm Y_e \left(\hat{z} \times \vec{E}_t\right) e^{\mp j\beta z}. \tag{A.20}$$

A.1.2 TE modes

The derivation of the TE modes, or H modes, is the dual of the previous derivation and thus is not presented in detail. In this derivation, $\vec{H}_z$ plays the role of the potential function from which all the field components are obtained. The complete mode expressions are

$$\vec{H} = \pm\vec{H}_t e^{\mp j\beta z} + \vec{H}_z e^{\mp j\beta z} = \pm\left(\frac{-j\beta}{k_c^2}\nabla_t h_z\right) e^{\mp j\beta z} + \hat{z} h_z e^{\mp j\beta z} \tag{A.21}$$

$$\vec{E} = \vec{E}_t e^{\mp j\beta z} = -Z_h \left(\hat{z} \times \vec{H}_t\right) e^{\mp j\beta z} = -Z_h \left(\hat{z} \times \left(\frac{-j\beta}{k_c^2}\nabla_t h_z\right)\right) e^{\mp j\beta z}, \tag{A.22}$$

where Z_h is the TE mode impedance, $\frac{\omega\mu}{\beta} = \frac{kZ}{\beta}$.

A.1.3 Mode normalization and other considerations

While the functional form of the modes is determined by solving equations (A.5)-(A.14) and enforcing boundary conditions (2.5)-(2.8), the multiplicative constants can be chosen in many different ways. Olver et al. state, "The main numerical problem [in calculating the far-field patterns of multimode horns] is to ensure that the amplitude coefficients for all modes are normalized in a standard manner."[80]. For mode matching, it is preferable to

normalize the modes, such that

$$\int_A \vec{e}_m \cdot \vec{e}_m \, dA = 1, \tag{A.23}$$

where A is the transverse cross section of the waveguide. Another convention used in mode matching and other waveguide analyses is to express modes in the form

$$\vec{E}_t = \left(a^+ + a^-\right) \sqrt{Z_p} \vec{e}_t \tag{A.24}$$

$$\vec{H}_t = \left(a^+ - a^-\right) \frac{\vec{h}_t}{\sqrt{Z_p}} = \left(a^+ - a^-\right) \frac{\hat{z} \times \vec{e}_t}{\sqrt{Z_p}}, \tag{A.25}$$

where a^+ and a^- are the complex modal ampliude for the forward and reverse travelling waves, respectively. Z_p is the wave impedance of the mode, where $p =$ TE or TM. The mode functions $\vec{e}_t$ and $\vec{h}_t$ are chosen so that they have units $\frac{1}{m}$, which is required for the units in equation (A.23) to be correct. The factor of $\sqrt{Z_p}$ ensures that the modal amplitudes have units $\frac{V}{\sqrt{\Omega}}$, which means that $\frac{|a|^2}{2}$ is the power of a propagating mode and $\frac{\pm j|a|^2}{2}$ is the reactive power carried by an evanescent TE (upper sign) or TM (lower sign) mode[56]. The normalization constants for mode expressions in circular and rectangular guides were chosen taking into account these considerations.

A.2 Modes in a Circular Waveguide

In a circular guide, the cylindrical coordinate system, (ρ, ϕ, z), is the most convenient. In cylindrical coordinates, the ∇_t^2 operator is $\frac{1}{\rho}\frac{\partial}{\partial \rho}\left(\rho \frac{\partial}{\partial \rho}\right) + \frac{1}{\rho^2}\frac{\partial^2}{\partial \phi^2}$. The homogeneous Helmholtz equation becomes

$$\frac{1}{\rho}\frac{\partial}{\partial \rho}\left(\rho \frac{\partial a_z}{\partial \rho}\right) + \frac{1}{\rho^2}\frac{\partial^2 a_z}{\partial \phi^2} + k_c^2 a_z = 0. \tag{A.26}$$

Separable solutions for which $a_z(\rho, \phi) = a_{z\rho}(\rho)\, a_{z\phi}(\phi)$ are sought. For that class of solutions, equation (A.26) can be rewritten as

$$\left(\rho^2 \frac{\partial^2 a_{z\rho}}{\partial \rho^2} + \rho \frac{\partial a_{z\rho}}{\partial \rho}\right) \frac{1}{a_{z\rho}} + k_c^2 \rho^2 = -\frac{\partial^2 a_{z\phi}}{\partial \phi^2} \frac{1}{a_{z\phi}}. \tag{A.27}$$

As the left and right side of the equation are functions of different variables, both must be equal to a constant for the equation to be always satisfied. The two resulting equations are

$$(k_c\rho)^2 \frac{\partial^2 a_{z\rho}}{\partial (k_c\rho)^2} + (k_c\rho) \frac{\partial a_{z\rho}}{\partial (k_c\rho)} + \left((k_c\rho)^2 - q^2\right) a_{z\rho} = 0 \tag{A.28}$$

$$\frac{\partial^2 a_{z\phi}}{\partial \phi^2} = -q^2 a_{z\phi}, \tag{A.29}$$

where q^2 is the separation constant. The solutions traditionally chosen for equation (A.28) are Bessel functions of the first kind, i.e. $a_{z\rho} = J_q(k_c\rho)$. Any harmonic function, $\sin q\phi$, $\cos q\phi$, or $e^{\mp jq\phi}$, will solve equation (A.29), but the eigenmodes are generally chosen to be real functions. Thus, the two solutions are

$$a_z = J_q(k_\rho\rho) \left\{ \begin{array}{c} \sin q\phi \\ \cos q\phi \end{array} \right\}. \tag{A.30}$$

The modes are degenerate and are simply the same field distribution rotated by 90°. Because the azimuthal component, $a_{z\phi}$, must be periodic with period 2π, q is taken to be a positive integer. The allowed values of k_ρ $(= k_c)$ are determined by enforcing the boundary conditions. For reasons mentioned in section A.1.3, the function is multiplied by constants. Based on Marcuvitz[81] and my own work, the best choice of constants is $-j\frac{k_\rho^2}{\beta} N_{qr}^p$, where N_{qr}^p is the geometrical normalization constant, p = TE or TM, and q and r specify the mode.

A.2.1 TM modes

For TM modes, e_z is the function which takes the form of equation (A.30), which when multiplied by the appropriate constants becomes

$$e_z = -j\frac{k_\rho^2}{\beta} N_{qr}^{TM} J_q(k_\rho\rho) \left\{ \begin{array}{c} \sin q\phi \\ \cos q\phi \end{array} \right\}. \tag{A.31}$$

Application of equations (A.17) and (A.18) yields

$$\vec{E}_t^{TM} = \hat{\rho}\left(-N_{qr}^{TM}\right) k_\rho J_q'(k_\rho\rho) \left\{ \begin{array}{c} \sin q\phi \\ \cos q\phi \end{array} \right\} + \hat{\phi}\left(-N_{qr}^{TM}\right) \frac{q}{\rho} J_q(k_\rho\rho) \left\{ \begin{array}{c} \cos q\phi \\ -\sin q\phi \end{array} \right\} \tag{A.32}$$

$$\vec{H}_t^{TM} = Y_e \left(\hat{\rho} N_{qr}^{TM} \frac{q}{\rho} J_q(k_\rho\rho) \left\{ \begin{array}{c} \cos q\phi \\ -\sin q\phi \end{array} \right\} - \hat{\phi} N_{qr}^{TM} k_\rho J_q'(k_\rho\rho) \left\{ \begin{array}{c} \sin q\phi \\ \cos q\phi \end{array} \right\} \right). \tag{A.33}$$

According to Marcuvitz[81], the geometrical normalization constant for TM modes is

$$N_{qr}^{TM} = \sqrt{\frac{\epsilon_q}{\pi}} \frac{1}{k_\rho R J_{q+1}(k_\rho R)}, \tag{A.34}$$

where R is the waveguide radius and

$$\epsilon_q = \left\{ \begin{array}{ll} 1 & \text{if } m = 0 \\ 2 & \text{if } m \neq 0 \end{array} \right. . \tag{A.35}$$

Note that the constant N_{qr}^{TM} is incorrectly defined in [119]. Wu and MacPhie[72] chose

$$e_z = -j \frac{k_\rho^2}{\beta} N_{qr}^{TM} J_q(k_\rho\rho) \left\{ \begin{array}{c} -\sin q\phi \\ \cos q\phi \end{array} \right\}, \tag{A.36}$$

which means the mode functions used in their paper have non-standard signs

$$\vec{E}_t^{TM} = \hat{\rho}\left(-N_{qr}^{TM}\right) k_\rho J_q'(k_\rho\rho) \left\{ \begin{array}{c} -\sin q\phi \\ \cos q\phi \end{array} \right\} + \hat{\phi}\left(-N_{qr}^{TM}\right) \frac{q}{\rho} J_q(k_\rho\rho) \left\{ \begin{array}{c} -\cos q\phi \\ -\sin q\phi \end{array} \right\} \tag{A.37}$$

$$\vec{H}_t^{TM} = Y_e \left(\hat{\rho} N_{qr}^{TM} \frac{q}{\rho} J_q(k_\rho\rho) \left\{ \begin{array}{c} -\cos q\phi \\ -\sin q\phi \end{array} \right\} - \hat{\phi} N_{qr}^{TM} k_\rho J_q'(k_\rho\rho) \left\{ \begin{array}{c} -\sin q\phi \\ \cos q\phi \end{array} \right\} \right), \tag{A.38}$$

where $J_q'(k_\rho\rho)$ is the derivative of the q^{th} order Bessel function of the first kind. The allowed values of k_ρ can be found by applying the $\vec{E}$ field boundary condition, equation (2.5). The tangential component of the electric field, the $\hat{\phi}$ component, must be zero on the perfectly conducting boundary of the metal waveguide walls, i.e. $E_\phi = 0$ at $\rho = R$. Therefore, $k_\rho R$

must be a root of the Bessel function. If $h_{qr}R$ is the r^{th} root of the q^{th} order Bessel function, then the allowed values of k_ρ are $k_\rho = h_{qr}$. The mode expressions $\vec{e}_t$ and $\vec{h}_t$ mentioned in section A.1.3 are given by

$$\vec{e}_t^{TM} = \vec{E}_t^{TM} \tag{A.39}$$

and

$$\vec{h}_t^{TM} = \frac{1}{Y_e}\vec{H}_t^{TM}. \tag{A.40}$$

A.2.2 TE modes

For TE modes, h_z is the function which takes the form of equation (A.30), which when multiplied by the appropriate constants becomes

$$h_z = -j\frac{k_\rho^2}{\beta}N_{qr}^{TE}J_q(k_\rho\rho)\left\{\begin{array}{c}\sin q\phi\\ \cos q\phi\end{array}\right\}. \tag{A.41}$$

Application of equations (A.22)[2] and (A.21) yields

$$\vec{E}_t^{TE} = Z_h\left(\hat{\rho}\left(-N_{qr}^{TE}\right)\frac{q}{\rho}J_q(k_\rho\rho)\left\{\begin{array}{c}\cos q\phi\\ -\sin q\phi\end{array}\right\} + \hat{\phi}N_{qr}^{TE}k_\rho J_q'(k_\rho\rho)\left\{\begin{array}{c}\sin q\phi\\ \cos q\phi\end{array}\right\}\right) \tag{A.42}$$

$$\vec{H}_t^{TE} = \hat{\rho}\left(-N_{qr}^{TE}\right)k_\rho J_q'(k_\rho\rho)\left\{\begin{array}{c}\sin q\phi\\ \cos q\phi\end{array}\right\} - \hat{\phi}N_{qr}^{TE}\frac{q}{\rho}J_q(k_\rho\rho)\left\{\begin{array}{c}\cos q\phi\\ -\sin q\phi\end{array}\right\}. \tag{A.43}$$

According to Marcuvitz[81], the geometrical normalization constant for TE modes is

$$N_{qr}^{TE} = \sqrt{\frac{\epsilon_q}{\pi}}\frac{1}{J_q(k_\rho R)\sqrt{(k_\rho R)^2 - q^2}}. \tag{A.44}$$

Note that the constant N_{qr}^{TE} is incorrectly defined in [119]. As with the TM modes, the allowed values of k_ρ can be found by applying the $\vec{E}$ field boundary condition, equation (2.5). The component of the electric field tangential to the waveguide walls, the $\hat{\phi}$ component, must vanish on the perfectly conducting boundary, i.e. $E_\phi = 0$ at $\rho = R$, where R is the

[2]The negative sign in front of Z_h is distributed.

radius of the waveguide. Therefore, $k_\rho R$ must be a root of the derivative of the Bessel function. If $h'_{qr}R$ is the r^{th} root of derivative of the q^{th} order Bessel function, then the allowed values of k_ρ are $k_\rho = h'_{qr}$. The same result can be obtained by enforcing the condition, equation (2.7), that the component of the $\vec{H}$ field normal to waveguide vanish at the wall. The mode expressions $\vec{e}_t$ and $\vec{h}_t$ mentioned in section A.1.3 are given by

$$\vec{e}_t^{TE} = \frac{1}{Z_h}\vec{E}_t^{TE} \tag{A.45}$$

and

$$\vec{h}_t^{TE} = \vec{H}_t^{TE}. \tag{A.46}$$

A.3 Modes in a Rectangular Waveguide

The derivation of eigenmodes in a rectangular waveguide follows the same steps as the derivation for a circular guide. The different boundary conditions result in a different function form for the solutions, of course. Cartesian coordinates, $(x, y, z,)$, are the most convenient coordinate system choice. The ∇_t^2 operator is $\frac{\partial^2}{\partial x^2} + \frac{\partial^2}{\partial y^2}$, and the homogenous Helmholtz equation becomes

$$\frac{\partial^2 a_z}{\partial x^2} + \frac{\partial^2 a_z}{\partial y^2} + k_c^2 a_z = 0. \tag{A.47}$$

Separable solutions for which $a_z(x, y) = a_{zx}(x)\, a_{zy}(y)$ are sought. For that class of solutions, equation (A.47) can be rewritten as

$$\frac{1}{a_{zx}}\frac{\partial^2 a_{zx}}{\partial x^2} + \frac{1}{a_{zy}}\frac{\partial^2 a_{zy}}{\partial y^2} + k_c^2 = 0. \tag{A.48}$$

Both the a_{zx} term and the a_{zy} term must be equal to constants, because they are functions of different variables and the left side of the equation is a constant. The resulting equations are

$$\frac{1}{a_{zx}}\frac{\partial^2 a_{zx}}{\partial x^2} = -k_x^2 \tag{A.49}$$

$$\frac{1}{a_{zy}}\frac{\partial^2 a_{zy}}{\partial x^2} = -k_y^2, \tag{A.50}$$

where k_x and k_y are constants to be specified by the boundary conditions. As with the ϕ component in cylindrical coordinates, the solutions to equations (A.49) and (A.50) are any harmonic function but are chosen to be the real functions, sine and cosine. Unlike the circular case, the sine and cosine solutions are not degenerate, and the boundary conditions for the type of mode involved must be enforced to determine the correct form of the solution. The multiplicative constants which result in a convenient expression for the modes are $j\frac{k_c^2}{\beta}N_{mn}$ for TM modes and $-j\frac{k_c^2}{\beta}N_{mn}$ for TE modes, where $k_c^2 = k_x^2 + k_y^2$ and $N_{mn} = \frac{\sqrt{\epsilon_m \epsilon_n}}{\sqrt{ab(k_x^2+k_y^2)}}$. The factors ϵ_m and ϵ_n are defined in equation (A.35), and a and b are respectively the x and y dimensions of the waveguide.

A.3.1 TM modes

As the field component $\vec{E}_z = \hat{z}e_z$ is parallel to the waveguide walls, it must vanish on all of the perfectly conducting boundaries, $x = 0$, $x = a$, $y = 0$, and $y = b$, according to equation (2.5).[3] Thus, the functional form of e_z must be $\sin\frac{m\pi}{a}x \sin\frac{n\pi}{b}y$, where m and n are integers. Equations (A.17) and (A.18) result in

$$\vec{E}_t^{TM} = \hat{x}N_{mn}k_x \cos k_x x \sin k_y y + \hat{y}N_{mn}k_y \sin k_x x \cos k_y y \tag{A.51}$$

and

$$\vec{H}_t^{TM} = Y_e\left(-\hat{x}N_{mn}k_y \sin k_x x \cos k_y y + \hat{y}N_{mn}k_x \cos k_x x \sin k_y y\right), \tag{A.52}$$

where $k_x = \frac{m\pi}{a}$ and $k_y = \frac{n\pi}{b}$. The complete expressions for the field of one mode are of the same form as equations (A.17) and (A.18), while the normalized modes have the same form as equations (A.39) and (A.40).

[3]The origin of the Cartesian coordinate system is taken to be the lower left corner of the waveguide.

A.3.2 TE modes

In order to determine the correct functional form of h_z, equation (A.21) can be used to see that $\vec{H}_t \sim \hat{x}\frac{\partial h_z}{\partial x} + \hat{y}\frac{\partial h_z}{\partial y}$. According to equation (2.7), the normal component of the $\vec{H}$ field in an isotropic material must vanish on the perfectly conducting waveguide walls. Thus, the x component, $\frac{\partial h_z}{\partial x}$, must vanish at $x = 0$ and $x = a$, and the y component, $\frac{\partial h_z}{\partial y}$, must vanish at $y = 0$ and $y = b$. Therefore, the x component must have a $\sin \frac{m\pi}{a}x$ dependence, and the y component must have a $\sin \frac{n\pi}{b}y$ dependence. h_z must then be $-j\frac{k_c^2}{\beta}N_{mn} \cos \frac{m\pi}{a}x \cos \frac{n\pi}{b}y$. Application of equations (A.21) and (A.22) yields

$$\vec{H}_t^{TE} = \hat{x}N_{mn}k_x \sin k_x x \cos k_y y + \hat{y}N_{mn}k_y \cos k_x x \sin k_y y \tag{A.53}$$

and

$$\vec{E}_t^{TE} = Z_h \left(\hat{x}N_{mn}k_y \cos k_x x \sin k_y y - \hat{y}N_{mn}k_x \sin k_x x \cos k_y y\right), \tag{A.54}$$

where $k_x = \frac{m\pi}{a}$ and $k_y = \frac{n\pi}{b}$. The complete expressions for the field of one mode are of the same form as equations (A.22) and (A.21), while the normalized modes have the same form as equations (A.45) and (A.46).

This page intentionally left blank.

Appendix B

Mode Matching Analysis of Rectangular to Circular Waveguide Transition

Using the expressions for eigenmodes in a circular guide provided by Wu and MacPhie, the mode matching procedure is applied to the junction between a smaller rectangular and a larger circular waveguide. Throughout this appendix, the notation of Wu and MacPhie[72] will be used. As shown in Figure B-1 (b), the coordinate system for the circular guide is (ρ, ϕ) or (x, y) and has its origin at the center of the circular guide. The coordinate system for the rectangular guide is (x', y') and has its origin in the lower left hand corner of the rectangular guide. The equations presented in appendix section A.2 are written in terms of polar coordinates, (ρ, ϕ) and the corresponding unit vectors, $\hat{\rho}$ and $\hat{\phi}$. While the unit vectors can easily be converted to Cartesian unit vectors through the standard Jacobian rotation matrix,

$$\begin{bmatrix} \hat{\rho} \\ \hat{\phi} \end{bmatrix} = \begin{bmatrix} \cos\phi & \sin\phi \\ -\sin\phi & \cos\phi \end{bmatrix} \begin{bmatrix} \hat{x} \\ \hat{y} \end{bmatrix}, \tag{B.1}$$

the functional form of the mode expressions (A.32) and (A.42) are not amenable to a simple transformation. Using a well known Bessel-Fourier series expansion of a plane wave[120],

$$e^{-j\vec{k}_i \cdot \vec{r}} = \sum_{q=-\infty}^{\infty} J_q(k \sin\theta_i \rho)\, e^{jq\phi} (j)^{-q} e^{-jq\phi_i} e^{-jk\cos\theta_i z}. \tag{B.2}$$

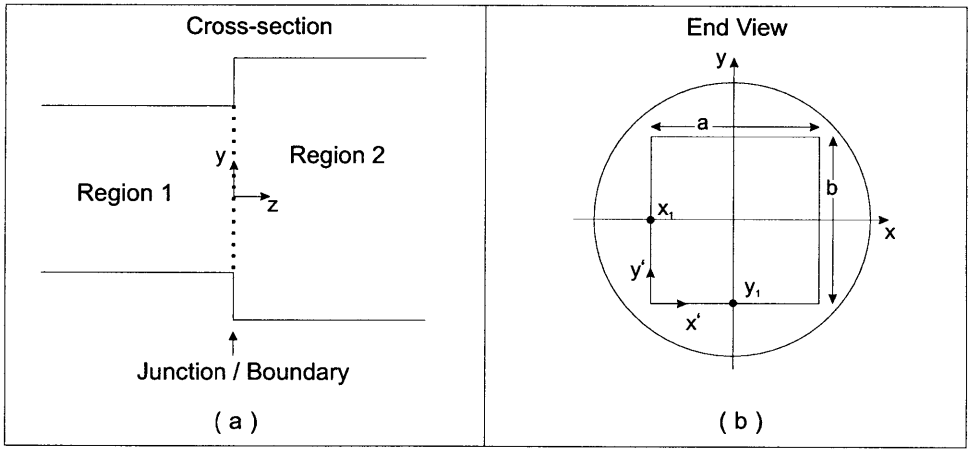

Figure B-1: *(a) Cross-section of a smaller rectangular waveguide to larger circular guide junction; (b) End view of rectangular to circular waveguide transition with coordinate systems labelled*

Wu and MacPhie derive the series expansion of $J_q(h\rho)\, e^{jq\phi}$

$$J_q(h\rho)\, e^{jq\phi} = \frac{(j)^q}{N} \sum_{l=0}^{N-1} e^{jl\frac{2q\pi}{N}} e^{-jh(C_l x + S_l y)}, \tag{B.3}$$

where $h = k \sin\theta_i$, $C_l = \cos\frac{l2\pi}{N}$, and $S_l = \sin\frac{l2\pi}{N}$. In order to obtain accurate results, the number N is selected such that $h\rho < \overline{N} - N_o$ where $N = 2\overline{N} + 1$ and N_o is a small integer. Using this series expansion and the coordinate transformations, the mode expressions (A.45) and (A.39) can be written as

$$\vec{e}^{TE} \begin{pmatrix} C \\ S \end{pmatrix}_{,qr} (x', y') = \frac{h'_{qr}}{N} (j)^{q+1} \sum_{l=0}^{N-1} \begin{pmatrix} C_{lq} \\ S_{lq} \end{pmatrix} e^{-jh'_{qr}(C_l x_1 + S_l y_1)} (\hat{x} S_l - \hat{y} C_l)\, e^{-jh'_{qr}(C_l x' + S_l y')} \tag{B.4}$$

and

$$\vec{e}^{TM} \begin{pmatrix} C \\ S \end{pmatrix}_{,qr} (x', y') = \frac{h_{qr}}{N} (j)^{q+1} \sum_{l=0}^{N-1} \begin{pmatrix} C_{lq} \\ -S_{lq} \end{pmatrix} e^{-jh_{qr}(C_l x_1 + S_l y_1)} (\hat{x} C_l + \hat{y} S_l)\, e^{-jh_{qr}(C_l x' + S_l y')}, \tag{B.5}$$

where $\begin{pmatrix} C \\ S \end{pmatrix}$ denotes the cosine and sine modes, respectively. The variables h'_{qr} and h_{qr} correspond to allowed values of k_ρ for the appropriate mode. The coordinate system has been shifted from (x, y) to (x', y') using the relations $x = x' + x_1$ and $y = y' + y_1$. Equations (B.4) and (B.5) correspond to the normalized form of equations (A.42) and (A.37), respectively. Using the expressions (B.4) and (B.5), the values of the various overlap integrals can be calculated.

As defined in section 2.2.4, the $\overline{\overline{H}}^C$ matrix has elements whose values are the overlap integrals of circular TE cosine-like modes and rectangular TE modes. For example, the overlap integral between the qr^{th} circular TE cosine-like mode and the mn^{th} rectangular TE mode is

$$H^C_{qr,mn} = \int_0^a \int_0^b \vec{e}^{\,TE}_{C,qr} \cdot \vec{e}^{\,TE}_{mn} dx'\, dy' \tag{B.6}$$

$$\begin{aligned} H^C_{qr,mn} = \; & N^{TE}_{qr} N_{mn} \frac{h'_{qr}}{N} (j)^{q+1} \sum_{l=0}^{N-1} C_{lq} e^{-jh'_{qr}(C_l x_1 + S_l y_1)} \\ & \int_0^a \int_0^b e^{-jh'_{qr}(C_l x' + S_l y')} (\hat{x} S_l - \hat{y} C_l) \\ & \cdot (\hat{x} k_y \cos k_x x' \sin k_y y' - \hat{y} k_x \sin k_x x' \cos k_y y')\, dx'\, dy' \end{aligned} \tag{B.7}$$

Examining the term formed by the inner product of the $\hat{x}$ terms, the integral portion of the equation can be separated to become

$$\underbrace{\int_0^a e^{-jh'_{qr} C_l x'} \cos k_x x' dx'}_{I1} \underbrace{\int_0^b e^{-jh'_{qr} S_l y'} \sin k_y y' dy'}_{I2}. \tag{B.8}$$

Integral $I1$ can be solved using standard techniques to obtain

$$I1 = jh'_{qr} C_l \frac{(-1)^m e^{-jh'_{qr} C_l a} - 1}{\left(h'_{qr} C_l\right)^2 - k_x^2} = jh'_{qr} C_l a \frac{(-1)^m e^{-jh'_{qr} C_l a} - 1}{\left(h'_{qr} C_l\right)^2 - (m\pi)^2} a, \tag{B.9}$$

where the relationship $k_x = \frac{m\pi}{a}$ has been used. Integral $I2$ can be similarly solved to obtain

$$I2 = k_y \frac{(-1)^n e^{-jh'_{qr} S_l b} - 1}{\left(h'_{qr} S_l\right)^2 - k_y^2} = n\pi \frac{(-1)^n e^{-jh'_{qr} S_l b} - 1}{\left(h'_{qr} S_l b\right)^2 o - (n\pi)^2} b, \tag{B.10}$$

where the relationship $k_y = \frac{n\pi}{b}$ has been used. By defining $I_m^C(\beta d)$ and $I_m^S(\beta d)$ as

$$I_m^C(\beta d) = \frac{1}{d}\int_0^d e^{-j\beta z}\cos\frac{m\pi}{d}z dz = j\beta d\frac{(-1)^m e^{-j\beta d}-1}{(\beta d)^2-(m\pi)^2} \tag{B.11}$$

and

$$I_m^S(\beta d) = \frac{1}{d}\int_0^d e^{-j\beta z}\sin\frac{m\pi}{d}z dz = m\pi\frac{(-1)^m e^{-j\beta d}-1}{(\beta d)^2-(m\pi)^2} = \frac{m\pi}{j\beta d}I_m^C(\beta d) \tag{B.12}$$

the product $I1\,I2$ can be written as

$$I1\,I2 = abI_m^C\left(C_l a'_{qr}\right) I_n^S\left(S_l b'_{qr}\right), \tag{B.13}$$

where the relations $a'_{qr} = h'_{qr}a$ and $b'_{qr} = h'_{qr}b$ have been used. The term formed by the scalar product of the $\hat{x}$ components of equation (B.7) can be written as

$$\frac{(j)^{q+1}}{N}\pi\sum_{l=0}^{N-1} C_{lq}e^{-jh'_{qr}(C_l x_1+S_l y_1)} S_l n a'_{qr} I_m^C\left(C_l a'_{qr}\right) I_n^S\left(S_l b'_{qr}\right). \tag{B.14}$$

The expression formed by the inner product of the $\hat{y}$ components in equation (B.7) can easily be shown to be

$$\frac{(j)^{q+1}}{N}\pi\sum_{l=0}^{N-1} C_{lq}e^{-jh'_{qr}(C_l x_1+S_l y_1)} C_l m b'_{qr} I_m^S\left(C_l a'_{qr}\right) I_n^C\left(S_l b'_{qr}\right). \tag{B.15}$$

Combining (B.14) and (B.15), the complete expression for $\overline{\overline{H}}^C_{qr,mn}$ can be written as

$$\begin{aligned}\overline{\overline{H}}^C_{qr,mn} = {} & N_{qr}^{TE}N_{mn}\frac{(j)^{q+1}}{N}\pi\sum_{l=0}^{N-1} C_{lq}e^{-jh'_{qr}(C_l x_1+S_l y_1)} \\ & \cdot\left(nS_l a'_{qr} I_m^C\left(C_l a'_{qr}\right) I_n^S\left(S_l b'_{qr}\right) + mC_l b'_{qr} I_m^S\left(C_l a'_{qr}\right) I_n^C\left(S_l b'_{qr}\right)\right)\end{aligned}. \tag{B.16}$$

By examining equation (B.4), the expression for $\overline{\overline{H}}^S_{qr,mn}$ is seen to be the same form as

(B.16) but with the substitution $C_{lq} \rightarrow S_{lq}$. Therefore, the complete expression is

$$\begin{Bmatrix} \overline{\overline{H}}^{C}_{qr,mn} \\ \overline{\overline{H}}^{S}_{qr,mn} \end{Bmatrix} = N_{qr}^{TE} N_{mn} \frac{(j)^{q+1}}{N} \pi \sum_{l=0}^{N-1} \begin{Bmatrix} C_{lq} \\ S_{lq} \end{Bmatrix} e^{-jh'_{qr}(C_l x_1 + S_l y_1)} \cdot \left(n S_l a'_{qr} I_m^C\left(C_l a'_{qr}\right) I_n^S\left(S_l b'_{qr}\right) + m C_l b'_{qr} I_m^S\left(C_l a'_{qr}\right) I_n^C\left(S_l b'_{qr}\right) \right) \tag{B.17}$$

Calculation of the $\overline{\overline{Q}}^{C}$, $\overline{\overline{Q}}^{S}$, $\overline{\overline{E}}^{C}$, and $\overline{\overline{E}}^{S}$ proceeds in the same manner as the calculation of $\overline{\overline{H}}^{C}$. The expressions for these overlap integrals are

$$\begin{Bmatrix} \overline{\overline{Q}}^{C}_{qr,mn} \\ \overline{\overline{Q}}^{S}_{qr,mn} \end{Bmatrix} = N_{qr}^{TM} N_{mn} \frac{(j)^{q+1}}{N} \pi \sum_{l=0}^{N-1} \begin{Bmatrix} C_{lq} \\ -S_{lq} \end{Bmatrix} e^{-jh_{qr}(C_l x_1 + S_l y_1)} \cdot \left(n C_l a_{qr} I_m^C(C_l a_{qr})\, I_n^S(S_l b_{qr}) - m S_l b_{qr} I_m^S(C_l a_{qr})\, I_n^C(S_l b_{qr}) \right) \tag{B.18}$$

and

$$\begin{Bmatrix} \overline{\overline{E}}^{C}_{qr,mn} \\ \overline{\overline{E}}^{S}_{qr,mn} \end{Bmatrix} = N_{qr}^{TM} N_{mn} \frac{(j)^{q+1}}{N} \pi \sum_{l=0}^{N-1} \begin{Bmatrix} C_{lq} \\ -S_{lq} \end{Bmatrix} e^{-jh_{qr}(C_l x_1 + S_l y_1)} \cdot \left(m C_l b_{qr} I_m^C(C_l a_{qr})\, I_n^S(S_l b_{qr}) + n S_l a_{qr} I_m^S(C_l a_{qr})\, I_n^C(S_l b_{qr}) \right) \tag{B.19}$$

As noted in literature[72, 119, 71], the elements of both $\overline{\overline{K}}$ matrices are identically zero. The equations in reference [72] corresponding to (B.6), (B.17), (B.18), and (B.19) all have errors. In [72], equations (8), (9), (11), (15), (16), and (18) have the incorrect normalization constants. Equation (18) has the incorrect sign in front of S_{lq}. Equation (19) has the second term in the sum as $S_l n a_{qr} I_m^C(C_l a_{qr})\, I_n^S(S_l b_{qr})$ instead of $S_l n a_{qr} I_m^S(C_l a_{qr})\, I_n^C(S_l b_{qr})$. Reference [72] cites the mode normalization expressions found in reference [119]. Both circular mode normalization expressions (located after equation (3)) are incorrect, and the rectangular mode normalization expression (equation (10)) is only accurate for modes which do not have $m = 0$.

In order to derive the generalized scattering matrices, the same method as presented in section 2.2.2 is used. As noted in section 2.2.4, however, to analyze a rectangular to circular waveguide junction with the rectangular guide as region 1, the definitions (2.60) and the equations (2.61)-(2.63) should be used. Equations (B.17), (B.18), and (B.19) provide the

values for all of the non-zero submatrices that comprise $\overline{\overline{M}}$. By substituting equation (2.62) into equation (2.63), the equation

$$\overline{\alpha}^- = \underbrace{\left(\overline{\overline{I}} + \overline{\overline{Z}}_\alpha^{\frac{1}{2}}\overline{\overline{M}}^T\overline{\overline{Z}}_\beta^{-1}\overline{\overline{M}}\,\overline{\overline{Z}}_\alpha^{\frac{1}{2}}\right)^{-1}\left(\overline{\overline{I}} - \overline{\overline{Z}}_\alpha^{\frac{1}{2}}\overline{\overline{M}}^T\overline{\overline{Z}}_\beta^{-1}\overline{\overline{M}}\,\overline{\overline{Z}}_\alpha^{\frac{1}{2}}\right)}_{\overline{\overline{S}}_{11}}\overline{\alpha}^+ + \underbrace{2\left(\overline{\overline{I}} + \overline{\overline{Z}}_\alpha^{\frac{1}{2}}\overline{\overline{M}}^T\overline{\overline{Z}}_\beta^{-1}\overline{\overline{M}}\,\overline{\overline{Z}}_\alpha^{\frac{1}{2}}\right)^{-1}\overline{\overline{Z}}_\alpha^{\frac{1}{2}}\overline{\overline{M}}^T\overline{\overline{Z}}_\beta^{-\frac{1}{2}}}_{\overline{\overline{S}}_{12}}\overline{\beta}^- \tag{B.20}$$

is obtained, and then further substitution yields

$$\overline{\beta}^+ = \underbrace{\overline{\overline{Z}}_\beta^{-\frac{1}{2}}\overline{\overline{M}}\,\overline{\overline{Z}}_\alpha^{\frac{1}{2}}\left(\overline{\overline{I}} + \overline{\overline{S}}_{11}\right)}_{\overline{\overline{S}}_{21}}\overline{\alpha}^+ + \underbrace{\left(\overline{\overline{Z}}_\beta^{-\frac{1}{2}}\overline{\overline{M}}\,\overline{\overline{Z}}_\alpha^{\frac{1}{2}}\overline{\overline{S}}_{12} - \overline{\overline{I}}\right)}_{\overline{\overline{S}}_{22}}\overline{\beta}^-. \tag{B.21}$$

These expressions for the generalized scattering matrices provide a full mode matching characterization of the junction between a smaller rectangular and larger circular guide.

Appendix C

Qualitative Verification of Mode Matching Code

The validity and correct application of the mode matching method can be verified at least in a qualitative sense by graphical inspection. As the name mode matching (or field matching) implies and as described in Section 2.2.1, the method derives from equating the electromagnetic fields on either side of a boundary. Thus, the generalized scattering matrix obtained for a junction can be tested by plotting the field on either side of the junction. By assuming an initial excitation on one side of the boundary, the submatrices S_{11} and S_{21} can be used to determine the total fields.

One of the example geometries described in [72] is the junction between a WR-75 waveguide and a centered circular waveguide with radius equal to the longer side of the rectangular guide. Figure C-1 shows the fields in either guide. In a color copy of the thesis, the fields in the circular guide are green, and in a black and white copy, they are gray. The fields in the rectangular guide are denoted by the black arrows. The fields fall almost exactly on top of one another in the boundary defined by the walls of the rectangular guide. On the metal surface tangential to the interface, the field in the circular guide is almost zero as the electric field vanishes on the face of a perfect electrical conductor. Wu and MacPhie[72] also provided a few of the elements of the generalized scattering matrix, which I used to check my code. However, I found that the values published in their paper were incorrect. They acknowledged that the values were incorrect and provided revised

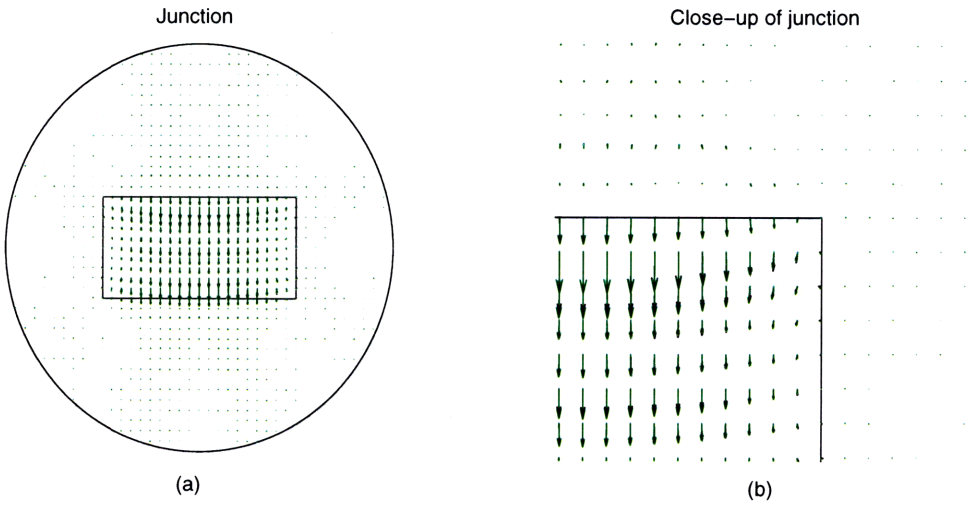

Figure C-1: *Electric field at junction between WR-75 waveguide (a = 2b = 0.75in.) and circular guide with R = a. TE10 excitation in rectangular guide. (a) Overview of entire junction. (b) Close-up of part of the junction.*

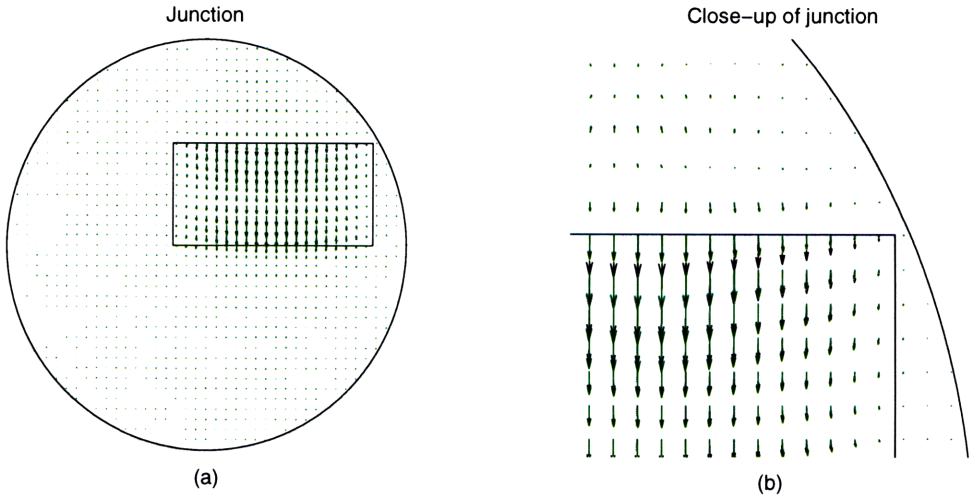

Figure C-2: *Electric field at junction between an offset WR-75 waveguide (a = 2b = 0.75in.) and circular guide with R = a. TE10 excitation in rectangular guide. (a) Overview of entire junction. (b) Close-up of part of the junction.*

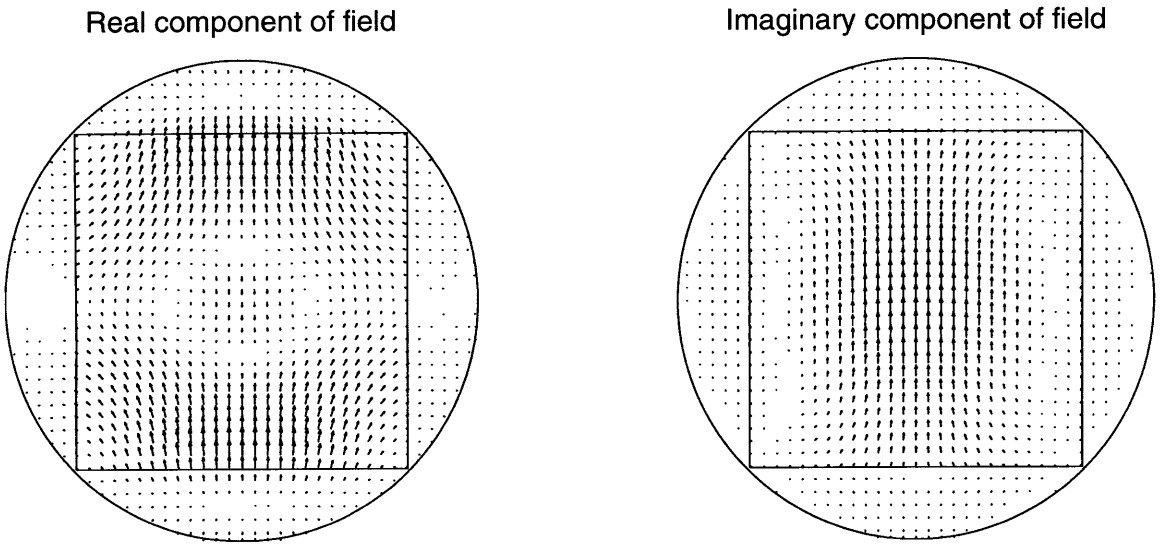

Figure C-3: *Electric field at junction between micromachined horn and circular section with radius* 0.97λ.

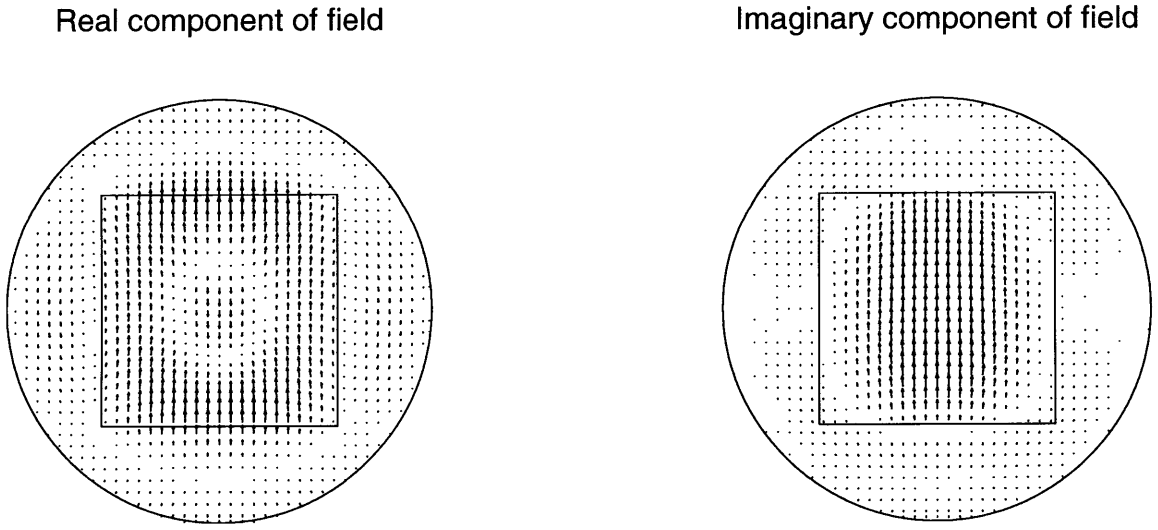

Figure C-4: *Electric field at junction between micromachined horn and circular section with radius* 1.22λ.

values which corresponded with mine. The case of an offset waveguide was also mentioned in [72]. This geometry is analyzed graphically in Figure C-2.

The same graphical method was used to analyze the micromachined horn to circular horn section transition. In this case, only the fields in the circular guide were analyzed, because the mode excitation coefficients in the rectangular guide were difficult to extract from Eleftheriades's code. Thus, the check being performed is simply that the electric field vanishes on the tangnetial metal wall. Real and imaginary components of the field exist simply because each mode has a complex weighting coefficient (associated with the magnitude and phase of the mode). As shown in Figure C-3, the fields are approximately zero on the surface of the metal. The geometry of a micromachined horn with larger circular section was also analyzed in Figure C-4. This qualitative analysis of the mode matching procedure used in the design of the circular horn sections indicates that deviations from predictions are due to experimental errors as described in Section 4.4.

Bibliography

[1] James C. Wiltse. *Millimeter and microwave engineering for communcations and radar*. SPIE, first edition, 1994.

[2] Darin Phelps. Vector analyzers evolve for millimeter-wave testing. *Microwaves and RF*, 36(6):152–160, 1997.

[3] T. H. Oxley and C. Burnett. mm-wave (30-110 GHz) hybrid microstrip technology. part I. *Microwave Journal*, 29(3):36–44, March 1986.

[4] T. H. Oxley and C. Burnett. mm-wave hybrid microstrip technology. part II. *Microwave Journal*, 29(5):177–185, May 1986.

[5] U. Guettich, A. Plattner, W. Schwab, I. Telliez, S. Tranchant, P. Savary, P. Bourne-Yaonaba, B. Byzery, E. Delhaye, C. Cordier, and M. Chelouche. 60 GHz GaAs MMIC technology for a high data rate mobile broadband demonstrator. In *1996 IEEE MTT-S International Microwave Symposium Digest*, number 2, pages 495–8, San Francisco, CA, USA, 1996. IEEE.

[6] Axel Stiller, Erwin M. Biebl, J.-F. Luy, Karl M. Strohm, and Josef Buechler. A monolithic integrated millimeter wave transmitter for automotive applications. *IEEE Trans. on Microwave Theory and Techniques*, 43(7):1654–8, July 1995.

[7] Lamberto Raffaelli and E. Stewart. Millimeter-wave monolithic components for automotive applications. *Microwave Journal*, 35(2):22–32, February 1992.

[8] Nicholas P. Morenc. MMICs for automotive radar applications. In *1996 IEEE MTT-S International Microwave Symposium Digest*, number 1, pages 39–41, San Francisco, CA, USA, 1996. IEEE.

[9] Holger H. Meinel. Commercial applications of millimeter waves, history, present status and future trends. *IEEE Trans. on Microwave Theory and Techniques*, 43(7):1639–53, 1995.

[10] Marc Liber and Francois Baron. 60 GHz communications, technology and applications trends. *Annales des Telecommunications*, 47(11-12):530–2, nov-dec 1992.

[11] Richard Leyshon. Millimeter technology gets a new lease on life. *Microwave Journal*, 35(3):26–35, March 1992.

[12] Teruhisa Ninomiya, Tamio Saito, Yoji Ohashi, and Hiroyuki Yatsuka. 60-GHz tranceiver for high-speed wireless lan system. In *1996 IEEE MTT-S International Microwave Symposium Digest*, number 2, pages 1171–4, San Francisco, CA, USA, 1996. IEEE.

[13] S. Meyer, J. Guena, J. C. Leost, E. Penard, and M. Goloubkoff. A new concept of LANs: Passive microwave links hooked onto a fiber optic backbone. In *1993 IEEE MTT-S International Microwave Symposium Digest*, number 3, pages 1549–52, Atlanta, GA, USA, 1993. IEEE.

[14] J. Wenger and J. Splettstoesser. Ka- and V- band MMIC components for personal communication networks. In *1996 IEEE MTT-S International Microwave Symposium Digest*, number 2, pages 491–4, San Francisco, CA, USA, 1996. IEEE.

[15] R. P. Braun, G. Grosskopf, C. H. von Helmholt, K. Krueger, U. Krueger, D. Rohde, and F. Schmidt. Optical microwave generation and transmission experiments in the 12 and 60 GHz-region for wireless communications. In *1996 IEEE MTT-S International Microwave Symposium Digest*, number 2, pages 499–501, San Francisco, CA, USA, 1996. IEEE.

[16] Holger H. Meinel. The market for short-haul line-of-sight millimeterwave transmission links. In *1996 IEEE MTT-S International Microwave Symposium Digest*, number 2, pages 487–9, San Francisco, CA, USA, 1996. IEEE.

[17] M. Hata, A. Fukazawa, M. Bessho, S. Makino, and M Higuchi. A new 40 GHz digital distribution radio with single local oscillator. In *1978 IEEE MTT-S International Microwave Symposium Digest*, pages 236–8, Ottawa, Ontario, Canada, 1978. IEEE.

[18] John Burns. The application of millimetre wave technology for personal communication networks in the united kingdom and europe: A technical and regulatory overview. In *1994 IEEE MTT-S International Microwave Symposium Digest*, number 2, pages 635–8, San Diego, CA, USA, 1994. IEEE.

[19] Michael J. Marcus. Spectrum management implications of millimeter wave technology. In *1994 IEEE MTT-S International Microwave Sypmosium Digest*, number 2, pages 631–4, San Diego, CA, USA, 1994. IEEE.

[20] Minoru Kotaki, Yukio Takimoto, Eisaku Akustu, Yasuhiro Fujita, Hiroshige Fukuhara, and Tsuneo Takahashi. Development of millimeter wave automotive sensing technology in japan. In *1992 IEEE MTT-S International Microwave Symposium Digest*, number 2, pages 709–12, Albuquerque, NM, USA, 1992. IEEE.

[21] L. Q. Bui, Y. Alon, and D. Neilson. Extended range coverage of an imaging radar system with feed-mounted 94 GHz MIMIC HEMT low noise amplifier and external LO. In *1992 IEEE MTT-S International Microwave Symposium Digest*, number 2, pages 687–90, Albuquerque, NM, USA, 1992. IEEE.

[22] Holger Meinel and A. Plattner. Millimetre-wave propagation along railway lines. *IEE Proceedings F (Communications, Radar and Signal Processing)*, 130(7):688–694, December 1983.

[23] Rahul Dixit. Microwave and millimeter-wave applications in automotive electronics. In *1996 IEEE MTT-S International Microwave Symposium Digest*, number 1, pages 31–3, San Francisco, CA, USA, 1996. IEEE.

[24] Holger H. Meinel. Applications of microwaves and millimeterwaves for vehicle communications and control in europe. In *1992 IEEE MTT-S International Microwave Symposium Digest*, number 2, pages 609–12, Albuquerque, NM, USA, 1992. IEEE.

[25] Lamberto Raffaelli. Millimeter-wave automotive radars and related technology. In *1996 IEEE MTT-S International Microwave Symposium Digest*, number 1, pages 35–8, San Francisco, CA, USA, 1996. IEEE.

[26] A. G. Stove. Automotive radar at 80 - 90 GHz. In *1992 IEEE MTT-S International Microwave Symposium Digest*, number 2, pages 613–16, Albuquerque, NM, USA, 1992. IEEE.

[27] N. Haese, M. Benlamlih, D. Cailleu, and P. A. Rolland. Low-cost design of a quasi-optical front-end for on board mm-wave pulsed radar. In *1992 MTT-S International Microwave Symposium Digest*, number 2, pages 621–3, Albuquerque, NM, USA, 1992. IEEE.

[28] Zong-Wen Li and Wolfgang Menzel. A 61GHz doppler radar using inverted strip dielectric waveguide. In *1992 IEEE MTT-S International Microwave Sympsium Digest*, number 2, pages 629–32, Albuquerque, NM, USA, 1992. IEEE.

[29] Juergen Detlefsen, Thomas Troll, Michael Rozmann, and Willi Zeilinger. System aspects and design of an automotive collision warning PN code radar using wavefront reconstruction. In *1992 IEEE MTT-S International Microwave Symposium Digest*, number 2, pages 625–8, Albuquerque, NM, USA, 1992. IEEE.

[30] T. Saito, N. Okubo, Y. Kawasaki, O. Isaji, and H. Suzuki. An FM-CW radar module with front-end switching heterodyne receiver. In *1992 IEEE MTT-S International Microwave Symposium Digest*, number 2, pages 713–6, Albuquerque, NM, USA, 1992. IEEE.

[31] D. A. Williams. Millimeter wave radars for automotive applications. In *1992 IEEE MTT-S International Microwave Symposium Digest*, number 2, pages 721–4, Albuquerque, NM, USA, 1992. IEEE.

[32] Kwo Wei Chang, Huei Wang, Greg Shreve, James G. Harrison, M. Core, A. Paxton, M. Yu, C. Harry Chen, and C. Samuel Dow. Forward-looking automotive radar using a W-band single-chip transceiver. *IEEE Trans. on Microwave Theory and Techniques*, 43(7):1659–68, July 1995.

[33] Linda P. B. Katehi. Novel transmission lines for the submillimeter-wave region. *Proceedings of the IEEE*, 80(11):1771–1787, 1992.

[34] James P. Hollinger. Applications of millimeter wave imaging. In *Proceedings of the SPIE*, number 544, pages 118–24, Arlington, VA, USA, 1985. SPIE.

[35] Larry Yujiri et al. Passive millimeter-wave camera. In *Proceedings of SPIE*, number 3064, pages 15–22, Orlando, FL, USA, 1997. SPIE.

[36] Gerhard de Lange, Brian R. Jacobson, and Qing Hu. A low-noise micromachined millimeter was heterodyne mixer with nb superconducting tunnel junctions. *Applied Physics Letters*, 68:1862, 1996.

[37] Gabriel M. Rebeiz, D. P. Kasilingham, P. A. Stimpson, and David B. Ruteledge. Monolithic millimeterwave two-dimensional horn imaging arrays. *IEEE Trans. on Antennas and Propagation*, 38:1473, 1990.

[38] George V. Eleftheriades and Gabriel M. Rebeiz. High-gain step-profiled integrated diagonal horn-antennas. *IEEE Trans. on Microwave Theory and Techniques*, 40:801–805, May 1992.

[39] George V. Eleftheriades, Walid Y. Ali Ahmad, Linda P. Katehi, and Gabriel M. Rebeiz. Millimeter-wave integrated-horn antennas part I: Theory. *IEEE Trans. on Antennas and Propagation*, 39:1575, 1991.

[40] Walid Y. Ali Ahmad, George V. Eleftheriades, Linda P. Katehi, and Gabriel M. Rebeiz. Millimeter-wave integrated-horn antennas part II: Experiment. *IEEE Trans. on Antennas and Propagation*, 39:1582, 1991.

[41] Walid Y. Ali Ahmad, Gabriel M. Rebeiz, William L. Bishop, and Thomas W. Crowe. An 86-106 GHz quasi-intergrated low noise schottky receiver. *IEEE Trans. on Microwave Theory and Techniques*, 41:588, 1993.

[42] Arifur Rahman, Erik Duerr, Gerhard de Lange, and Qing Hu. Micromachined room-temperature microbolometer for mm-wave detection and focal plane imaging arrays. In *Proceedings of SPIE*, SPIE Aerosense, Orlando, FL, April 1997. International Society of Optical Engineers (SPIE), SPIE.

[43] Arifur Rahman. Room temperature micromachined microbolometers for W-band (75 GHz – 110 GHz) focal plane imaging array. Master's thesis, Massachusetts Institute of Technology, Electrical Engineering Department, June 1996.

[44] Gerhard de Lange, Arifur Rahman, Erik Duerr, and Qing Hu. Development of a 3 x 3 micromachined millimeter wave sis imaging system. *IEEE Trans. on Applied Superconductivity*, 2(2):3593–3596, 1997.

[45] William R. McGrath, Christopher Walker, Markus Yap, and Yu-Chong Tai. Silicon micromachined waveguides for millimeter-wave and submillimeter-wave frequencies. *IEEE Microwave and Guided Wave Letters*, 3(3):61–63, 1993.

[46] A. A. Ayon, N. J. Kolias, and N. C. MacDonald. Tunable, micromachined parallel-plate transmission lines. In *IEEE/Cornell Conference on Advanced Concepts in High Speed Semiconductor Devices and Circuits*, pages 201–208, Ithaca, NY, August 1995. IEEE Electron Devices Society, IEEE.

[47] Terry T. H. Eng, Sidney C. Kan, and George K. L. Wong. Surface-micromachined epitaxial silicon contilevers as movable optical waveguides on silicon-on-insulator substrates. *Sensors and Actuators A (Physical)*, A49(1-2):109–113, 1995.

[48] Chen-Yu Chi and Gabriel M. Rebeiz. A low-loss 20 GHz micromachined bandpass filter. In *1995 IEEE MTT-S International Microwave Symposium Digest*, IEEE MTT-S International Microwave Symposium, pages 1531–1534, Orlando, FL, May 1995. IEEE, IEEE.

[49] S. S. Gearhart, C. C. Ling, and Gabriel M. Rebeiz. Monolithic millimeter-wave corner-reflector antennas. In *1990 International Symposium Digest. Antennas and Propagation.*, International Symposium on Antennas and Propagation. Merging Technologies for the 90's, pages 1914–1917, Dallas, TX, May 1990. IEEE, IEEE.

[50] Bassem Shenouda, L. W. Pearson, J. E. Harriss, W. Wang, and Y. Guo. Etched-silicon micromachined waveguides and horn antennas at 94 GHz. In *IEEE Antennas and Propagation Society International Symposium 1996 Digest*, number 2 in IEEE Antennas and Propagation Society International Symposium in conjunction with USNC/URSI National Radio Science Meeting, pages 988–991, Baltimore, MD, 1996. IEEE.

[51] B. Veidt, K. Kornelsen, J. F. Vneldik, D. Routledge, and M. J. Brett. Diagonal horn integrated with micromachined waveguide for submillimetre applications. *Electronics Letters*, 31(16):1307–1309, 1995.

[52] Gabriel M. Rebeiz and David B. Rutledge. Integrated horn antennas for millimeter-wave applications. *Annales des Telecommunications*, 47(1-2):38–48, 1992.

[53] George V. Eleftheriades, Walid Y. Ali-Ahmad, and Gabriel M. Rebeiz. A 20-db quasi-integrated horn antenna. *IEEE Microwave and Guided Wave Letters*, 2(2):73–75, 1992.

[54] Edouard Garcia, Brian R. Jacobson, and Qing Hu. Fabrication of high quality superconductor-insulator-superconductor junctions on thin si_3n_4 membranes. *Applied Physics Letters*, 63:1002, 1993.

[55] Gerhard de Lange, Konstantinos Konistis, and Qing Hu. Array of micromachined MMW SIS detectors with integrated JJLO: summary of first experimental results. in collaboration with HYPRES, October 1997.

[56] George V. Eleftheriades. *Analysis and Design of Integrated-Circuit Horn Antennas for Millimeter and Submillimeter-Wave Applications*. PhD dissertation, The University of Michigan, Department of Electrical Engineering, 1993.

[57] George V. Eleftheriades and Gabriel M. Rebeiz. Design and analysis of quasi-integrated horn antennas for millimeter and submillimeter-wave applications. *IEEE Trans. on Microwave Theory and Techniques*, 41(6/7):954–964, 1993.

[58] A. Wexler. Solution of waveguide discontinuities. *IEEE Trans. on Microwave Theory and Techniques*, 15(9):508–517, 1967.

[59] Y. C. Shih. The mode-matching method. In Tatsuo Itoh, editor, *Numerical Techniques for Microwave and Millimeter-Wave Passive Structures*, chapter 10, pages 622–631. Wiley Interscience, New York, first edition, 1989.

[60] R. Mittra and S. W. Lee. *Analytical Techniques in the Theory of Guided Waves*. Macmillan Series in Electrical Science. The Macmillan Company, 1971.

[61] S. M. Tun. Application of generalised circular and rectangular mode matching techniques to the design of antennas. In *IEE Colloquium on Application and Validation of Design Tools for Antennas*, pages 1/1–6, London, UK, 1993. IEE.

[62] A. Melloni, M. Politi, and G. Guido Gentili. Mode-matching analysis of TE011-mode waveguide bandpass filters. *IEEE Trans. on Microwave Theory and Techniques*, MTT-43(9):2109–16, September 1995.

[63] Hartmut Patzelt and Fritz Arndt. Double-plane steps in rectangular waveguides and their application for transformers, irises, and filters. *IEEE Trans. on Microwave Theory and Techniques*, MTT-30(5):771–6, May 1982.

[64] William J. English. The circular waveguide step-discontinuity mode transducer. *IEEE Trans. on Microwave Theory and Techniques*, MTT-21(10):633–6, October 1973.

[65] Graeme L. James and Bruce M. Thomas. TE11 to HE11 cylindrical waveguide mode converters using ring-loaded slots. *IEEE Trans. on Microwave Theory and Techniques*, MTT-30(3):278–85, March 1982.

[66] Graeme L. James. Analysis and design of TE11-to-HE11 corrugated cylindrical waveguide mode converters. *IEEE Trans. on Microwave Theory and Techniques*, MTT-29(10):1059–66, October 1981.

[67] T. S. Bird. Mode matching analysis of arrays of stepped rectangular horns and application to satellite antenna design. In *Seventh International Conference on Antennas and Propagation - ICAP 91*, number 2, pages 849–852, York, UK, 1991. IEE.

[68] A. D. Olver. Modal matching analysis in horn antenna analysis. In *International Conference on Computation in Electromagnetics*, pages 234–7, London, UK, 1991. IEE.

[69] Luiz C. da Silva and M. G. Castello Branco. Analysis fo the junction between smooth and corrugated cylindrical waveguides in mode converters. *IEEE Trans. on Microwave Theory and Techniques*, MTT-38(6):800–2, June 1990.

[70] J. M. Reiter and F. Arndt. Full-wave analysis of circular waveguide horn antennas including the outer wall geometry with an hybrid MM/BCMM method. In *IEEE Antennas and Propagation Society International Symposium. 1996 Digest*, number 3, pages 1984–7, Baltimore, MD, USA, 1996. IEEE.

[71] Reza Safavi-Naini and Robert H. MacPhie. Scattering at rectangular-to-rectangular waveguide junctions. *IEEE Trans. on Microwave Theory and Techniques*, MTT-30(11):2060–3, November 1982.

[72] Robert H. MacPhie and Ke-Li Wu. Scattering at the junction of a rectangular waveguide and a larger circular waveguide. *IEEE Trans. on Microwave Theory and Techniques*, 43(9):2041–2045, 1995.

[73] B. N. Das and P. V. D. Somasekhar Rao. Analysis of a transition between rectangular and circular waveguides. *IEEE Trans. on Microwave Theory and Techniques*, MTT-39(2):357–9, February 1991.

[74] Uwe Papziner and Fritz Arndt. Field theoretical computer-aided design of rectangular and circular iris coupled rectangular or circular waveguide cavity filters. *IEEE Trans. on Microwave Theory and Techniques*, 41(3):462–470, 1993.

[75] C. Sabatier. Scattering at an offset circular hole in a rectangular waveguide. *IEEE Trans. on Microwave Theory and Techniques*, MTT-40(3):587–92, March 1992.

[76] Robert W. Haas, Dennis Brest, Harry Mueggenburg, Lee Lang, and Dave Meimlich. Fabrication and performance of mmw and smmw platelet horn arrays. *International Journal of Infrared and Millimeter Waves*, 14(11):2289–2294, 1993.

[77] Robert W. Haas. Further development of MMW and SMMW platelet feed horn arrays. Number 75 in Astronomical Society of the Pacific Conference Series, pages 99–105, Tuscon, AZ, May 1994. Astronomical Society of the Pacific.

[78] Tatsuo Itoh. *Numerical Techniques for Microwave and Millimeter-wave Passive Structures*. John Wiley & Sons, Inc., first edition, 1989.

[79] Graeme L. James. On the problem of applying mode-matching techniques in analyzing conical waveguide discontinuities. *IEEE Trans. on Microwave Theory and Techniques*, MTT-31(9):718–23, September 1983.

[80] A. D. Olver, P. J. B. Clarricoats, A. A. Kishk, and L. Shafai. *Microwave Horns and Feeds*. First edition, 1994.

[81] N. Marcuvitz. *Waveguide Handbook*, volume 21 of *IEE Electromagnetic Wave Series*. Peter Peregrinus Ltd., first edition, 1986.

[82] Robert E. Collin. *Field Theory of Guided Waves*. IEEE Press, second edition, 1991.

[83] Robert E. Collin. *Foundation for Microwave Engineering*. McGraw Hill Physical and Quantum Electronics Series. McGraw Hill, first edition, 1966.

[84] David M. Pozar. *Microwave Engineering*. Addison-Wesley, first edition, 1990.

[85] Jin Au Kong. *Electromagnetic Wave Theory*. John Wiley & Sons, Inc., second edition, 1990.

[86] J. L. Fontecha and C. Cagigal. Transition rectangular to circular waveguide by means of rectangular guides. In *International Conference on Computation in Electromagnetics*, pages 378–381, London, UK, 1991. IEE.

[87] Jose R. Montejo-Garai and Juan Zapata. Full-wave design and realization of multicoupled dual-mode circular waveguide filters. *IEEE Trans. on Microwave Theory and Techniques*, MTT-43(6):1290–7, June 1995.

[88] Tatsuo Itoh. Generalized scattering matrix technique. In Tatsuo Itoh, editor, *Numerical Techniques for Microwave and Millimeter-Wave Passive Structures*, chapter 10, pages 622–631. Wiley Interscience, New York, 1 edition, 1989.

[89] P. D. Potter. A new horn antenna with suppressed sidelobes and equal beamwidths. *The Microwave Journal*, pages 71–8, June 1963.

[90] George V. Eleftheriades and Gabriel M. Rebeiz. A systematic approach towards the design of multimode quasi-integrated horn antennas for receiver applications. In *IEEE Antennas and Propagation Society International Symposium. 1992 Digest.*, number 1, pages 285–8, Chicago, IL, USA, 1992. IEEE.

[91] A. C. Ludwig. The definition of cross polarization. *IEEE Trans. on Microwave Antennas and Propagation*, AP-21(1):116–9, January 1973.

[92] Hiroyuki Deguchi, Mikio Takabayashi, Norio Miyahara, Shigeru Makino, Osami Ishida, and Takashi Katagi. An analysis of multimode conical horn antennas with flare-angle changes by using generalized telegraphist's equation. *Electronics and Communications in Japan, Part I.*, 80(2):79–89, February 1997.

[93] Daniele Bresciani, Giuseppe Figlia, Vito G. Daniele, and Daniela Finotto. Exact scattering matrix for the design of a multimode circular feed. In *1988 AP-S International Symposium Digest*, number 1, pages 79–89, Syracuse, NY, USA, June 1988. IEEE.

[94] Zhisheng Lin, Zhengmi Du, and Shener Chen. A 4mm-wave composite mode multimode conical feedhorn. *International Journal of Infrared and Millimeter Waves*, 17(10):1749–60, October 1996.

[95] Thua Van Ho and John Litva. Adaptive beamforming using multimode feed horn antennas. In *1989 AP-S International Symposium Digest*, number 3, pages 1654–7, San Jose CA, USA, June 1989. IEEE.

[96] D. LaFlame, P. Balling, J. Wu, N. Schroeder, and H. Wolf. Multi-mode antenna optimization. In *IEEE Antennas and Propagation Society International Symposium. 1992 Digest.*, number 3, pages 1344–7, Chicago, IL, USA, July 1992. IEEE.

[97] E. V. Jull. *Aperture Antennas and Diffraction Theory*, volume 10 of *IEE Electromagnetic Wave Series*. Peter Peregrinus Ltd., first edition, 1981.

[98] Constantine A. Balanis. *Antenna Theory*. John Wiley & Sons, Inc., first edition, 1982.

[99] S. Karmalkar, D. Sridhar, and J. Banerjee. A novel activation process for autocatalytic electroless deposition on silicon substrates. *Journal of the Electrochemical Society*, 144(5):1696–8, May 1997.

[100] Stanley Wolf and Richard N. Tauber. *Silicon Processing for the VLSI Era*. Lattice Press, first edition, 1986.

[101] J. L. Olsen. *Electron Transport in Metals*, volume 12 of *Interscience Tracts on Physics and Astronomy*. John Wiley & Sons, Inc., first edition, 1962.

[102] Technic, Inc. 1 Spectacle Street. Cranston, RI 02910.

[103] Wolfgang H. Kummer and Edmond S. Gillespie. Antenna measurements - 1978. *Proceedings of the IEEE*, 66(4):483–507, April 1978.

[104] J. S. Hollis, T. J. Lyon, and L. Clayton. *Microwave antenna measurements*. Scientific-Atlanta, Inc., first edition, 1970.

[105] A. E. Bailey. *Microwave Measurements*. Peter Peregrinus Ltd., second edition, 1989.

[106] A. D. Olver and A. A. Saleeb. Lens-type compact antenna range. *Electronics Letters*, 15(14):409–10, July 1979.

[107] Wolfgang Menzel and B. Huder. Compact range for millimetre-wave frequenciew using a dielectric lens. *Electronics Letters*, 20(19):768–9, September 1984.

[108] M. Philippakis and C. G. Parini. Compact antenna range performance evaluation using simulated pattern measurements. *IEE Proc. - Microwaves, Antennas, and Propagation*, 143(3):200–6, June 1996.

[109] DynaOptic Motion. 23561 Ridge Route. Suite U. Laguna Hills. CA 92653. Contact: Steve Berger.

[110] P. J. B. Clarricoats and A. D. Olver. *Corrugated Horns for Microwave Antennas*, volume 18 of *IEE Electromagnetic Wave Series*. Peter Peregrinus Ltd., first edition, 1984.

[111] Rolf Duerr. Private communication.

[112] Gabriel M. Rebeiz, Dayalan P. Kasilingam, Yong Guo, Philip A. Stimson, and David B. Rutledge. Monolithic millimeter-wave two-dimensional horn imaging arrays. *IEEE Trans. on Antennas and Propagation*, 38(9):1473–82, September 1990.

[113] Yong Guo, Karen Lee, Philip Stimson, Kent Potter, and David Rutledge. Aperture efficiency of integrated-circuit horn antennas. *Microwave and optical technology letters*, 4(1):6–9, January 1991.

[114] David H. Staelin, Ann W. Morgenthaler, and Jin Au Kong. *Electromagnetic Waves*. Prentice Hall, first edition, 1994.

[115] Graeme L. James. TE11-to-HE11 converters for small angle corrugated horns. *IEEE Trans. on Antennas and Propagation*, AP-30(6):1057–62, November 1982.

[116] C. K. Walker, T. M. Bloomstein, S. T. Palmacci, M. B. Stern, and J. E. Curtin. Laser micromachining of silicon: a new technique for fabricating high quality terahertz waveguide components. In *Eighth International Symposium on Space Terahertz Technology Proceedings.*, number 1, Cambridge, MA, USA, 1997.

[117] T. Crowe, P. J. Koh, W. L. Bishop, C. M. Mann, J. L. Hesler, R. M. Weikle II, P. A. D. Wood, and D. Matheson. Inexpensive receiver components for millimeter and submillimeter wavelengths. In *Eighth International Symposium on Space Terahertz Technology Proceedings.*, number 1, Cambridge, MA, USA, 1997.

[118] Arttu Luukanen. Private communication.

[119] John D. Wade and Robert H. MacPhie. Scattering at circular-to-rectangular waveguide junctions. *IEEE Trans. on Microwave Theory and Techniques*, 34(11):1085–1091, 1986.

[120] Samuel Silver. *Microwave Antenna Theory and Design*, volume 19 of *IEE Electromagnetic Wave Series*. Peter Peregrinus Ltd., first edition, 1984.